Analysis of Aircraft Accuracy Location in Aeronautical Multilateration Systems

Tiago Manuel Ribeiro Costa

Thesis to obtain the Master of Science Degree in

Electrical and Computer Engineering

Supervisor: Prof. Luís Manuel de Jesus Sousa Correia

Examination Committee

Chairperson: Prof. José Eduardo Charters Ribeiro da Cunha Sanguino

Supervisor: Prof. Luís Manuel de Jesus Sousa Correia

Members of Committee: Prof. António Manuel Restani Graça Alves Moreira

Eng. André Gustavo Botelho Maia

June 2017

To my beloved family

"I do not think that the wireless waves I have discovered
will have any practical application."

Heinrich Rudolf Hertz

"Truth is much too complicated to allow anything but approximations."

John von Neumann

Acknowledgements

Abstract

Aeronautical multilateration systems enable the locating of an aircraft based on the Time Difference of Arrival of its signal to three or more strategically placed receiving ground stations, located around an area of interest, providing continuous air traffic surveillance. The aim of this dissertation was to develop a model for the performance analysis of multilateration systems, concerning radio coverage and aircraft location accuracy. The proposed model considers ground stations' location, their antennas radiation patterns, transmitted power, receiver sensitivity, and the corresponding parameters for the aircraft. Line of Sight conditions are assessed by considering Digital Elevation, Fresnel's Ellipsoid, and the Effective Earth's Radius Models. The Free-Space Path Loss Model is also used, with fading margins being set to model power oscillations due to multipath and the aircraft orientation uncertainty. Aircraft accuracy location is estimated from the system's Geometric Dilution of Precision, considering error components due to tropospheric delay, multipath, receiver noise, quantisation, and clock bias. The model was implemented in a simulator and successfully validated, with results in agreement with data from the literature and previously implemented systems. The developed model was employed in the analysis of an implemented system from NAV Portugal, with results suggesting that the system has a good degree of redundancy, displaying negligible reductions in coverage, of as low as 2%, when two out of twelve ground stations are removed. A statistical analysis suggests that a Shifted Exponential Distribution can model the positioning error, with parameters proportional to the aircraft's altitude.

Keywords

Air Traffic Control; Distributed Positioning Systems; Aeronautical Multilateration; Positioning Error.

Resumo

Os sistemas de multilateração aeronáutica permitem localizar uma aeronave com base na diferença do tempo de chegada de sinais a três ou mais estações terrestres, localizadas ao redor de uma área de interesse. O objetivo desta dissertação foi desenvolver um modelo para a análise do desempenho de sistemas de multilateração relativamente à precisão da localização de aeronaves. O modelo proposto considera a localização das estações terrestres e da aeronave, os diagramas de radiação das antenas, a potência transmitida, e a sensibilidade do recetor. As condições de Linha-de-Vista são avaliadas, considerando os Modelos de Elevação Digital, do Elipsoide de Fresnel, e do Raio Efetivo da Terra. O Modelo de Propagação em Espaço Livre é também empregue, considerando margens de desvanecimento para as oscilações de potência devido a multipercurso e à incerteza da orientação da aeronave. A precisão da localização da aeronave é estimada a partir da Diluição Geométrica de Precisão, considerando as componentes de erro devido ao atraso troposférico, multipercurso, ruído do recetor, quantização, e enviesamento do relógio. O modelo foi implementado num simulador e validado com sucesso, com resultados em concordância com dados da literatura e de sistemas previamente implementados. Um sistema da NAV Portugal foi analisado, com resultados que sugerem que o sistema possui uma boa redundância, apresentando até 2% de redução da cobertura, quando duas de doze estações terrestres são removidas. A análise estatística sugere que o erro de posicionamento pode ser modelado por uma Distribuição Exponencial Deslocada, com parâmetros proporcionais à altitude da aeronave.

Palavras-chave

Controlo de Tráfego Aéreo; Sistemas de Posicionamento Distribuídos; Multilateração Aeronáutica; Erro de Posicionamento.

Table of Contents

List of Figures

List of Tables

List of Acronyms

ADC	Analogue-to-Digital Converter
ADS-B	Automatic Dependent Surveillance – Broadcast
ADS-C	Automatic Dependent Surveillance – Contract
AGL	Above Ground Level
AMSL	Above Mean Sea Level
ANSP	Air Navigation Service Provider
ARTAS	ATM Surveillance Tracker and Server
A-SMGCS	Advanced Surface Movement Guidance and Control Systems
ASTER GDEM V2	Advanced Spaceborne Thermal Emission and Reflection Radiometer Global Digital Elevation Model Version 002
ATC	Air Traffic Control
ATM	Air Traffic Management
AWGN	Additive White Gaussian Noise
BER	Bit Error Rate
CAD	Computer-Aided Design
CNR	Carrier-to-Noise Ratio
CNS	Communications, Navigation and Surveillance
CRLB	Cramér-Rao Lower Bound
DEM	Digital Elevation Model
DEMETER	Distance Measuring Equipment Tracer
DGPS	Differential Global Positioning System
DL	Downlink
DME	Distance Measuring Equipment
DPSK	Differential Phase Shift Keying
ECEF	Earth-Centred Earth-Fixed
ED	Document from the European Organisation for Civil Aviation Equipment
EGM96	1996 Earth Gravitational Model
EIRP	Effective Isotropic Radiated Power
EKF	Extended Kalman Filter
ENU	East-North-Up
ErM	Error Model
ES	Extended Squitter
EUROCAE	European Organisation for Civil Aviation Equipment
FEC	Forward Error Correction
GDEx	Global Data Explorer
GDoP	Geometric Dilution of Precision
GDP	Gross Domestic Product

GeoTIFF	Geographic Tagged Image File Format
GNSS	Global Navigation Satellite System
GPS	Global Positioning System
GS	Ground Station
GTD	Geometrical Theory of Diffraction
GVA	Gross Value Added
HAE	Height Above Ellipsoid
IF	Intermediate Frequency
ILS	Instrument Landing System
IMMKF	Interacting Multiple Model Kalman Filter
ITU	International Telecommunications Union
ITU-R	International Telecommunications Union – Radio sector
JPEG	Joint Photographic Experts Group
LAM	Local Area Multilateration
LoS	Line-of-Sight
LP DAAC	Land Processes Distributed Active Archive Centre
MDL	Minimum Discernible Signal
METI	Ministry of Economy, Trade, and Industry
MLAT	Aeronautical Multilateration
MLS	Microwave Landing System
MSL	Mean Sea Level
MTL	Minimum Triggering Level
NAA	Non-uniform Angular Array
NAV Portugal, EPE	Navegação Aérea de Portugal
NAVAID	Navigational Aid
NDB	Non-Directional Beacon
NED	North-East-Down
NLoS	Non Line-of-Sight
PBN	Performance Based Navigation
PCD	Probability of Code Detection
PD	Probability of Position Detection
PEC	Perfectly Electrically Conducting
PFCD	Probability of False Code Detection
PFD	Probability of False Detection
PO-SBR	Physical Optics - Shooting and Bouncing Ray
PPM	Pulse Position Modulation
PrM	Propagation Model
PSR	Primary Surveillance Radar
QoS	Quality of Service
RMS	Root Mean Square Value
RMSE	Root Mean Square Error
RSS	Root Sum of Squares
Rx	Receiver
SAT	Site Acceptance Test

SMR	Surface Movement Radar
SNR	Signal-to-Noise Ratio
SSR	Secondary Surveillance Radar
TDoA	Time Difference of Arrival
TMA	Terminal Manoeuvring Area
ToA	Time of Arrival
TSoA	Time Sum of Arrivals
Tx	Transmitter
UAA	Uniform Angular Array
UKF	Unscented Kalman Filter
UL	Uplink
ULA	Uniform Linear Array
VHF	Very High Frequency
VOR	VHF Omnidirectional Radio Range
WAM	Wide Area Multilateration
WGS84	1984 World Geodetic System

List of Symbols

$\gamma^k_{\Delta d_{pos}}$	sample kurtosis coefficient of the positioning error
$\gamma^s_{\Delta d_{pos}}$	sample skewness coefficient of the positioning error
$\Delta\theta_c$	sampling resolution of the geocentric angle
Δd_{DEM}	sampling resolution of the terrain profile
Δd_{jitter}	error component due to local clock jitter
Δd_{pos}	aircraft RMS positioning error
$\overline{\Delta d_{pos}}$	sample mean of the positioning error
Δd^{max}_{pos}	sample maximum of the positioning error
Δd^{min}_{pos}	sample minimum of the positioning error
$\Delta d^{p\%}_{pos}$	$p\%$ sample percentile
$\Delta d_{quantisation}$	error component due to pulse quantisation
$\Delta d_{sampling}$	error component due to sampling timing ambiguity
Δd_{SNR}	error component due to pulse detection ambiguity
Δd_{sync}	error component due to system synchronisation
Δd_{TDoA}	RMS TDoA accuracy associated with a pair of GSs
Δd_{ToA}	RMS ToA accuracy associated with a GS
Δd_{SNR}	error component due to pulse detection ambiguity
$\Delta d_{sampling}$	error component due to sampling timing ambiguity
$\Delta d_{quantisation}$	error component due to pulse quantisation
Δd_{jitter}	error component due to local clock jitter
Δd_{sync}	error component due to system synchronisation
Δd^2_{ee}	variance of the aircraft positioning estimates in the East direction
Δd^2_{nn}	variance of the aircraft positioning estimates in the North direction
Δh_{geoid}	geoid undulation with respect to the Earth ellipsoid
Δf_{rc}	radio-channel bandwidth
Δh^A_{GS}	difference between aircraft and GS height

$\Delta t_{sampling}$	sampling interval
$\sqrt{\overline{\varepsilon^2}}$	root mean squared error
θ_A	polar angle on the aircraft's antenna pattern
θ_{GS}	polar angle on the GS's antenna pattern
θ_c	geocentric angle between the GS and the aircraft
λ_0	carrier wavelength
λ_A	geodetic longitude of the aircraft
λ_{GS}	geodetic longitude of the GS
$\lambda_{A/GS,t}$	t^{th} geodetic longitude sample along a great circle arc
λ_m	m^{th} geodetic longitude sample
$\boldsymbol{\rho}_k$	aircraft LoS unit vector associated with the kth ground station
$\sigma_{\Delta d_{pos}}$	sample standard deviation of the positioning error
$\boldsymbol{\Sigma}_{ecef}$	covariance matrix of the aircraft ECEF positioning estimates
$\boldsymbol{\Sigma}_{enu}$	covariance matrix of the aircraft ENU positioning estimates
$\boldsymbol{\Sigma}_{tdoa}$	covariance matrix of the TDoA estimates
υ	degree of the Fresnel zone
ϕ_A	geodetic latitude of the aircraft
ϕ_{GS}	geodetic latitude of the GS
$\phi_{A/GS,t}$	t^{th} geodetic latitude sample along a great circle arc
ϕ_n	n^{th} geodetic latitude sample
$\psi_{A/GS}$	azimuth of the great circle arc at the aircraft location
a	ellipsoid's semi-major axis
$\boldsymbol{A}$	sample vector
A_i	i^{th} sample in $\boldsymbol{A}$
b	ellipsoid's semi-minor axis
B_w	effective bandwidth of the preamble pulses
c	light speed in vacuum
d	radio-path length
d_a	largest dimension of the antenna
d_{ff}	far-field border distance of an antenna

$d_{P,A}$	distance of a point P in the radio link to the aircraft
$d_{P,GS}$	distance of a point P in the radio link to the GS
d_{RH}	maximum link length
$\mathbf{D}$	design matrix
D_{GDOP}	Geometric Dilution of Precision
e	ellipsoid's eccentricity
E_b	signal energy per bit
f_0	carrier frequency
F	noise figure
$F_{\upsilon,P}$	υ^{th} Fresnel zone radius at a point P of the radio link
G_r	gain of the receiving antenna
G_t	gain of the transmitting antenna
$h_{A,MSL}$	aircraft height above mean sea level
$h_{GS,MSL}$	ground station height above mean sea level
h_{HAE}	geodetic height
h_{MSL}	height above mean sea level
H_b	breakpoint parameter of the simplified refractivity model
$\mathbf{I}$	identity matrix
$\bar{k}$	average refraction parameter
L_{bf}	free-space basic transmission loss
L_p	propagation model path loss
$L_{p\ total}$	total path loss
L_{Rx}	losses in the receiver system
L_{Tx}	losses in the transmitter system
$M_{F\ FF}$	fast fading margin
$M_{F\ SF}$	slow fading margin
M_I	implementation margin
M_{net}	net link margin
N	total noise power
N_c	maximum number of errors allowed for a correct demodulation

N_s	average surface refractivity
N_0	noise power density per Hertz of noise bandwidth
N_λ	number of discrete geodetic longitude samples
N_ϕ	number of discrete geodetic latitude samples
N_A	number of samples in A
N_b	number of errored bits in the message
N_{bl}	message bit-length
N_{GS}	number of ground stations
N_{obs}	number of observations
N_{par}	number of parameters
$p\%$	percentage for a given case
p_{Exp}	PDF of the shifted exponential distribution
P_e	bit error probability
$P_{e\,DL}$	downlink bit error probability specification
$P_{e\,UL}$	uplink bit error probability specification
$P_{e\,N_b\,N_{bl}}$	probability of having exactly N_b errored bits in an N_{bl} bit block
$P_{e\,N_c\,N_{bl}}$	block error probability
P_{EIRP}	Effective Isotropic Radiated Power
P_{Rx}	carrier input power at the Rx
$P_{Rx\,min}$	receiver sensitivity
P_{Tx}	transmitter output power
Q^{-1}	inverse Gaussian Q-function
$\mathbf{r}_{ECEF}$	tree-dimensional ECEF Cartesian coordinates
r_A	effective distance of the aircraft's antenna to the Earth's centre
r_{GS}	effective distance of the GS's antenna to the Earth's centre
R^2	coefficient of determination
R^2_{adj}	adjusted coefficient of determination
R_b	data bit rate at the baseband output
R_{Earth}	Earth's mean radius
R_e	effective Earth radius

R_{ew}	ellipsoid radius of curvature in the prime vertical (east-west orientation)
S	sample standard deviation
$\mathbf{T}_{enu}^{ecef}$	coordinate transformation matrix from ECEF to ENU coordinates
tr	trace of a square matrix
$\mathbf{x}$	aircraft ECEF coordinates
$\mathbf{x}^k$	k^{th} ground station ECEF coordinates
x_0	translation parameter of the shifted exponential distribution
$\widehat{x_0}$	maximum likelihood estimate for x_0
$\overline{x_n}$	shape parameter of the shifted exponential distribution
$\widehat{\overline{x_n}}$	maximum likelihood estimate for $\overline{x_n}$
y_i	i^{th} observed value
$\hat{y}_i$	i^{th} predicted value
$\bar{y}$	arithmetic average of the observed values

List of Software

Adobe Photoshop CC 2016   Raster graphics editing software

Antenna Magus 2016   Antenna design and modelling software

CST STUDIO SUITE 2016   Electromagnetic simulation software

Google Earth   Map and geographical information software

MATLAB R2016a   Numerical simulation software

Microsoft Excel 2016   Spreadsheet software

Microsoft Visio 2016   Diagramming and vector graphics software

Microsoft Word 2016   Word processor software

Chapter 1

Introduction

This chapter provides a brief impression of the work under study. An overview of the subject is presented and the motivations are established. At the end of the chapter, the work structure is provided.

1.1 Aeronautical surveillance paradigm

Flying is a manifest result of humanity's pioneering spirit and ambition; and is still today a symbol of freedom and economic success, inspiring and fascinating new generations. The air transport service, the end product of the civil aviation industry, is closely linked with economic development, acting as a catalyst as well as a driver in an economy. Aviation is estimated to generate more than 62.7 million jobs worldwide, representing a global economic impact of €2.5 billion, 3.5% of the World's Gross Domestic Product (GDP), with considerable catalytic and induced effects on social, economic, and scientific development [1]. The link between a country's GDP and the investment in air transportation is explored in many of the world's largest economies, where this industry is known to be resilient to economic recession and has a massive impact on productivity and innovation relative to its size [2].

In a broader sense, air transportation increases the connectivity between urban, business, industry, and tourism hotspots, having a wide economic impact by offering access to markets and travel destinations outside the local community. The industry has a crucial role in the economy that goes way beyond tourism, enabling the fast distribution of high value to weight products, supporting just-in-time global manufacturing production and distribution of consumer products, moving fresh produce from developing economies to markets in the industrialised world, providing rapid delivery for e-commerce businesses, and allowing the global access to perishable drugs and vaccines from the pharmaceutical industry. The air transport industry also has an important role in education, research, and business, enabling the exchange of students, large-scale scientific conferences, access to specialised professionals, and strong client relationships [1].

In Portugal, the aviation sector has a considerable economic footprint, with an estimated Gross Value Added (GVA) contribution of €12 000 million, representing 5.6% of the Portuguese GDP, and $260\,000$ jobs, considering both direct, indirect, induced and catalytic economic channels [3]. The industry also creates high productivity jobs, with the average air transport employee estimated to generate €70 000 in GVA annually, a value significantly higher than the average productivity level in Portugal [4].

As the socio-economic benefits of aviation are being increasingly explored by different businesses, industries and individuals, new requirements emerge with the democratisation of the industry, and the need to reduce costs and time. Traditionally, aircraft have been guided through a series of ground based Navigational Aids (NAVAID), such as the Non-Directional Beacon (NDB), the VHF Omnidirectional Radio Range (VOR), the Distance Measuring Equipment (DME), as well as the Instrument Landing System (ILS) and the Microwave Landing System (MLS), flying in long straight line routes from one NAVAID to the next, wasting resources, and misusing winds. Moreover, the aircraft-to-aircraft and aircraft-to-ground communication links had limited capacity, not allowing for real-time air space awareness, limiting the ability to change routes due to weather conditions, wasting human resources, and requiring large safety margins in between aircrafts. Finally, Air Traffic Control (ATC) was constrained by surveillance systems with limited accuracy, capacity and coverage, such as the Primary Surveillance Radar (PSR) and the Secondary Surveillance Radar (SSR), limiting the controller's ability to validate on-board position estimates, and to assess the air space in real time.

The industry's answer to the problem of limited airspace capacity, and the lack of flexibility to change routes to avoid significant weather, or to better take advantage of winds, is the integration of the Communications, Navigation and Surveillance (CNS) infrastructure with Air Traffic Management (ATM). The sustainable development of the infrastructure consists of taking advantage of high-performance aircraft-to-aircraft, aircraft-to-ground, and aircraft-to-satellite digital communication links, moving from ground based NAVAIDs to Global Navigation Satellite Systems (GNSS), and introducing ground based surveillance systems with higher performance.

The key role of GNSS goes beyond navigation, the development of the Automatic Detection and Surveillance-Broadcast (ADS-B) system allows aircraft to transmit their on-board position estimate to other aircraft and to the ATC, increasing the accuracy and update rate of surveillance information. Nonetheless, with the spread and acceptance of GNSS as the primary source for navigation and surveillance, the industry becomes vulnerable to the problems and limitations of this technology. To guarantee the safety levels, and redundancy needs of the industry, a ground-based surveillance system with capacity, accuracy, and coverage comparable to ADS-B, is required; this role being fulfilled by Aeronautical Multilateration (MLAT) systems, such as the Wide Area Multilateration (WAM) system for the en-route airspace, and the Local Area Multilateration (LAM) one for airport approach and surface.

The integration of emerging technologies, such as the Multi-Static Primary Surveillance Radar (MSPSR) for continental surveillance, and Space-Based ADS-B for oceanic and continental ones, with existing technologies, will offer considerable improvements in ATM performance, and long-term cost savings to Air Navigation Service Providers (ANSP).

1.2 Aeronautical multilateration overview

Air Traffic Control must provide expedite, safe, and efficient schemes for the routeing and flow of air traffic. Ever-increasing demands in ATC capacity and efficiency must cope with strict safety requirements; for this purpose, horizontal and vertical separation distances between aircraft must be carefully defined and respected [5]. Under this perspective, surveillance systems must deliver significant improvements in terms of performance and Quality of Service (QoS) [6].

The performance decay with target distance is an important limitation inherent to traditional radar systems, and imposes constraints on coverage, and areas where aircraft can safely manoeuvre. This problem may be overcome by the flexibility of aeronautical multilateration systems, allowing for lower costs and customised solutions regarding surveillance coverage requirements [7]. These systems represent a low-cost distributed surveillance technology, that exceeds the performance of previous solutions in many scenarios, in particular, for mountainous regions or large geographic areas [8].

Aeronautical multilateration systems are used in ATM, for the various types of airspace, allowing the extraction and display of the position and identification of an aircraft, to air traffic controllers. A reply is requested to targets within range, and targets' replies are captured by carefully placed Ground Stations

(GS). Using a telecommunications network, the information retrieved by all receivers is sent to a central processing unit, where targets are identified and positions are determined. Based on the Time Difference of Arrival (TDoA) of a target's reply to at least three GSs, it is possible to determine the target location within a confidence region.

The accuracy of this system depends on the geometry of the problem and, on the technical parameters of the target's transponder and the GS's receiver; namely, their radiation patterns, transmitted power, and sensitivity. In general, the accuracy of the system is defined by the Mean Square Error (MSE) of the location. The desired capacity and separation minima between aircraft set the minimal performance parameters of the system. The MSE of the location needs to be lower than a given threshold to comply with these requirements.

LAM systems are an essential element for Advanced Surface Movement Guidance and Control Systems (A-SMGCS) in airport surveillance, allowing for the monitoring of aircraft and vehicle movements on the airport's surface, replacing radar-based systems, such as the Surface Movement Radar (SMR). Contrary to radar solutions, LAM systems offer tailored coverage, combined with the ability of uniquely identifying all aircraft and vehicles on the airport surface, equipped with ATC transponders [7].

In WAM, the distance between adjacent receiver sites, otherwise known as system baseline, can go up to $100\,\mathrm{km}$, allowing for a coverage area larger than that of SSR and PSR radars. The small receivers can be mounted on offshore drilling platforms, or spread over mountainous regions, offering coverage where it would be impossible to install a radar.

NAV Portugal E.P.E. is the Portuguese ANSP, its mission being "to ensure the provision of safe and efficient air navigation services, while contributing to the creation of value and well-being of society, thus playing a vital role in the aviation sector" [9]. NAV is committed to the deployment and maintenance of surveillance systems to ensure airspace capacity, coverage, and aircraft accuracy location. The Portuguese aeronautical surveillance network must comply with national and international recommendations and standards; they define the performance parameters for the various systems, including redundancy requirements. Aeronautical multilateration systems must offer redundancy at the system level, for safer management of the air space. Nationwide, NAV has several of these systems deployed, and is planning the installation of a new system for the south region of Portugal.

1.3 Motivation, novelty, and content

Aeronautical multilateration systems are acquired by ANSPs, through public procurement contracts, to ATM systems manufacturers, such as Comsoft Solutions, Era Corporation, Indra Sistemas, Saab Sensis Corporation and Thales Air Systems. System manufacturers provide optimised solutions subject to several requirements, such as possible GS sites, radio coverage, target location accuracy, target capacity, and delay. These solutions are tailored to a specific scenario; details about the solution performance, and the optimisation techniques employed, not being usually disclosed by contractors.

ANSPs, such as NAV Portugal, require simulation tools to validate proposals during a tender process, to estimate system coverage concerning aircraft location accuracy, and to estimate the installed system resilience to GS malfunction.

The aim of this dissertation was to develop a model and a simulation tool for the analysis of performance of WAM systems. The proposed model considers the GSs' location, their antennas radiation patterns, transmitted power, receiver sensitivity, and the corresponding parameters for the aircraft. Line-of-Sight (LoS) conditions are assessed considering a Digital Elevation, Fresnel's Ellipsoid, and the Effective Earth's Radius Models. The Free-Space Path Loss Model is used, with fading margins being set to model the power oscillations due to multipath, and the aircraft orientation uncertainty. Aircraft accuracy location is estimated from the system's Geometric Dilution of Precision (GDoP), considering the error components due to tropospheric delay, multipath, receiver noise, quantisation, and clock bias.

The key innovation of this thesis is a system model for coverage estimation, considering propagation, as well as aircraft location accuracy requirements. The proposed model has two main components, a Propagation Model (PrM), for cumulative radio coverage estimation; and, an Error Model (ErM), for accuracy coverage estimation. The PrM model's main innovations include the integration of a Simplified Exponential Refractivity Model, for the estimation of the average refraction parameter; and, the integration of a Digital Elevation Model, for the estimation of the terrain profile. Moreover, two important inputs for the model are obtained in this thesis: the required CNR, at a GS receiver; and the statistical model of the ATC transponder antenna mounted on the aircraft. The ErM model main innovations include the integration of models for the positioning error due to geometry effects, receiver noise, signal bandwidth, and quantisation, as well as average values from the literature for the error components due to tropospheric delay, multipath, and clock bias.

The thesis is divided into five chapters, including this Introduction. Chapter 2 provides the fundamental concepts of aeronautical surveillance, focusing on multilateration systems, and the state of the art. Chapter 3 concerns the proposal, description, implementation, and assessment of the model for the analysis of aircraft accuracy location in aeronautical multilateration systems. Chapter 4 provides the description of the scenarios for the performance analysis, and the analysis of solutions and of their implementation. Chapter 5 finalises the thesis, providing the main results from the work, conclusions from the various chapters are presented, and recommendations for future implementations of aeronautical multilateration systems provided. Additional material and information related to this study may be found in the appendices of this thesis.

Chapter 2

Fundamental concepts and state of the art

This chapter provides the fundamental concepts of aeronautical surveillance, focusing on multilateration systems. It begins with an overview of surveillance systems for air traffic control. Then, a study of multilateration systems is performed, with emphasis on performance parameters and technical limitations. Lastly, the state of the art, with previously published work on the question of this thesis, is presented.

2.1 Aeronautical surveillance systems

In this section, an assessment of surveillance systems for ATC is presented, based on [10] and [11]; a brief comparison of the considered aeronautical surveillance systems being shown in Table 2.1. The surveillance systems for ATC include the PSR, the SSR, the ADS-B system, and the MLAT system.

Table 2.1 – Comparison of surveillance systems (adapted from [12]).

Surveillance System	On-board equipment required?	Interrogation required?	Data measured by surveillance system?
PSR	No non-cooperative	Yes active	Yes independent surveillance
SSR	Yes cooperative	Yes active	Yes (partly) partly independent surveillance
Mode A/C MLAT	Yes cooperative	Yes active	Yes (partly) partly independent surveillance
Mode S MLAT	Yes cooperative	No passive	Yes (partly) partly independent surveillance
ADS-B	Yes cooperative	No passive	No dependent surveillance

The PSR is a ground-based, centralised, non-cooperative, independent, surveillance system; based on the estimation of the round-trip delay, between the transmission of a pulse, and the reception of its reflection from a passive reflecting body. The coverage volume is usually segmented into cells, with spatial resolution defined by two components; the range resolution, inversely proportional to the pulse width; and, the angular resolution, defined by the product between the main-lobe beamwidth and the object range. The system operates by providing estimates, for the range and azimuth of a detected object; it can be shown that the Cramér-Rao Lower Bound (CRLB), or theoretical accuracy of these estimates, is subject to the Signal-to-Noise Ratio (SNR), the effective bandwidth of the signal, and the antenna main-lobe half-power beamwidth [13]. Other sources of error should not be neglected, including the errors obtained during the assessment of the radar's coordinates and azimuth; unwanted movement of the radar due to wind, or temperature variations; presence of objects in the antenna's neighbourhood; the geometric and atmospheric models, used to compute the detected object location; errors due to interference; and, the target Radar Cross Section (RCS) [14]. The system should operate at a frequency where geometrical optics is valid; in other words, the electrical size of the object to be detected should be much larger than the signal wavelength. Three different frequency bands are used, depending on the type of airspace and associated path-loss limitations: the L-band, $[1\,215, 1\,350]\,\mathrm{MHz}$, is usually reserved for en-route ($200\,\mathrm{NM}$); the S-band, $[2.7, 3.1]\,\mathrm{GHz}$, is usually used for approach ($60\,\mathrm{NM}$); the X-band, $[8.0, 12.0]\,\mathrm{GHz}$, is used for airport surveillance and landing ($10\,\mathrm{NM}$). The system is particularly vulnerable to interference due to the detection of unwanted backscatter, also known as radar clutter, from the terrain, sea surface, rain, and wind farms. The PSR system is mostly used for airspace intruder protection, and non-cooperative aircraft management and detection, due to its interference sensitivity, lack of aircraft identification, and lack of precise altitude information [10], [11].

The SSR is a ground-based, centralised, cooperative, independent, surveillance system, based on the transmission and subsequent reception of a reply from an airborne transponder. The system differs from the PSR radar in the sense that an active response is required; the transmission and reception are performed at distinct frequencies; and, the round-trip delay estimation must now account for a standardised delay, that is set in the aircraft transponder [15]. The ground system consists of a rotating directive antenna, usually placed together with the en-route PSR radar, which transmits interrogation messages at $1\,030$ MHz, and receives transponder replies at $1\,090$ MHz. The interrogation, and reply messages, are used to locate the cooperative aircraft, and to exchange relevant information. Accuracy and resolution underlying effects are similar to those of PSR. Depending on the operation mode selected, by the ground equipment, the SSR can request the aircraft's 4-digit octal identity code, entered by the pilot (Mode A), or its barometric altitude information (Mode C). Mode A only supports $4\,096$ individual identity codes, which may represent a capacity limitation in busy airspaces; Mode C supports altitude reports in 100 ft (30.48 m) increments, which may represent a limitation in terms of altitude accuracy.

Mode S was developed as an improvement to Modes A and C; it allows to select a specific aircraft to enquire, reducing interference, and enabling a higher bitrate communication channel. By doing so, besides the standard information from Modes A or C, the Mode S transponder reply can also carry several aircraft parameters through the data link, including the aircraft unique 24 bit address (over 16 million individual identity codes), barometric altitude with a resolution of 25 ft (7.62 m), aircraft status, bank angle, magnetic heading, and track angle [15].

ADS-B is a surveillance system that allows for an aircraft to continuously broadcast several information parameters to the ATC on the ground (ADS-B Out), and to other suitably equipped aircraft in range (ADS-B In). The standard transmission signal may include the aircraft's unique 24 bit address, its velocity, its pressure-altitude information, and its geographical position. ADS-B depends on pre-established systems to gather and broadcast this information: the geographical position information is retrieved through the on-board Global Navigation Satellite System (GNSS) receiver, and the information broadcast may be done through the ATC Mode S transponder. A simple pole antenna is a suitable receiving GS, thus making this system rather simple and inexpensive compared to radars. Additionally, ADS-B allows for higher refresh rate, contrary to PSR and SSR, for which the radar sweep rotational speed constrains the refresh rate of information.

Space-based ADS-B is an emerging technology for global satellite coverage of ADS-B Out, based on the Low Earth Orbit (LEO) Iridium NEXT constellation. Similar to ground-based ADS-B, the system relies on on-board navigation systems to determine, amongst other data, the aircraft's position, velocity, and predicted route; reporting this information to the ATC centre in charge, through a satellite link, with bearable delay and refresh rate.

Aeronautical multilateration is a ground-based, independent, and cooperative, scheme of hyperbolic positioning, that exploits the regular ATC transponder replies, independently locating the transmitting aircraft. The aircraft's position is determined by means of the Time of Arrival (ToA) of the transmitted reply to a network of fixed receivers on the ground; the Mode A/C/S/ES report allows for the identification

of the signal arriving at each GS. The received reports are time stamped and sent, by means of a telecommunications network, to a central processing unit where a TDoA algorithm is applied. If at least four GSs (receivers) acquire a transponder reply, then it is possible to define hyperboloid surfaces, of constant distance difference, between the aircraft and each pair of receivers; their intersection corresponding to the aircraft's position. The MLAT positioning system makes use of information retrieved by GSs, that capture SSR replies and ADS-B data, exploiting signals from well-stablished systems, to provide surveillance and air traffic management. Several GSs are required to guarantee coverage, assure minimum accuracy requirements, and resilience to receiver malfunction.

2.2 Basic aspects of multilateration systems

Aircraft are equipped with transponders constantly transmitting information; by exploiting these signals, measuring the TDoA of these waveforms, to receivers on the ground, it is possible to estimate the transmitter's position. Aeronautical multilateration systems exploit the radio interface of existing technologies, such as the SSR and ADS-B Out systems; integrating the Mode A/C/S/ES data transfer capabilities, with an independent method for locating the aircraft, and validate its reported position.

The uplink interrogation channel operates with a $1\,030\,\mathrm{MHz}$ carrier, with an emission mask of $21.5\,\mathrm{MHz}$ [16]; being used to interrogate cooperative aircraft in range [17]. Different modulation schemes are used, depending on the selected interrogation mode. Modes A and C interrogations, consist of two rectangular pulses, of $0.8\,\mathrm{\mu s}$ width; the separation interval between the two pulses being used by the GSs to inform the interrogated transponders of the selected mode. For Mode A, an interval of $8 \pm 0.2\,\mathrm{\mu s}$ is used, while Mode C is selected with an interval of $21 \pm 0.2\,\mathrm{\mu s}$. Under these operation modes, the interrogation message is unaddressed, and all the aircraft in range are interrogated. Mode S allows discrete interrogation of an aircraft; for this purpose, following a two-pulse preamble, an additional Differential Phased Shift Keying (DPSK) modulated data block is sent, carrying the address of the selected aircraft [17]. This mode enables a considerable reduction of interference in the channel. The transmitter power depends on the intended coverage, and it is not usually disclosed by the manufacturers; nonetheless, one should expect a value that guarantees balance with the downlink.

The downlink reply channel operates at $1\,090\,\mathrm{MHz}$, with a $-20\,\mathrm{dB}$ bandwidth of $14\,\mathrm{MHz}$ [16], being used to locate and identify cooperative aircraft in range [17]. The transponder reply message is identical for all operation modes, consisting of a preamble with four $0.5\,\mathrm{\mu s}$ rectangular pulses, followed by a Pulse Position Modulated (PPM) data block. The data block bitlength varies with the operation mode: for Modes A and C, it has $12\,\mathrm{bit}$; and for Mode S, it can have $56\,\mathrm{bit}$ or $112\,\mathrm{bit}$. The transmitter power varies between $48.5\,\mathrm{dBm}$ and $57\,\mathrm{dBm}$, depending on the aircraft class [17].

The multilateration system relies on the downlink reply, to locate and identify the transmitting aircraft; for this purpose, the GS receiver; the telecommunications network supporting the system; and the central processing unit, where positions are estimated and aircraft tracked; are all important components

that affect system performance, in terms of coverage, accuracy, capacity, and delay.

Hyperbolic positioning consists of measuring the TDoA of a signal, between strategically distributed pairs of sensors; in aeronautical multilateration, this location method being used as follows. An aircraft transponder broadcasts a signal, traveling through different propagation paths, to a distributed network of sensors, corresponding to the MLAT system GSs. In each receiver, the signal is converted to baseband, and digitised. The receiver's IF filter bandwidth, noise factor, and quantisation resolution, have a critical role in the theoretical accuracy of the system. Because of the different propagation paths, the signal, transmitted by the aircraft transponder, arrives at slightly different instants of time at each GS. In a system with N_{GS} GSs, it is possible to define $N_{GS} - 1$ independent nonlinear TDoA equations, each representing a hyperboloid surface.

In general, the system of equations is overdetermined, that is, at least three hyperbolic equations, associated to four receivers, are available, allowing the estimation of the three unknown aircraft coordinates. It is also possible to attain this calculation with only three receivers, through the replacement of one of the hyperboloids, by a horizontal plane [18], [8]. In this scenario, the system should get hold of the aircraft's barometric height, as the target's altitude defines the height of the horizontal plane; this information is usually available from a Mode C, or S, message.

Hyperbolic positioning is done over random variables, meaning that the TDoA from a pair of GSs, provides not a surface, but rather a confidence region around a hyperboloid surface; therefore, the intersection of these regions does not give a single point in space, where the aircraft can be located, but rather a confidence volume. Accuracy location of aircraft using multilateration, becomes subject to the problem geometry, and, for every position calculation, it requires the use of GSs that minimise the position error. Regular synchronisation of the receivers' clocks is required, to minimise the error associated with the clock offset, in each receiver; moreover, a precise assessment of the positions of the GSs is key, when defining the nonlinear hyperbolic system of equations.

The errors inherent to the position estimate, can be categorised, in terms of their statistical nature, into systematic, correlated, and random errors [5], [19], [20], [21]:

- Systematic errors – Errors in this category are considered constant or slowly varying with time, and cannot be eliminated in the location estimator, by repeating measurements, or by averaging several observations. These errors affect every TDoA measurement, and are typically caused by imperfect receiver measurements, relative GS synchronisation errors, and inaccuracies in the GSs' position assessment. The correction of systematic errors, in WAM, can be achieved by means of opportunity traffic transmissions, i.e., signals transmitted from aircraft within the system coverage zone, as described in [22] and [23].

- Correlated errors – Errors in this category are also considered slowly time variant, but only affect TDoA measurements in particular regions, and are typically caused by multipath. These errors can be identified, monitored, and attributed, to problematic regions.

- Random errors – Errors in this category have a white noise behaviour, and are attributed to noise at the received signals, quantitatively described by the SNR, and to quantisation errors in the digitisation process of the incoming signals.

In [19], the author performs an error investigation, and characterisation, for MLAT systems, classifying errors in terms of their origin: signal propagation errors (propagation errors, potential errors, instrumental errors), TDoA or timing errors, signal corruption, algorithm errors, and survey errors.

In [24], the author studies the optimisation of MLAT systems, characterising the error sources for WAM in external and internal sources, Figure 2.1.
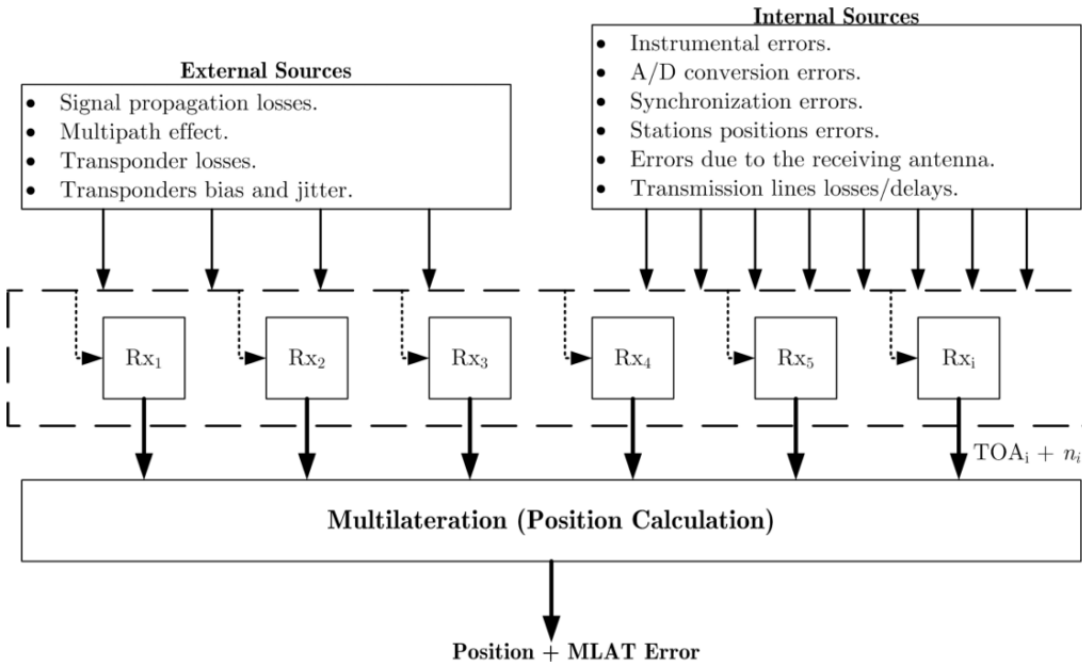
Figure 2.1 – Error sources classification for MLAT systems (adapted from [24]).

There are two fundamental TDoA estimation techniques [11], [25], [26]:

- ToA correlation – Using matched filter techniques, ToAs are estimated in each sensor, and subsequently transmitted to a central processing unit. The TDoA estimator is simply the analytical difference between a pair of ToAs. This procedure is appropriate for signal waveforms where a defined pulse edge can be easily measured; as is the case with the preamble pulses in aircraft transponder signals.

- Cross-correlation – The signals received by each sensor are digitised, time stamped, and transmitted to a central processing unit, where a correlation function estimates the time difference between pairs of sensors. The accuracy of this estimation depends on the type of signal transmitted by the target, and on the signal corruption by the channel; namely, multipath effects. This procedure can be applied for any signal, and is commonly used in Sensor Networks, Wireless Positioning, and Electronic Warfare Support Measures systems. Mode A/C/S transponder signals, do not intrinsically have good auto- or cross-correlation properties; therefore, MLAT systems, based on cross-correlation, must make use of algorithms designed to avoid incorrect or ambiguous results.

Figure 2.2 presents the simplified data flow for a TDoA system, based on ToA correlation. Manufacturers often do not disclose details about their systems; nonetheless, this method is claimed to be the most commonly used for aeronautical multilateration [11].
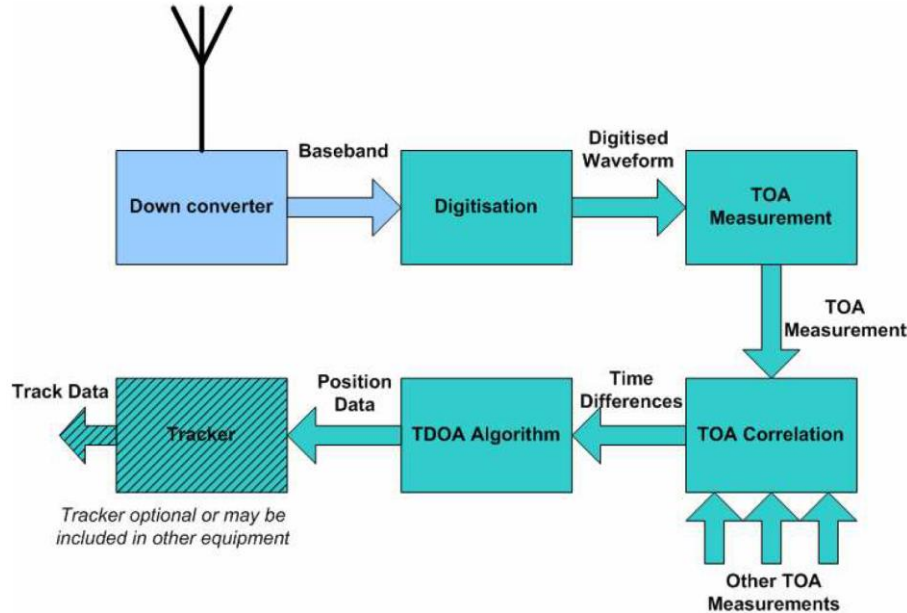
Figure 2.2 – Simplified data flow for a TDoA system based on ToA correlation (adapted from [11]).

The blocks presented in Figure 2.2 have the following functionalities:

- Down Converter – It converts the received $1\,090\ \text{MHz}$ RF signal to baseband, allowing the digitisation of the signal;
- Digitisation – It digitises the analogue signal, by means of an appropriate Analogue-to-Digital Converter (ADC);
- ToA Measurement – It calculates the ToA of the signals; additionally, the transponder message is demodulated, and used to identify the target;
- ToA Correlation – The ToA estimations are correlated using the target's identification;
- TDoA Algorithm – The correlated and grouped ToA measurements, are applied to a TDoA algorithm, to estimate the aircraft position;
- Tracker – It improves accuracy, by filtering raw position data, and producing an aircraft track; by means of a filtering algorithm, examples including the Extended Kalman Filter (EKF), the Unscented Kalman Filter (UKF), and the Interacting Multiple Model Kalman Filter (IMMKF) [27].

Multi-sensor fusion tracking is a technology that allows the combination of information from several surveillance systems, such as PSR, SSR, ADS-B and WAM, improving the reliability and accuracy of the surveillance network [28]. Examples of such systems are the ATM Surveillance Tracker and Server (ARTAS) developed by EUROCONTROL, [27], [29], and Phoenix developed by the German ANSP Deutsche Flugsicherung, [30].

2.3 Performance parameters for multilateration systems

For a quantitative assessment of the performance of typical operational MLAT systems, one should focus on system compliance with the applicable international standards. The performance

specifications, published by the European Organisation for Civil Aviation Equipment (EUROCAE), are the 'Minimum Operational Performance Specification (MOPS) for Mode S Multilateration Systems for use in A-SMGCS', abbreviated as ED-117 [31]; and, the 'Technical Specification for WAM Systems', abbreviated as ED-142 [32]. ANSP's in Europe, adopt these specifications for their MLAT systems; in summary, the domain of ED-117 is the LAM system, and the domain of ED-142 is the WAM one.

The main performance parameters for MLAT systems are:

- Probability of Position Detection (PD) – The PD is the probability of generating a valid position report, within the parameterised accuracy requirements, on a position update.

- Probability of False Detection (PFD) – The PFD is the probability of generating a report for a false target.

- Probability of Code Detection (PCD) – The PCD is the probability of generating a target report, with a validated, and correct, Mode A/C/S code.

- Probability of False Code Detection (PFCD) – The PFCD is the probability of generating a target report, with a validated, but incorrect, Mode A/C/S code.

- Processing Delay – The processing delay corresponds to the elapsed time, since a reply signal is detected at a GS, and the corresponding target report is generated.

- Target Capacity – This parameter is defined by the number of targets that can be processed by the central processing system, without surpassing the maximum delay for this task.

- Operational System Accuracy – This accuracy is obtained from the MSE, between the positions acquired by the MLAT system, and the measurements provided by a reference system like ADS-B, data from GNSS; or a trajectory reconstruction algorithm, through filtering of the available MLAT data.

- Availability – This parameter corresponds to the probability of the system being able to perform the corresponding function, on a position update, measuring system reliability.

ED-142 [32] covers WAM requirements, in the airspace of Terminal Manoeuvring Area (TMA), and en-route. The update interval is defined differently for these types of airspace, Table 2.2. ED-142 also specifies the conditions for Site Acceptance Testing (SAT), and the testing procedures necessary for the verification and optimisation of WAM. The performance tests include, among others, the evaluation of the system's PD, PFD, PCD, PFCD, and accuracy. The relevant performance requirements are listed in Table 2.3.

Table 2.2 – Defined update intervals in ED-142 (extracted from [32]).

Update Mode	Airspace Type	
	TMA	En-route
Aperiodic	≤ 5s	≤ 8s
Periodic	≤ 4s	≤ 6s

Table 2.3 – ED-142 requirements (extracted from [32]).

Test Parameters	Requirement
Horizontal Position Accuracy – TMA	150 m RMS
Horizontal Position Accuracy – En-route	350 m RMS

Table 2.3 (contd.) – ED-142 requirements (extracted from [32]).

Test Parameters	Requirement
PD	≥ 97.0%
PFD	≤ 0.1%
PCD – Mode S	≥ 99.0%
PCD – Mode A	≥ 98.0%
PCD – Mode C	≥ 96.0%
PFCD – Mode S	≤ 0.1%
PFCD – Mode A	≤ 0.1%
PFCD – Mode C	≤ 0.1%
Processing delay	≤ 1 s
Target Capacity	≥ 250
Availability	≥ 99.99%

2.4 Technical limitations of multilateration systems

The receiver sensitivity is a measure of the ability of a receiver to demodulate, and retrieve information, from a weak signal. Considering that the power of any signal drops with the square of the distance, this parameter dictates the range of each GS, of the multilateration system. The inherent thermal noise, the modulation scheme, and the receiver implementation, define the receiver sensitivity. Moreover, since ToA accuracy is a function of the SNR, which in turn is a function of the receiver sensitivity, sensitivity impacts also on system accuracy [11].

The dynamic range, the ratio between the power levels of the weakest and strongest signals that the receiver system can handle, imposes an important limitation on the ability of the receiver to process signal sources, both relatively near and far from the antenna [11], [33], [20].

The digitisation rate also affects the accuracy of the system; the accuracy of the TDoA estimation improves for higher clock rates. This improvement over the raw measurements, also increases the potential improvements from signal processing, and target tracking algorithms [11].

The propagation delay between the receiver's antenna and digitisation block, must be taken into account for the derivation of the signal ToA [11]. The different propagation delays, inherent to each of the multilateration receivers, give rise to a factor called group time delay, that degrades localisation accuracy. This delay is less significant in distributed clock systems, for which the digitisation process is part of the receiving block; than in common clock ones, for which the digitisation process only takes place after the signal has been transmitted to the central processing unit. The design of the multilateration system must guarantee that delay changes, can either be regularly calibrated, or known, for variations of received power level, frequency, temperature, and ageing of components [11], [34].

The choice of antenna, for the reception of the Mode A/C/S 1 090 MHz signals, is of great importance as its peak gain, beam pattern, and bandwidth, will have a significant influence on the system performance; the peak gain of the antenna, coupled with the receiver's sensitivity, dictates the system

coverage; a careful design of the antenna beam pattern, enables a system with uniform coverage and tolerance to multipath; careful choice of bandwidth, limits out of band noise and interference [11].

Systems relying on GNSS synchronisation, have a dedicated antenna to receive the satellite signals; an appropriate antenna must be chosen to minimise the effects of multipath and interference.

Multipath, interference, jamming, and garble, can corrupt the transponder signal received by the system. Recovery mechanisms may be enough to retrieve the aircraft identification; however, the deformation of the signal, disturbs the accuracy of the ToA measurement [19]. Rejection of corrupted signals can improve accuracy, but it is done at the expense of the detection probability. Systems implemented in dense signal environments are subject to a higher probability of garble, which must be considered during system design. The probability of detection, and the demodulation ability, are also impaired by a low SNR [11], [19].

Restricted to $1\,090\,\mathrm{MHz}$ signals, multilateration receivers are generally narrow-band; therefore, the system is only particularly exposed to malicious in-band interference; and, to adjacent-channel interference, from unintentional sidebands of other systems [11].

The use of a single omnidirectional antenna is a common approach for the implementation of GSs. This provides a low antenna gain, therefore, a low SNR. The low SNR has a negative impact on some performance parameters; namely, the PD, the PFD, and the robustness to garbling. The system is particularly vulnerable to garbling, as signals are received from every direction [18].

The system baseline is the distance between adjacent GSs, and the radar horizon of multiple receivers must be taken into account [11], [21]. Earth curvature has an important impact on the coverage of the lower flight levels; the low-level coverage of the system is worse for wider receiver baselines [11]. Typical values of $10\,\mathrm{NM}$ to $20\,\mathrm{NM}$, are used to provide low-level coverage [11]. If height information from another source, such as Mode C barometric altitude, is available, it is possible to determine the target position with only three receivers; otherwise, a full three-dimensional solution requires four or more GSs, in LoS with the target's transponder. Therefore, for system design, one must study the impact of terrain, and antenna heights, on system performance [11].

According to [11], [35], [36], and others, the influence of the system geometrical configuration, on the accuracy of the measured position, should use the GDoP as metric. In a hyperbolic system of position determination, GDoP is associated with errors in position, caused by the relative location of transponders and GSs. GDoP varies with the target position, with respect to receivers. Therefore, for the same TDoA error statistics, one may obtain a system accuracy that varies with the target position, and the number and location of GSs involved in the TDoA algorithm [11].

The flight mode influences the aircraft accuracy location [18]; airliners are usually equipped with two antennas for the ATC transponder, one at the bottom part of the aircraft, and one at the top. The transponder system compares the power level of the interrogation signal, received by both antennas, selecting the antenna with the highest received power for the reply. During a turn, the aircraft roll angle is set to the required bank angle, for that turn; this angle can go up to 45°, changing the electromagnetic paths, between the GSs and the transponder on the aircraft. For WAM, one may expect the location of

an aircraft in straight flight, to show an improved accuracy, compared with the location of an aircraft in a curved one. Moreover, the performance of the filtering techniques, used by the tracking system, also deteriorate during trajectory variations, corrupting the tracker ability to filter noisy estimates.

2.5 State of the art

The true position of an object is usually unknown; for this reason, the quality assessment of MLAT systems can be a demanding task. In [18], Pourvoyeur, Mathias, and Heidger, from the German ANSP Deutsche Flugsicherung, suggest that when deploying GSs, within an area already covered by well-understood systems, one should use the existing framework as a reference. It is also stated, that aircraft traffic presents variations along the day, and the year; which influences the volume and characteristics of the available data; therefore, it should be considered during the evaluations of requirement compliance and system performance. In this thesis, in accordance with [18], the analysis of WAM uses, as reference, the position information provided by ADS-B.

Xu et al. [8], carried out a performance assessment, of installed multilateration systems, by manufacturer Era Systems Corporation. Their motivation was to demonstrate the compliance of Era's aeronautical products, with the applicable performance specifications ED-117 [31], and ED-142 [32], published by the EUROCAE. Era uses a scheme of elliptical-hyperbolic positioning, calculating the Time Sum of Arrivals (TSoA), to locate a target in space. This is achieved by making use of an active transmitter, integrated into the multilateration system, to obtain the elapsed time between an interrogation and the reception of a reply. The authors state that this method provides a more accurate position detection, compared with the regular scheme of hyperbolic positioning. Reference [8], also describes a SAT methodology, by making use of flight tests and target of opportunity tests, for the performance evaluation of WAM systems. Flight tests are performed by appropriate aircraft, equipped with Differential Global Positioning System (DGPS) equipment, to achieve a positional reference source, with an accuracy better than $1\,\mathrm{m}$. The flight path for this test is designed in advance, to cross as much of the coverage volume as possible. On the other hand, the target of opportunity tests use information from regular flights, providing a good indicator of system performance for typical flight paths. Table 2.4, contains the observed performance information, gathered during a flight test, for the two airspace scenarios, TMA and En-route.

In [37], the authors developed a tool to analyse the expected performance of local, and wide area, multilateration systems; including an impact evaluation of multipath, by means of a method of ray-tracing based on the Geometrical Theory of Diffraction (GTD). The developed tool also provides the possibility of considering different system architectures, for the evaluation of GDoP and precision error. The output parameters are the radio coverage area of each GS; the number of GSs in LoS, from each point in space; and the GDoP, including its horizontal and vertical components. The input parameters include the terrain profile, a set of available locations for GSs, antenna radiation patterns, thermal noise, and interfering signals.

Table 2.4 – Era WAM, ED-142 compliance analysis (extracted from [8]).

Test parameters	Observed
Accuracy	66.8 m (Terminal)
	139.1 m (En-route)
PD	98.1%
PCD – Mode S	100.0%
PCD – Mode A	100.0%
PCD – Mode C	100.0%
PFD	0.0%
PFCD – Mode S	0.0%
PFCD – Mode A	0.0%
PFCD – Mode C	0.0%
Predicted availability	99.9999%

Lei et al. [38], studied planar distributions for three-dimensional TDoA positioning systems, with the purpose of obtaining the optimal distribution, in terms of GDoP and coverage. A minimum of four sensors is required to solve the TDoA equations, and eight topologies were considered for their distribution above the plane: straight (or Uniform Linear Array (ULA)), trapezoidal, parallelogram, rectangle, inverted triangle (or T-shaped), Wye, lozenge and square (or Uniform Angular Array (UAA) of four sensors). The position error inherent to the eight cases was analysed by means of three-dimensional plots, and contour plots of GDoP. It was shown, that the Wye distribution is preferable, as it presents a smooth and well-behaved GDoP surface, with overall lower position error and higher coverage area, compared to other topologies. The GDoP for the Wye sensor distribution is presented in Figure 2.3; simulations being performed under LoS conditions, with a moving target at 10 km height, a wave propagation speed of 0.3 m/ns, and a TDoA measurement error of 40 ns.

Yang and Scheuing [39], studied the impact of the sensor array geometry, on the accuracy of TDoA-based source localisation, by means of a theoretical analysis of the Cramér-Rao Lower Bound (CRLB). If the measurement errors are Gaussian distributed with zero mean, and TDoA measurements uncorrelated, the authors derive the necessary and sufficient conditions for the optimum sensor array geometry, that minimises the trace of the CRLB square matrix. These conditions result in a set of optimum arrays, for both two- and three-dimensional localisation. The authors suggest UAAs as the optimal two-dimensional sensor placement strategy for source localisation, in the sense that UAAs minimise the trace of the CRLB.

In the context of sonar, radar, mobile communications, and sensor networks, Lui and So [40], studied passive source localisation, using TDoA measurements, from an array of spatially distributed sensors. The focus of the analysis is sensor array geometry design, based on correlated TDoA estimates. For the scenario of signals in additive white Gaussian noise, the authors show that UAAs are an optimum sensor placement strategy, and derive the theoretical minimum achievable accuracy. Furthermore, numerical simulation examples, validating their analytical findings, are also presented. Figure 2.4 displays the simulation results for the position MSE, with a source fixed at the origin, a rectangular test area of dimension $20 \text{ m} \times 10 \text{ m}$, wave propagation speed at 360 m/s, and a four-sensor system with the following placement strategies: UAA, Non-uniform Angular Array (NAA), rectangle (or Corners), L-shape

and ULA. Results suggest that accuracy improves with the uniformity of the baseline between each pair of sensors; UAAs showing an improvement of 2 to $7\,\text{dB}$ compared with other sensor placement strategies.

(a) GDoP surface plot.   (b) GDoP contour plot.
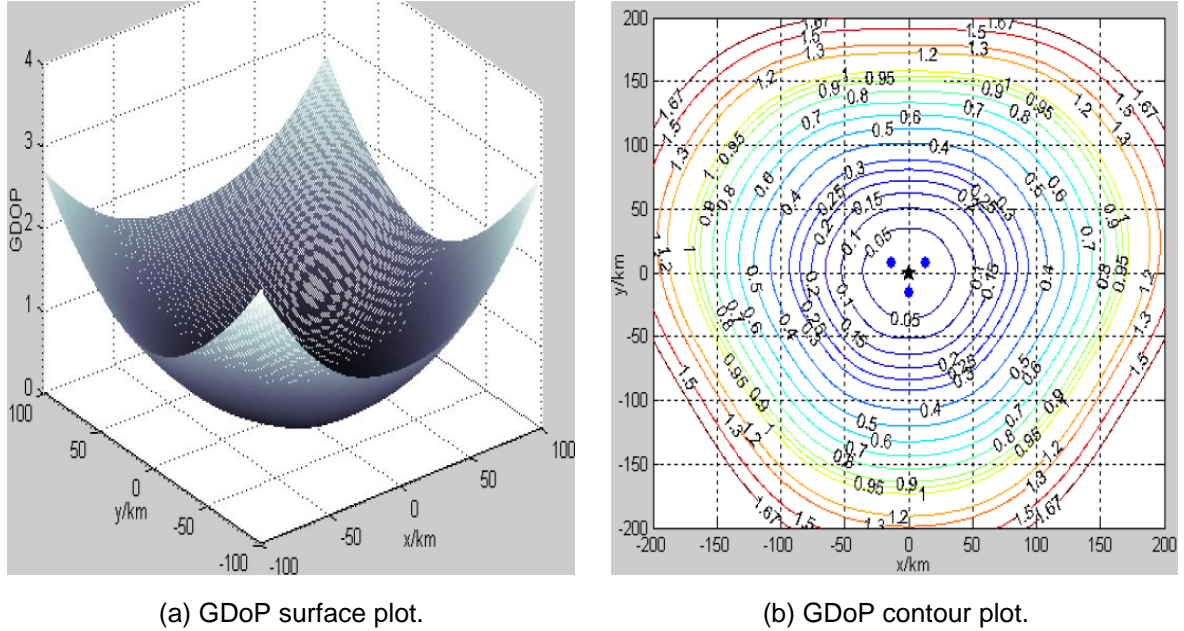
Figure 2.3 – GDoP for a Wye distribution of four sensors (extracted from [38]).

Within the framework of electronic warfare, Meng et al. [41], studied sensor distributions for determining the location of a radar, by means of four aircraft in formation. Taking GDoP as a performance metric, the authors analysed the key factors affecting accuracy, i.e., aircraft formation, or sensor distribution; the relative position of the aircraft chosen as the leader, the reference sensor; and, the length and direction of the baseline. From computer simulations, the authors concluded that the T-shaped and rhombus distributions are ideal for localisation tasks in a specified and narrow area, and that the Wye distribution is preferable for ensuring high and uniform accuracy over a wide area.
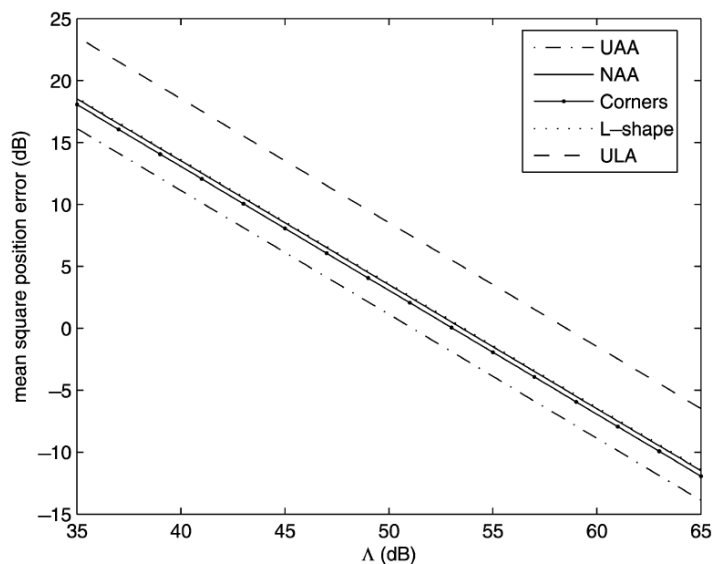
Figure 2.4 – Position MSE for different four-sensor geometries versus SNR (extracted from [40]).

Jiang [42], analysed variations of the T- and Wye distributions for four-sensor TDoA systems. Through simulation, the author explored the sensibility of GDoP to variations on the relative positions of the sensors and the target, arriving at the following conclusions:

- system performance can be improved in a region, at the expense of performance from the remaining coverage area; this is attained by manipulation of the system baseline, in a single direction;
- the Wye distribution is preferable for implementations where performance is expected to be as uniform as possible, or targets have random or unknown trajectories;
- the T-shaped distribution is preferable when targets are to be located along a linear trajectory, and the system accuracy outside that region is not relevant;
- choosing the appropriate reference sensor for TDoA calculations, has a positive effect on accuracy.

An estimation method for aeronautical services basic transmission loss, is presented in Recommendation ITU-R P.528-3 [43]. The method is valid in the frequency range $[125, 15\,500]\,\text{MHz}$, for aeronautical and satellite services, making use of ground-air, ground-satellite, air-air, air-satellite, and satellite-satellite links. The estimation is based on the interpolation of basic transmission loss data, from sets of curves provided in the recommendation. These sets of curves were obtained through computer simulations using the IF-77 Electromagnetic Wave Propagation Model, and depict the relationship of the basic transmission loss with the distance between antennas, the heights of the antennas above mean sea level, the frequency, and the time availability. The IF-77 simulator is carefully described in [44].

The Distance Measuring Equipment Tracer (DEMETER) is a software tool from EUROCONTROL [45]; which supports the implementation of Performance Based Navigation (PBN), and the optimisation and rationalisation of the navigation infrastructure. The tool allows to assess the spatial performance of DME and VOR systems, concerning coverage and redundancy. DEMETER is used by ANSPs in most European Civil Aviation Conference (ECAC) member states, as well as globally by other organisations, including research institutes and universities [45]. DEMETER's main features and functionalities, include the flexibility to import airspace elements in .csv format, an integrated terrain database, co-channel separation assessment, and coverage calculations based on LoS, Free-Space Path Loss, and Diffraction, propagation models. The tool does not offer the capability to assess MLAT systems in terms of cumulative radio and accuracy coverage.

The airframe shadowing depth depends on the roll angle, the antenna's location, the aircraft's outline, and the aircraft's electrical size, compared with the signal wavelength. The authors of [46], studied the effects of the airframe shadowing in the L-band, for a carrier centred at $968\,\text{MHz}$, and two antenna locations, on the bottom of a S-3B Viking aircraft, describing an U-shaped trajectory, at $580\,\text{m}$ above ground. When considering an antenna placed forward to the wings, the authors found that for roll angles between 5° and 30°, the typical fading depths caused by the aircraft's wings, range between a minimum of $2.6\,\text{dB}$ and maximum of $25.5\,\text{dB}$; the average shadow loss, during the $1\,\text{hour}$ measurement campaign, being $10.3\,\text{dB}$ with a standard deviation of $4.4\,\text{dB}$.

Chapter 3

Models and

simulator description

This chapter concerns the proposal, description, implementation, and assessment of the model for the analysis of aircraft accuracy location in aeronautical multilateration systems. The chapter starts with a cursory description of the theoretical model, offering an overview of its aims and assumptions. Subsequently, a more detailed description of the sub-models is provided, followed by the development of the statistical model for the positioning error. Next, the implementation of the developed model is fully described, with detailed flowcharts being shown for the algorithms realised in the simulator. Finally, the chapter ends with a thorough assessment of results from the model by comparison with data from the literature, and from previously implemented systems.

3.1 Model development

The purpose of this section is to describe the theoretical models employed in solving the research problem of this dissertation.

3.1.1 Model overview

A multilateration system is defined by an operational coverage volume within which QoS specifications are met. QoS regulation consists of several mandatory performance specifications, such as, accuracy, detection probability, capacity and processing delay [32]. This dissertation addresses the study of aircraft accuracy location in aeronautical multilateration systems, the proposed model providing a framework to study and estimate the coverage volume, considering system accuracy and detection probability specifications. Figure 3.1 presents the outline of the proposed model, with the constraints, specifications, and steps required to estimate the operational system coverage in terms of aircraft accuracy location and detection probability.

Design constraints

Number and location of ground stations

Performance regulations

Probability of detection
Horizontal accuracy

Implementation constraints

Terrain profile
Antenna patterns
Receivers' noise figure

Model

Propagation modelling and coverage analysis

Error modelling and accuracy analysis

Resilience analysis

Output

Theoretical coverage
Theoretical accuracy
System resilience

Analytically determined parameters

- Free-space basic transmission loss
- Fresnel ellipsoid radius
- Effective earth radius
- Orthodromic distance

- Expected signal-to-noise ratio
- RMS ToA error
- RMS TDoA error
- RMS positioning error

Figure 3.1 – Model overview.

Taking a set of possible GSs' sites, one defines the geographic volume within which the system complies with the minimum performance specifications, by discretising this volume in terms of possible aircraft coordinates, and checking, for each possible coordinate, if the minimum performance specifications are met. The flowchart of the model has 3 elementary steps, that should be run for each one of the

considered aircraft coordinates:

- Coverage analysis – With a Propagation Model (PrM), and considering the minimum probability of detection specification, estimate the GSs that effectively detect the aircraft.
- Accuracy analysis – With an Error Model (ErM), and considering the minimum positioning accuracy specification, check if the aircraft coordinate is effectively covered by the system.
- Resilience analysis – Considering the results from the PrM simulations, generate all the $N_{GS} - 1$ and $N_{GS} - 2$ combinations of GSs that effectively detect the aircraft, and, for each combination, reapply the ErM model to check if the aircraft coordinate is covered by the system.

The performance specifications considered for this assessment are the horizontal positioning accuracy and the detection probability, aircraft capacity and processing delay not being considered. The developed model reduces the aircraft to a point target in an horizontal plane parallel to the Earth, disregarding the yaw, pitch and roll angles. GSs are assumed to lie on the ground within fixed and limited positions. All sensors are assumed equal, with known noise factor, sensitivity, and height Above Ground Level (AGL). Radiation patterns are assumed to be omnidirectional in the horizontal plane and with known behaviour in the vertical one; their local spherical coordinate systems being always assumed to have the vertical axis normal to the Earth's surface with the cone of silence pointing upwards for the GSs, and downwards for the aircraft. Unless specified, geographic coordinates are referenced to the 1984 World Geodetic System (WGS84) with heights referenced to the 1996 Earth Gravitational Model (EGM96) geoid.

The coverage analysis should be divided into two categories: LoS coverage, and sensitivity coverage. The LoS coverage analysis should consider the terrain profile and the first order Fresnel ellipsoid model to determine if an aircraft and a GS are in view or if their radio-path is blocked by the terrain. On the other hand, the sensitivity coverage analysis is used to determine if the signal arriving to a receiver is above the minimum CNR threshold required to comply with the detection probability regulation.

Accuracy analysis should be divided into three processes, i.e., error models: RMS ToA, RMS TDoA, and RMS positioning. The RMS ToA error model estimates the ToA error associated with each GS-aircraft link, considering the expected SNR and the signal bandwidth. The RMS TDoA error model measures the TDoA error associated with each of the possible GS pairs that are used to estimate the aircraft position. The RMS positioning error model takes into consideration the RMS TDoA error estimates and the geometry of the GSs network to estimate the positioning error associated with the given aircraft coordinate.

The model should aim at providing an estimation of the effective system performance. Operational performance may vary due to the considered approximations and simplifications. In what regards the accuracy analysis, the model only provides a lower bound for this parameter (the CRLB), operational system accuracy being usually worse. An assessment of this estimate is provided in Section 3.4.

WAM uses $1\,030\,\text{MHz}$ for the ground-based uplink interrogations, with an emission mask of $21.5\,\text{MHz}$. Downlink replies are transmitted by the aircraft's transponder at $1090\,\text{MHz}$, with a $-20\,\text{dB}$ bandwidth of $14\,\text{MHz}$ [16].

3.1.2 Propagation model

This subsection deals with the description of the propagation model used to estimate the operational conditions of the radiofrequency link between an aircraft and a GS. The essential parameters for this assessment are the received signal strength, the link budget, and the minimum received signal levels that guarantee a reliable operation. The effects due to tropospheric scintillation and gaseous absorption are neglected due to the operating frequency. Also, the receiver's dynamic range and the presence of interference in the channel are not considered. This model has its roots on works done in collaboration with NAV: João Pinto [47], Ricardo Santos [48], Joana Fernandes [49] and Rodrigo Santos [50].

Put simply, the sensitivity coverage model consists of determining if the net link margin is above a defined value. The net link margin provides a measure of the power surplus in the link, between the operating point, and the point where the link can no longer be maintained, being obtained by comparing the expected Carrier-to-Noise Ratio (CNR) with the one that is required to achieve a given detection probability,

$$M_{net\,[dB]} = (P_{Rx}/N)_{expected\,[dB]} - (P_{Rx}/N)_{min\,[dB]} \qquad (3.1)$$

where:

- P_{Rx}: carrier input power at the Rx,
- N: total noise power,
- $(P_{Rx}/N)_{expected}$: expected CNR,
- $(P_{Rx}/N)_{min}$: required CNR.

The expected CNR is a measure of the power ratio at the output of the receiver's Intermediate Frequency (IF) filter, before demodulation, and is defined by,

$$(P_{Rx}/N)_{expected\,[dB]} = P_{Rx\,[dBm]} - N_{[dBm]} = P_{EIRP\,[dBm]} - L_{p\,total\,[dB]} + G_{r\,[dBi]} - L_{Rx\,[dB]} - N_{[dBm]} \qquad (3.2)$$

where:
- P_{EIRP}: Effective Isotropic Radiated Power,
- $L_{p\,total}$: total path loss,
- G_r: gain of the receiving antenna,
- L_{Rx}: losses in the receiver system.

The Effective Isotropic Radiated Power (EIRP) is taken as the transmitted power plus the transmitting antenna gain minus any losses in the transmitter system,

$$P_{EIRP\,[dBm]} = P_{Tx\,[dBm]} + G_{t\,[dBi]} - L_{Tx\,[dB]} \qquad (3.3)$$

where:
- P_{Tx}: transmitter output power,
- G_t: gain of the transmitting antenna,
- L_{Tx}: losses in the transmitter system.

The total path loss is the propagation model path loss plus the slow and fast fading margins,

$$L_{p\,total\,[dB]} = L_{bf\,[dB]} + M_{F\,SF\,[dB]} + M_{F\,FF\,[dB]}$$ (3.4)

where:
- L_{bf}: free-space basic transmission loss,
- $M_{F\,SF}$: slow fading margin,
- $M_{F\,FF}$: fast fading margin.

In the proposed model, different approaches are used to deal with the two sources of shadowing commonly found in aeronautical communications:
- Shadowing due to the terrain, which is modelled by only considering radio-paths with a cleared first-order Fresnel ellipsoid, hence no fading margin being associated to this effect.
- Shadowing due to the aircraft's structure, which is modelled by an average far-field elevation pattern obtained for an antenna mounted on an aircraft, plus a slow fading margin associated with the uncertainty about the aircraft orientation.

Fast fading is mostly due to constructive and destructive interference patterns from multipath; in LoS conditions, the aeronautical radio-channel should be mostly dominated by Rician fading; nonetheless, there is no ITU-R recommendation regarding multipath fading for air-ground communications, and no definition for the Rician fading factor to be used in the L-band. In [51] the authors provide an analysis of typical air-ground aeronautical communication system propagation losses in the L-band for a carrier at $972\,\text{MHz}$; regarding the fading due to multipath, the authors suggest a margin of $26\,\text{dB}$, indicating that it guarantees a system availability of 99.99%.

Free-space loss is a good approximation for the L-band basic transmission loss in air-ground communication links, if the first Fresnel zone is cleared of any obstacles and far-field conditions hold [52]. Recommendation ITU-R P.525-2 [53] describes the model for the free-space basic transmission losses for point-to-point links, this model is valid for propagation under LoS conditions, inside Fraunhofer's far-field region, i.e., for distances to the antennas higher than the far-filed distance [54],

$$d_{ff\,[m]} = \frac{2\,d_{a\,[m]}^2}{\lambda_{0\,[m]}}$$ (3.5)

where:
- d_a: largest dimension of the antenna,
- λ_0: carrier wavelength.

Equation (3.5) yields a value well below $1\,\text{m}$, for $1\,090\,\text{MHz}$ and a quarter-wave monopole antenna (typical for ATC transponder systems); in these conditions, free-space basic transmission loss is taken,

$$L_{bf\,[dB]} = 32.4 + 20\log f_{0\,[MHz]} + 20\log d_{[km]}$$ (3.6)

where:
- f_0: carrier frequency,
- d: radio-path length.

WAM is based on the reception of Mode A/C/S/ES transponder signals at $1\,090\text{ MHz}$, (3.6) yielding a value of 73 dB for an aircraft at 100 m of a GS, typical for an aircraft in approach or on the runway, and of 145 dB for an aircraft at FL 400, 12.2 km AMSL, in the radio horizon distance of a GS.

Ignoring environmental noise sources, the total noise power, also known as noise floor or Minimum Discernible Signal (MDS), used in (3.2), is well approximated by,

$$N_{[\text{dBm}]} = -174 + 10\log\Delta f_{rc[\text{Hz}]} + F_{[\text{dB}]} \tag{3.7}$$

where:
- Δf_{rc}: radio-channel bandwidth,
- F: noise figure.

The law of cosines for planar triangles and the Spherical Earth Model can be used to produce estimators for the propagation path length, and for the elevation angles at the antennas. The Spherical Earth Model also has some error, since approximating the Earth ellipsoid by a sphere introduces an error proportional to the Earth's flattening, bellow 1%; this approximation is reasonable for CNR estimation. For succinctness in the presentation of the next models, one starts by defining the following quantities,

$$r_{A\,[\text{km}]} \triangleq R_{e\,[\text{km}]} + h_{A,MSL\,[\text{km}]} \tag{3.8}$$

$$r_{GS\,[\text{km}]} \triangleq R_{e\,[\text{km}]} + h_{GS,MSL\,[\text{km}]} \tag{3.9}$$

$$\Delta h_{GS\,[\text{km}]}^{A} \triangleq h_{A,MSL\,[\text{km}]} - h_{GS,MSL\,[\text{km}]} \tag{3.10}$$

where:
- r_A: effective distance of the aircraft's antenna to the Earth's centre,
- r_{GS}: effective distance of the GS's antenna to the Earth's centre,
- Δh_{GS}^{A}: difference between aircraft and GS height,
- R_e: effective Earth radius,
- $h_{A,MSL}$: aircraft height above mean sea level,
- $h_{GS,MSL}$: ground station height above mean sea level.

The geocentric angle is the one formed by the imaginary straight line that joins two given points with the centre of the Earth, requiring to compute the radio-path length only when the GS and the aircraft geodetic coordinates are known,

$$\theta_{c[\text{rad}]} = \arccos\big(\cos(\phi_{A[\text{rad}]})\,\cos(\phi_{GS[\text{rad}]})\,\cos(\lambda_{A[\text{rad}]} - \lambda_{GS[\text{rad}]}) + \sin(\phi_{A[\text{rad}]})\,\sin(\phi_{GS[\text{rad}]})\big) \tag{3.11}$$

Knowing the altitudes and the geocentric angle between the aircraft and the GS, the radio-path length can be estimated from,

$$d_{[\text{km}]} = 2\,R_{e\,[\text{km}]}\sin\left(\frac{\theta_{c[\text{rad}]}}{2}\right)\sqrt{\left(1 + \frac{h_{GS,MSL\,[\text{km}]}}{R_{e\,[\text{km}]}}\right)\left(1 + \frac{h_{A,MSL\,[\text{km}]}}{R_{e\,[\text{km}]}}\right) + \left(\frac{\Delta h_{GS\,[\text{km}]}^{A}}{2\,R_{e\,[\text{km}]}\sin\left(\frac{\theta_{c[\text{rad}]}}{2}\right)}\right)^{2}} \tag{3.12}$$

This model is numerically better-conditioned than the analytically equivalent obtained by direct application of the law of cosines for planar triangles to the triangle formed by the Earth's centre, the GS, and the aircraft [55].

Taking the Spherical Earth Model, the polar angle at the local spherical coordinate system of the aircraft's antenna, North-East-Down, can be modelled by,

$$\theta_{A\ [\text{rad}]} = \sin^{-1}\left(\frac{\Delta h_{GS\ [\text{km}]}^A}{d_{[\text{km}]}}\left(1 - \frac{\Delta h_{GS\ [\text{km}]}^A}{2\ r_{A\ [\text{km}]}}\right) + \frac{d_{[\text{km}]}}{2\ r_{A\ [\text{km}]}}\right) \tag{3.13}$$

The polar angle at the local spherical coordinate system of the GS antenna, East-North-Up (ENU), can be modelled by,

$$\theta_{GS\ [\text{rad}]} = \sin^{-1}\left(\frac{\Delta h_{GS\ [\text{km}]}^A}{d_{[\text{km}]}}\left(1 + \frac{\Delta h_{GS\ [\text{km}]}^A}{2\ r_{GS\ [\text{km}]}}\right) - \frac{d_{[\text{km}]}}{2\ r_{GS\ [\text{km}]}}\right) \tag{3.14}$$

The propagation path is changed by the atmospheric refractive index gradient; typically, only the vertical component of the gradient is significant, causing radio waves propagating in the atmosphere to bend towards the Earth [54]. The modelling of this behaviour is application dependent; for CNR estimation, it is reasonable to assume that the Earth is spherical, and that the refractive index gradient is constant. This simplified Atmospheric Model may not be valid for highly directive antennas, and for applications requiring highly accurate range and angle estimates, such as, positioning and antenna pointing.

At low altitudes, typically bellow $10\ \text{km}$ ($33\,000\ \text{ft}$) [56], the Effective Earth's Radius Model, or k-Model, can be applied, modelling the troposphere as a single spherical layer with constant refractive index gradient. The practical application of this model consists of considering rectilinear propagation paths in a slightly inflated Earth with radius multiplied by a factor k, which accounts for the refraction phenomena, the effective Earth radius being,

$$R_{e\ [\text{km}]} = \bar{k}\ R_{Earth\ [\text{km}]} \tag{3.15}$$

where:

- $\bar{k}$: average refraction parameter,
- R_{Earth}: Earth's mean radius.

Compared with numerical integration models for the atmospheric refraction, the k-Model introduces an error on the elevation angle estimates, between 0.02° and 0.2°, depending on aircraft altitude and instantaneous atmospheric conditions [57].

Taking the Segmented Bean and Thayer Model for refractivity, it is possible to obtain an approximate one-segment exponential model, valid in some altitude range [57]. The Simplified Exponential Model for refractivity used in this thesis is defined to cross the Segmented Bean and Thayer Model in two altitude points, the lowest at $0\ \text{ft}$, and the highest at $40\,000\ \text{ft}$, being particularly accurate inside the range defined by those points. With this purpose, the model parameters are defined as $N_s = 314.9$, and $H_b = 7.8516\ \text{km}$. It can be shown that the average refraction parameter is well-approximated by,

$$\bar{k} = \cfrac{1}{1 - \left(\cfrac{10^{-6} \, N_S \, \cos(\theta_{GS \, [\text{rad}]}) \, R_{Earth \, [\text{km}]}}{H_{b \, [\text{km}]}}\right) \left(\cfrac{h_{A,MSL \, [\text{km}]}/H_{b \, [\text{km}]}}{e^{h_{A,MSL \, [\text{km}]}/H_{b \, [\text{km}]}} - 1}\right)} \tag{3.16}$$

where:

- N_s: average surface refractivity,

- H_b: breakpoint parameter of the simplified refractivity model.

It is worth noting that the model depends on the elevation angle at the GS, which, in turn, depends on the refraction parameter. The problem can be solved with some approximation by using the geometric elevation angle at the GS's antenna, that is, the angle given by (3.14) for $\bar{k} = 1$. Nonetheless, an accurate approach would be to iterate between the two quantities until some accuracy metric was met.

Assessing LoS coverage for a target-sensor pair is a computationally expensive task. The link length, or LoS distance, must be computed, and an LoS vector defined, digitised, and compared with the DEM to determine if the point-to-point link, or Fresnel ellipsoid, is cleared. A first order approximation for the coverage area, neglecting terrain shadowing, and considering only the shadowing of a smooth, spherical Earth, should be considered to avoid unnecessary computations for points outside this region. The radius of this circular coverage area is defined as the maximum link length,

$$d_{RH \, [\text{km}]} = \sqrt{r_{A \, [\text{km}]}^2 - R_{e \, [\text{km}]}^2} + \sqrt{r_{GS \, [\text{km}]}^2 - R_{e \, [\text{km}]}^2} \tag{3.17}$$

The radio horizon distance of each antenna defines the maximum propagation distance of the radio link. Coverage computations should include all points of the DEM within this radius. The number of ground points that must be evaluated grows considerably as altitude increases, lengthening computation time. Table 3.1 shows the evolution of the radio horizon distance with antenna height.

Table 3.1 – Radio horizon distance for different antenna heights.

Antenna height above MSL		Radio horizon distance	
$h_{t,MSL}$ [m]	$h_{t,MSL}$ [ft]	d_{RH} [km]	d_{RH} [NM]
305	1000	72	39
1524	5000	161	87
3048	10000	228	123
15240	50000	509	275

In order to establish LoS conditions, one should take into account that a great percentage of radio wave energy is concentrated in the first Fresnel zone [20]. The general equation for the υth Fresnel zones radius evaluation at any point P in between the endpoints of a radio link, is given by,

$$F_{\upsilon,P \, [\text{m}]} = \sqrt{\frac{\upsilon \, \lambda_{0 \, [\text{m}]} \, d_{P,A \, [\text{m}]} \, d_{P,GS \, [\text{m}]}}{d_{P,A \, [\text{m}]} + d_{P,GS \, [\text{m}]}}} \tag{3.18}$$

where:
- $d_{P,A}$: distance of a point P in the radio link to the aircraft,

- $d_{P,GS}$: distance of a point P in the radio link to the GS.

For Mode A/C/S/ES replies, the wavelength is $0.275\,\text{m}$. The Fresnel ellipsoid radius has its maximum for $d_{P,A} = d_{P,GS}$, (3.18) yielding $82.9\,\text{m}$ for $\upsilon = 1$, $d_{P,A} = d_{P,GS} = 50\,\text{km}$ and $\lambda_0 = 0.275\,\text{m}$. In this assessment, and to avoid the slow fading effects resulting from terrain shadowing, only the propagation paths with a completely cleared first degree Fresnel zone are considered viable.

The employed Digital Elevation Model (DEM) is a subset of the Advanced Spaceborne Thermal Emission and Reflection Radiometer Global Digital Elevation Model Version 002 (ASTER GDEM V2), developed jointly by the U.S. National Aeronautics and Space Administration (NASA) and Japan's Ministry of Economy, Trade, and Industry (METI) [58]. The original model was obtained by stereo-correlation of data captured in between years 2000 to 2011 by the ASTER sensor on board of the TERRA satellite, having an overall vertical accuracy of around $17\,\text{m}$ at the 95% confidence level, and a horizontal resolution of approximately $75\,\text{m}$; performance depends on several factors, such as, terrain slope, existence of tree canopies, or consistent presence of clouds over the same area during the several satellite scans.

The ASTER GDEM V2 is available for download, free of charge, from the Land Processes Distributed Active Archive Centre (LP DAAC) Global Data Explorer (GDEx) website [59]. The model is distributed as Geographic Tagged Image File Format (GeoTIFF) files with geographic coordinates (latitude, longitude). The data consists of a $1\,\text{arcsecond}$ (approximately $30\,\text{m}$ at the equator) grid cell DEM, referenced to the 1984 World Geodetic System (WGS84) / 1996 Earth Gravitational Model (EGM96) geoid.

The average geoid undulation in Portugal is $50\,\text{m}$, this value being used when converting between the height above mean sea level, h_{MSL}, and the one above the ellipsoid, h_{HAE}, which can be related through,

$$h_{MSL}(\phi, \lambda) = h_{HAE}(\phi, \lambda) + \Delta h_{geoid}(\phi, \lambda) \tag{3.19}$$

where:
- Δh_{geoid}: geoid undulation with respect to the ellipsoid,
- ϕ: geodetic latitude,
- λ: geodetic longitude.

The terrain profile bellow the link path can be extracted by bilinear interpolation of the DEM matrix; with this purpose, the locations along the great circle arc connecting a GS and an aircraft should be defined. Taking the Spherical Earth Model and the spherical trigonometry laws, it is possible to estimate the latitude and the longitude coordinates of an arbitrary point along the arc of the great circle between two points [55]. Adjusting the estimator to account for a sampling resolution yields,

$$\phi_{A/GS,t\,[\text{rad}]} = \arcsin\left(\sin\left(\phi_{GS\,[\text{rad}]}\right)\cos\left(t\,\Delta\theta_{c\,[\text{rad}]}\right) + \cos\left(\phi_{GS\,[\text{rad}]}\right)\sin\left(t\,\Delta\theta_{c\,[\text{rad}]}\right)\cos\left(\psi_{A/GS\,[\text{rad}]}\right)\right) \tag{3.20}$$

$$\lambda_{A/GS,t\,[\text{rad}]} = \lambda_{GS\,[\text{rad}]} + \arctan\left(\sin\left(\psi_{A/GS\,[\text{rad}]}\right)\sin\left(t\,\Delta\theta_{c\,[\text{rad}]}\right),\right.$$
$$\left.\cos\left(\phi_{GS\,[\text{rad}]}\right)\cos\left(t\,\Delta\theta_{c\,[\text{rad}]}\right) - \sin\left(\phi_{GS\,[\text{rad}]}\right)\sin\left(t\,\Delta\theta_{c\,[\text{rad}]}\right)\cos\left(\psi_{A/GS\,[\text{rad}]}\right)\right) \tag{3.21}$$

$$t \in \left\{t : t \in \mathbb{N}, t \in [1, N_t], N_t = \left\lfloor \frac{\theta_c}{\Delta\theta_c} \right\rfloor\right\} \tag{3.22}$$

$$\Delta\theta_{c\ [\text{rad}]} = \frac{\Delta d_{DEM\ [\text{km}]}}{R_{Earth\ [\text{km}]}} \tag{3.23}$$

$$\psi_{A/GS\ [\text{rad}]} = \arctan\big(\cos(\phi_{A\ [\text{rad}]})\sin(\lambda_{A\ [\text{rad}]} - \lambda_{GS\ [\text{rad}]})\ ,$$
$$\sin(\phi_{A\ [\text{rad}]})\cos(\phi_{GS\ [\text{rad}]}) - \cos(\phi_{A\ [\text{rad}]})\sin(\phi_{GS\ [\text{rad}]})\cos(\lambda_{A\ [\text{rad}]} - \lambda_{GS\ [\text{rad}]})\big) \tag{3.24}$$

where:

- $\phi_{A/GS,t}$: t^{th} geodetic latitude sample along a great circle arc,
- $\lambda_{A/GS,t}$: t^{th} geodetic longitude sample along a great circle arc,
- $\Delta\theta_c$: sampling resolution of the geocentric angle,
- Δd_{DEM}: sampling resolution of the terrain profile,
- $\psi_{A/GS}$: azimuth of the great circle arc at the aircraft location,
- $\arctan\ (\ ,\ )$: four-quadrant inverse tangent.

This model depends on 5 input parameters: GS coordinates, aircraft coordinates, and sampling resolution of the terrain profile. The last parameter should be selected considering the DEM resolution, and the processing time. It is worth noting that in (3.21) since two quantities in the range $[-\pi, \pi]$ are being added, the result will be in the range $[-2\pi, 2\pi]$, therefore, an adjustment of $\pm 2\pi$ may be required to guarantee a value for $\lambda_{A/GS,t}$ in the range $[-\pi, \pi]$.

3.1.3 Error model

A telecommunications system's coverage is a complex concept that may depend on a number of factors, such as the received signal strength, delay between the edge of the network and its core, or capacity in terms of users and bitrate. In the case of aeronautical multilateration, coverage should also be defined in terms of aircraft location accuracy.

Considering a TDoA estimator based on ToA correlation, the RMS TDoA estimation accuracy associated with the GSs pair (GS_1, GS_2) can be modelled by a Root Sum of Squares (RSS) of the RMS ToA accuracy of each pair of sensors,

$$\Delta d_{TDoA\ (GS_1, GS_2)\ [\text{m}]} = \sqrt{\Delta d_{TOA\ GS_1\ [\text{m}^2]}^2 + \Delta d_{TOA\ GS_2\ [\text{m}^2]}^2} \tag{3.25}$$

where:

- $\Delta d_{ToA\ GS_k}$: RMS ToA accuracy associated with the kth GS.

Considering the several error components, the RMS ToA accuracy can be modelled by the RSS,

$$\Delta d_{TOA\ [\text{m}]} = \sqrt{\Delta d_{SNR\ [\text{m}^2]}^2 + \Delta d_{sampling\ [\text{m}^2]}^2 + \Delta d_{quantisation\ [\text{m}^2]}^2 + \Delta d_{jitter\ [\text{m}^2]}^2 + \Delta d_{sync\ [\text{m}^2]}^2} \tag{3.26}$$

where:

- Δd_{SNR}: error component due to pulse detection,
- $\Delta d_{sampling}$: error component due to sampling timing,
- $\Delta d_{quantisation}$: error component due to pulse quantisation,

- Δd_{jitter}: error component due to local clock jitter,
- Δd_{sync}: error component due to system synchronisation.

The effect of the additive white Gaussian noise at the matched filter detector is modelled by [60], [61],

$$\Delta d_{SNR\,[m]} = \frac{c_{[m/s]}}{2\sqrt{2}\,\pi\,B_{w\,[Hz]}\sqrt{E_{b\,[J/bit]}/N_{0\,[W/Hz]}}}$$

(3.27)

where:
- c: light speed in vacuum,
- B_w: effective bandwidth of the preamble pulses,
- E_b: signal energy per bit,
- N_0: noise power density per Hertz of noise bandwidth.

Figure 3.2 depicts the behaviour of (3.27) for an effective bandwidth of $2\,\mathrm{MHz}$. In these conditions, the RMS ToA accuracy is inversely proportional to the SNR with a proportionality constant of $284.6\,\mathrm{m}^2$, while Figure 3.3 depicts the combined behaviour of (3.27) and (3.25) for an effective bandwidth of $2\,\mathrm{MHz}$.
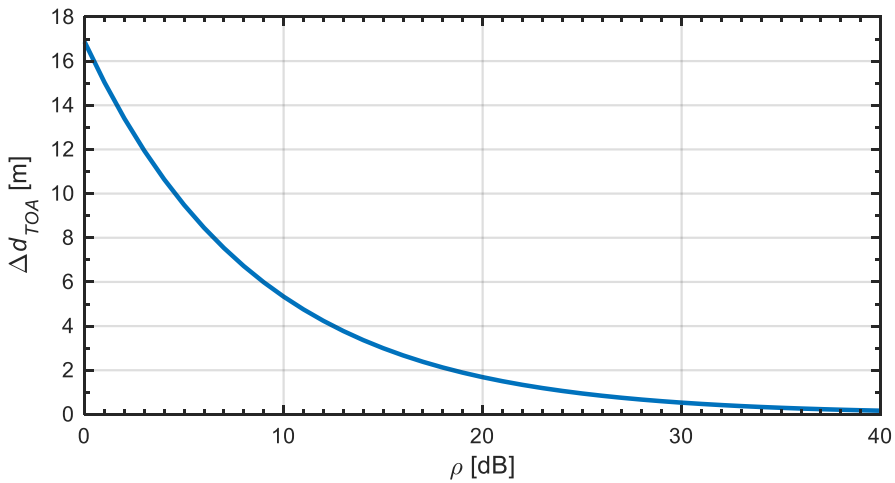
Figure 3.2 – RMS ToA accuracy versus the effective SNR, with $B_w = 2\,\mathrm{MHz}$.
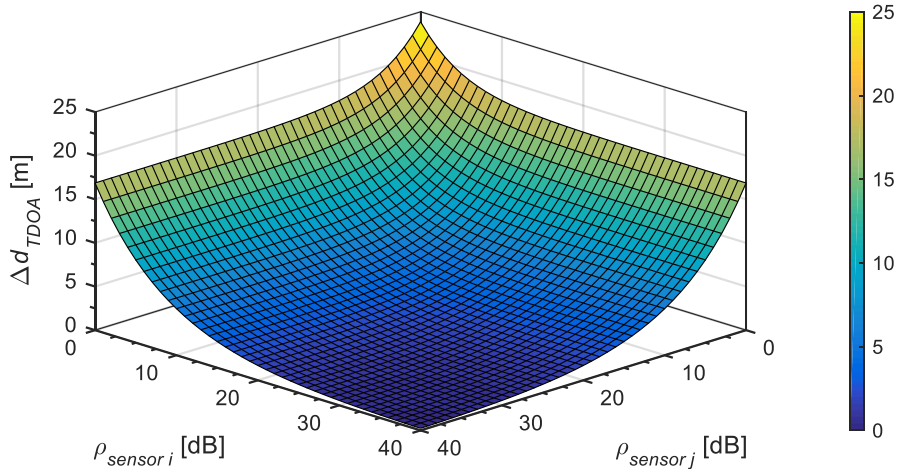
Figure 3.3 – RMS TDoA accuracy versus the effective SNR in each sensor, with $B_w = 2\,\mathrm{MHz}$.

The effect of the additive white Gaussian noise at the sampling time instant, is modelled as an error component by [62],

$$\Delta d_{sampling\,[m]} = c_{[m/s]}\,\frac{\Delta t_{sampling\,[s]}}{\sqrt{12}}$$

(3.28)

where:

- $\Delta t_{sampling}$: sampling interval.

The model assumes an optimal receiver and only measures the error component due to thermal noise, corrupting the receiver's ability to read the correct pulse ToA. One should complete the model with other error components, namely, the timing errors (typically $15\,\mathrm{m}$) and the propagation errors (typically $23\,\mathrm{m}$). As seen in Table 3.2, the RMS ToA accuracy for each sensor is given by the RSS of several error components.

Table 3.2 – Error components of the RMS ToA accuracy (extracted from [32]).

Error source	Typical RMS value	Reference
Timing	15 m	Leeson [63]
Propagation	23 m	Leeson [63]
Sensor survey	5 m	Leeson [63]
Multipath	Unknown	Leeson [63]
AWGN	Analytically determined	McDonough et al. [64]

The design matrix, $\mathbf{D}$, $[3 \times N_{GS}]$, holding the aircraft-sensor geometry, has columns containing the LoS unit vectors between the aircraft and each GS [42], [55],

$$\mathbf{D}_{[3\times N_{GS}]} = \begin{bmatrix} \rho_{1\,x} & & \rho_{N_{GS}\,x} \\ \rho_{1\,y} & \cdots & \rho_{N_{GS}\,y} \\ \rho_{1\,z} & & \rho_{N_{GS}\,z} \end{bmatrix}$$

(3.29)

$$\boldsymbol{\rho}_{k\,[3\times1]} = \frac{\mathbf{x}_{[3\times1]} - \mathbf{x}^k_{[3\times1]}}{\left\| \mathbf{x}_{[3\times1]} - \mathbf{x}^k_{[3\times1]} \right\|}$$

where:

- $\boldsymbol{\rho}_k$: aircraft LoS unit vector associated with the kth ground station,
- N_{GS}: number of ground stations,
- $\mathbf{x}$: aircraft ECEF coordinates,
- $\mathbf{x}^k$: k^{th} ground station ECEF coordinates.

GDoP is a dimensionless quantity defined by the Frobenius norm [65],

$$D_{GDOP} = \sqrt{\mathrm{tr}\left(\mathbf{D}_{[3\times N_{GS}]}\,\mathbf{D}^{\mathrm{T}}_{[N_{GS}\times3]} \right)}$$

(3.30)

where:

- $\mathrm{tr}\,(\cdot)$: trace of a square matrix.

The RMS position accuracy, i.e., the covariance matrix of the aircraft ECEF positioning estimates, is defined as,

$$\mathbf{\Sigma}_{ecef\ [3\times3][\text{m}^2]} = \mathbf{D}_{[3\times N_{GS}]}\ \mathbf{\Sigma}_{tdoa\ [N_{GS}\times N_{GS}][\text{m}^2]}\ \mathbf{D}^{\text{T}}_{[N_{GS}\times3]} \tag{3.31}$$

where:

- $\mathbf{\Sigma}_{tdoa}$: covariance matrix of the TDoA estimates.

Under LoS conditions the measurement errors can be considered zero-mean, independent, and identically distributed Gaussian variables [66]; as a result, the covariance matrix is expressed as,

$$\mathbf{\Sigma}_{tdoa\ [N_{GS}\times N_{GS}][\text{m}^2]} = \begin{bmatrix} \Delta d^2_{TDoA\ (GS_1,GS_2)\ [\text{m}]} \\ \vdots \\ \Delta d^2_{TDoA\ \left(GS_1,GS_{N_{GS}}\right)\ [\text{m}]} \end{bmatrix} \mathbf{I}_{[N_{GS}\times N_{GS}]} \tag{3.32}$$

where:
- $\mathbf{I}$: identity matrix.

The transformation matrix from ECEF to East-North-Up (ENU) coordinates [55], is

$$\mathbf{T}^{ecef}_{enu\ [3\times3]} = \begin{bmatrix} -\sin\lambda & \cos\lambda & 0 \\ -\sin\phi\cos\lambda & -\sin\phi\sin\lambda & \cos\phi \\ \cos\phi\cos\lambda & \cos\phi\sin\lambda & \sin\phi \end{bmatrix} \tag{3.33}$$

Applying the transformation matrix, the error matrix of the aircraft ENU positioning estimates becomes,

$$\mathbf{\Sigma}_{enu\ [3\times3][\text{m}^2]} = \mathbf{T}^{ecef}_{enu\ [3\times3]}\ \mathbf{\Sigma}_{ecef\ [3\times3][\text{m}^2]}\ \mathbf{T}^{ecef\ \text{T}}_{enu\ [3\times3]} \tag{3.34}$$

When estimating the aircraft's position, the aeronautical service provider relies on the altitude transmitted by the on-board altimeter via ADS-B; therefore, only the East and North terms of the error matrix should be considered for the accuracy analysis of the aeronautical multilateration system. In this scenario, the RMS positioning error becomes,

$$\Delta d_{pos\ [\text{m}]} = \sqrt{\Delta d^2_{ee\ [\text{m}^2]} + \Delta d^2_{nn\ [\text{m}^2]}} \tag{3.35}$$

where:
- Δd^2_{ee}: variance of the aircraft positioning estimates in the East direction,
- Δd^2_{nn}: variance of the aircraft positioning estimates in the North direction.

3.2 Model implementation

The models presented in Section 3.1 were implemented in a simulator using the matrix-based MathWorks MATLAB r2016a language. Implementation was done considering MathWorks recommendations for improvement of performance [67], and efficient use of memory [68].

3.2.1 Simulator overview

The developed algorithm uses a DEM to determine if an aircraft and a GS are in LoS; subsequently, the received power is computed considering the transmitted power, the radiation pattern of the antenna placed on the aircraft, the path loss, and the radiation pattern of the antenna in the GS. The CNR is estimated, being used to evaluate if the target's message is detected and correctly decoded by the GS's receiver. Finally, having performed the radio coverage analysis, GDoP and the RMS position accuracy models are applied to access the system performance.

As seen in Figure 3.4, the first step of the simulator concerns the input data loading and processing; next, the object used to organise the input, output and inner parameters of the simulator is initialised and populated. The simulator was optimised for an analysis across FLs, independently analysing the system coverage for each FL. The main simulator loop starts by running the PrM Simulator to estimate radio coverage, then, considering these results, system accuracy is estimated in the ErM Simulator.
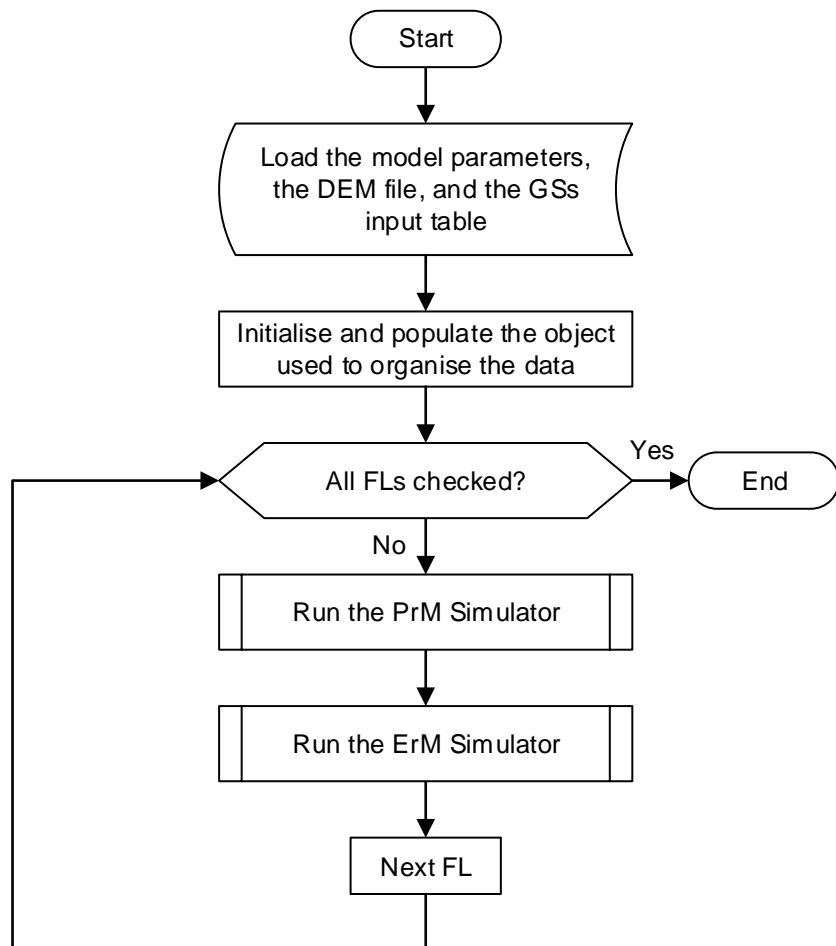
Figure 3.4 – Simulator overview.

The simulation process begins by loading variables and predefined parameters: the DEM with the terrain elevation profile matrix; the GSs file with the array of GSs geodetic coordinates; the Aircraft file with the array of aircraft geodetic coordinates; the radiation patterns of the GSs' and aircraft antennas, which may be a mapping array or a nonparametric regression function; and, the aeronautical scenario basic parameters, such as the preamble pulses bandwidth, transmitted power, channel bandwidth, noise

figure, fading margins, and losses in the receiver system.

3.2.2 Propagation model simulator

Figure 3.5 shows the overview of the PrM Simulator, the simulator consists of three main functions: the radio-horizon algorithm, the LoS algorithm, and the CNR estimation algorithm.
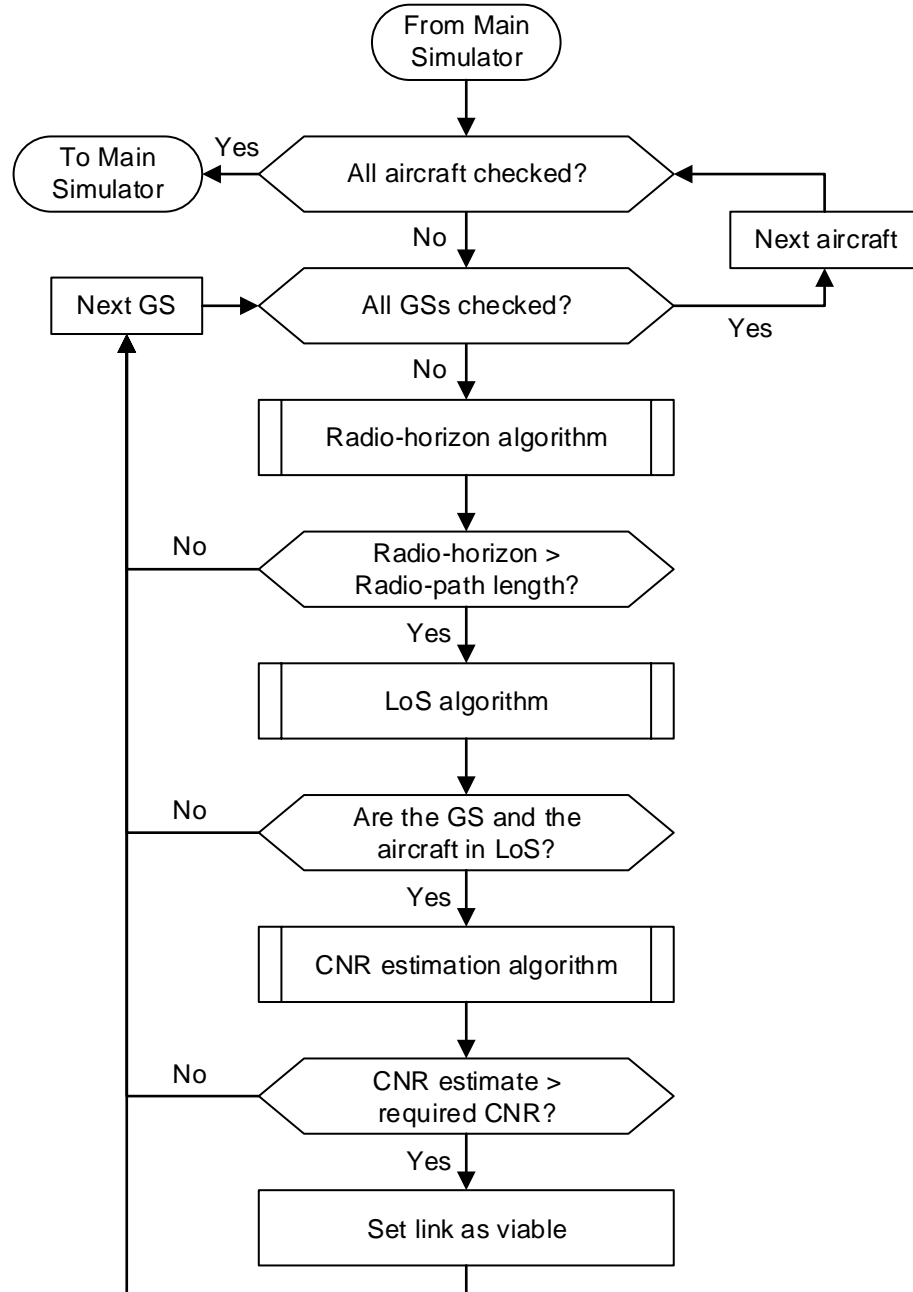
Figure 3.5 – Flowchart of the PrM simulator with the steps required to estimate radio coverage.

The process is implemented in a nested loop, estimating radio coverage for each link between an aircraft and a GS. First the radio-horizon distance is compared with the radio-path length, allowing the swift rejection of NLoS links beyond the radio-horizon, and avoiding further unnecessary computations; then, if the aircraft is not beyond the radio-horizon, the LoS algorithm is employed, assessing radio visibility

in terms of terrain shadowing. Finally, only for LoS links, the CNR estimation algorithm is used to verify if the estimated CNR is above the required one, suggesting that the QoS specifications for message detection in the receiver are met. Only links that pass the above steps are marked as viable, this information is critical for the ErM Simulator.

Figure 3.6 depicts the flowchart for the radio-horizon algorithm with the steps required to determine if an aircraft is beyond the radio-horizon; it is worth recalling that the geometric polar angle at the GS's antenna is obtained by applying (3.14) for $\bar{k} = 1$.
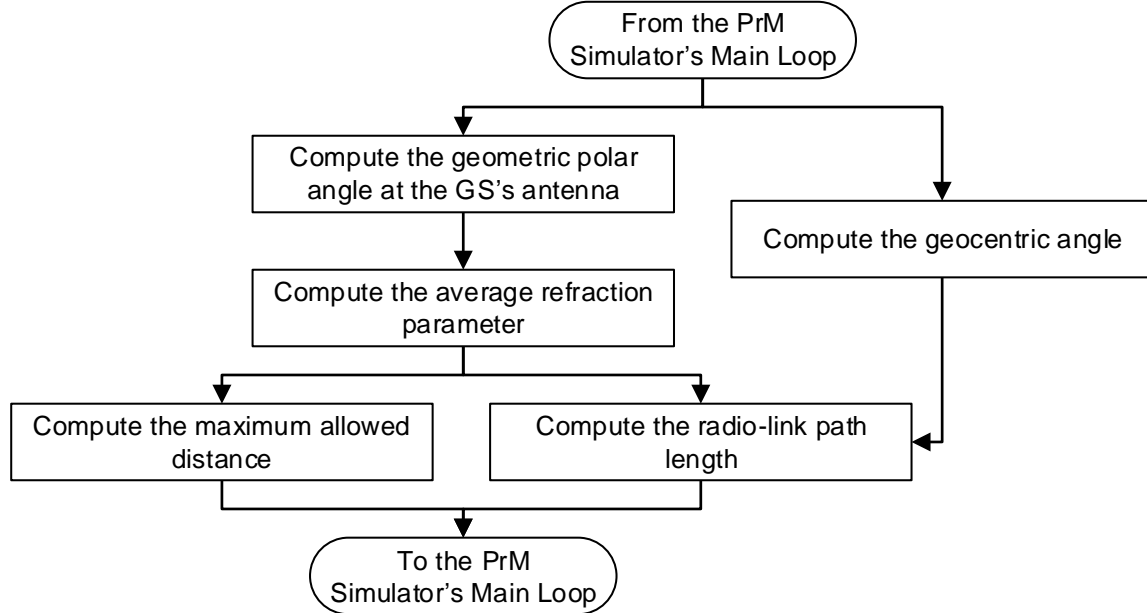
Figure 3.6 – Flowchart for the radio-horizon algorithm with the steps required to compute the average refraction parameter and the radio-link path length.

As seen in Figure 3.7, the LoS coverage analysis starts with the digitalisation of the great circle arc between the aircraft and the GS; then, with this information, the terrain profile is extracted from the DEM matrix by bilinear interpolation. The heights are then corrected to account for the effective Earth bulge, and each point of the Fresnel ellipsoid is compared with the terrain profile below, determining if the Fresnel ellipsoid is cleared. The radius of the Fresnel ellipsoid is obtained for each point of the link, and by subtracting each point of the slant-range with the corresponding ellipsoid radius, one obtains the maximum elevation that the terrain-plus-obstacles can have.

Figure 3.8 shows the CNR estimation algorithm, the algorithm takes the slant-range distance, the elevation angle at the GS site, and the depression angle at the aircraft. These parameters are fed to the propagation model and the power at the receiver is obtained.

The ErM simulator is depicted in Figure 3.9, the simulator takes each aircraft at a time; and, considering the list of viable GSs per aircraft learned by the PrM simulator, the accuracy associated with the given aircraft coordinate is assessed. First, the ToA error components associated to each GS are computed; then, the independent TDoA combinations are determined using MATLAB's $nchoosek$ command. Having defined the pairs of GSs used to write the TDoA system of equations, the RMS positioning error associated to the given aircraft coordinate is computed.
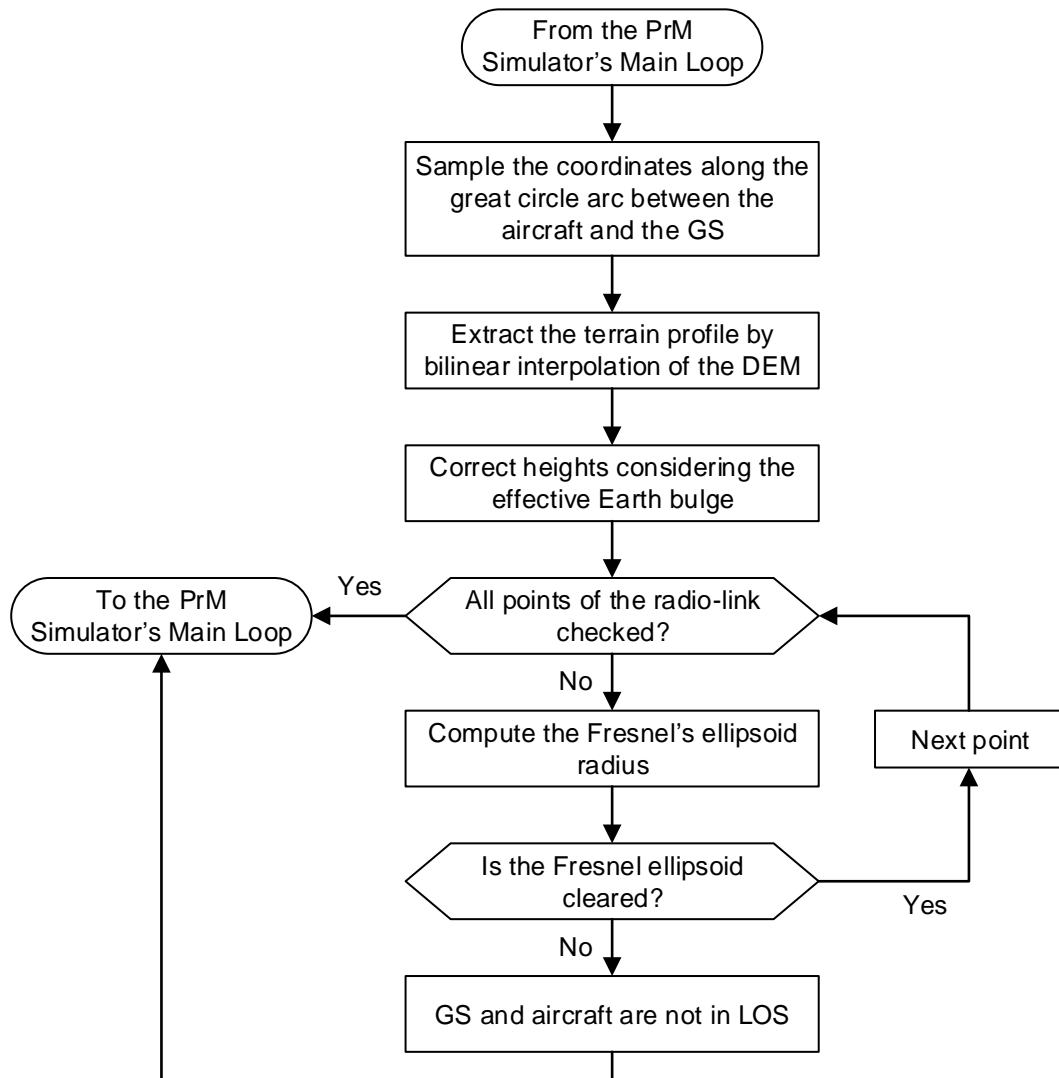
Figure 3.7 – Flowchart for the LoS algorithm.
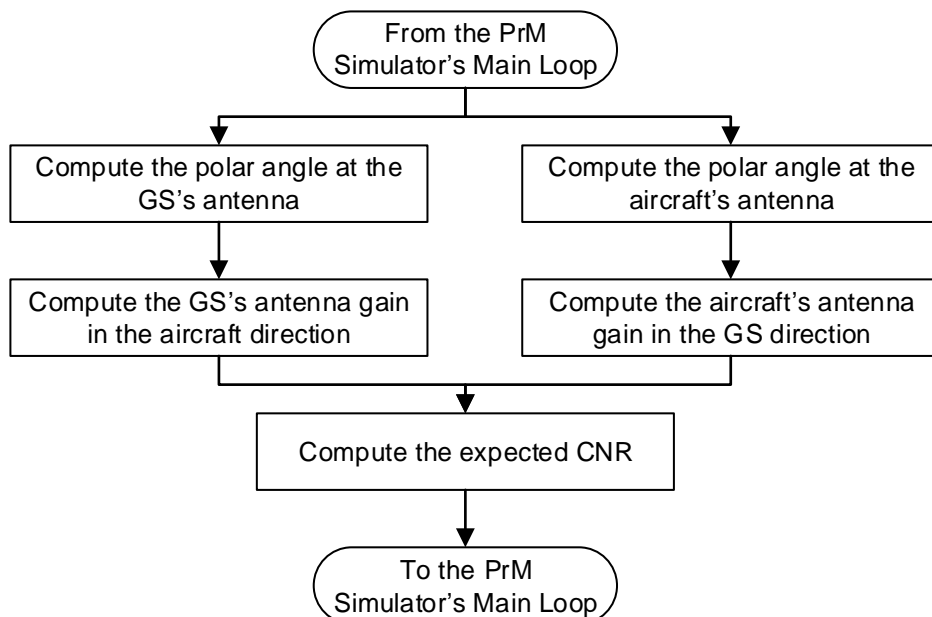
Figure 3.8 – Flowchart for the CNR estimation algorithm.

3.2.3 Error model simulator

The ErM simulator is depicted in Figure 3.9, which takes each aircraft at a time, and considering the list of viable GSs per aircraft learned by the PrM simulator, assesses the accuracy associated with the given aircraft coordinate. First, the ToA error components associated to each GS are computed, then, the independent TDoA combinations are determined using MATLAB's $nchoosek$ command. Having defined the pairs of GSs used to write the TDoA system of equations, the RMS positioning error associated to the given aircraft coordinate is computed.
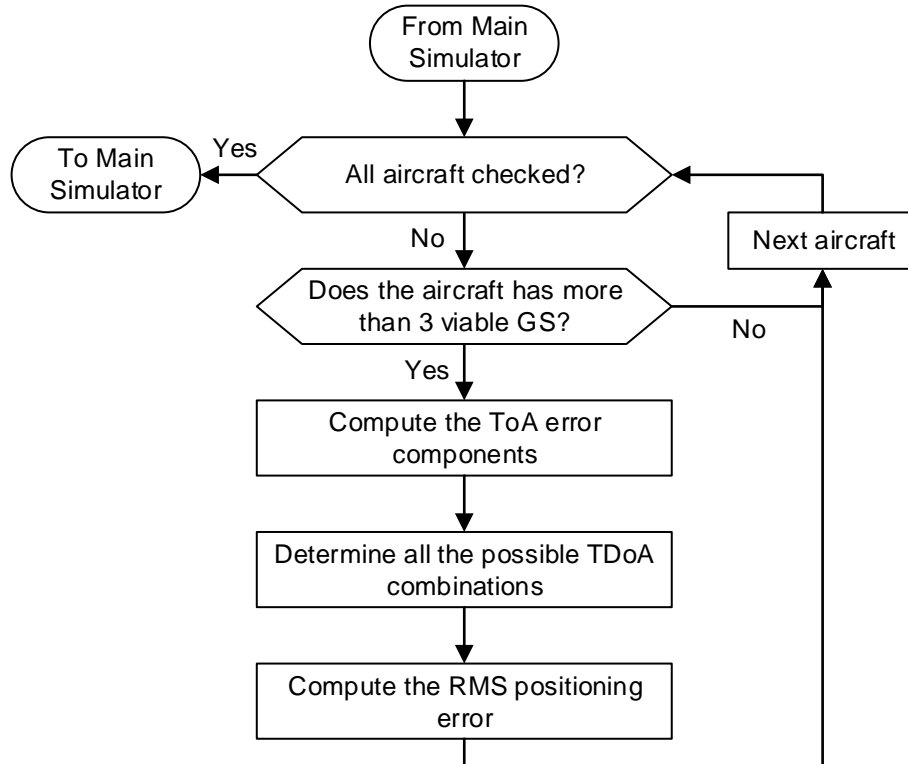
Figure 3.9 – Flowchart of the ErM simulator.

3.2.4 Estimating the required carrier-to-noise ratio

The minimum CNR required at the receiver for correct demodulation of a message is an important parameter when estimating system coverage. In digital modulation systems, the required CNR is directly proportional to the Bit-Energy-to-Noise-Density Ratio, simply referred to as SNR, required by the demodulator to ensure that the bit error probability, or Bit Error Rate (BER), of the system remains below a specified threshold; with the proportionality constant being the ratio between the data bit rate and the channel bandwidth. In decibels, this relationship is expressed by,

$$(P_{Rx}/N)_{min \text{ [dB]}} = (E_b/N_0)_{min \text{ [dB]}} + 10 \log \frac{R_{b \text{ [bit/s]}}}{\Delta f_{rc \text{ [Hz]}}} \tag{3.36}$$

where:
- R_b: data bit rate at the baseband output,
- $(E_b/N_0)_{min}$: required SNR.

The required SNR to ensure a given bit error probability QoS, increases with the modulation scheme complexity, and decreases with the implementation of error correction techniques; therefore, the correct estimation of this parameter requires the knowledge on the digital modulation scheme used, and on the error correction capability of the system. In aeronautical multilateration systems the modulation scheme differs in the up- and downlinks; in what follows, one establishes the relationship between the required SNR for a specified BER in the two-way communication channel.

Binary Differential Phase Shift Keying (2-DPSK), is the modulation scheme used for uplink interrogation messages. Assuming an optimal differential demodulator at the aircraft's receiver, the required SNR for a specified BER can be estimated from [69],

$$(E_b/N_0)_{min,UL \, [\text{dB}]} = 10 \log(-\ln(2 \, P_{e \, UL})) + M_{I \, [\text{dB}]} \tag{3.37}$$

where:
- $P_{e \, UL}$: uplink bit error probability specification,
- M_I: implementation margin.

Binary Pulse Position Modulation (2-PPM), is the modulation scheme used for the downlink replies transmitted by the aircraft's transponder. Assuming a coherent demodulator at the GS's receiver, the required SNR for a specified BER can be estimated from [70],

$$(E_b/N_0)_{min,DL \, [\text{dB}]} = 10 \log(Q^{-1}(P_{e \, DL})^2) + M_{I \, [\text{dB}]} \tag{3.38}$$

where:
- $P_{e \, DL}$: downlink bit error probability specification,
- Q^{-1}: inverse Gaussian Q-function.

The bit error probability requirement is not directly specified for aeronautical multilateration systems; instead, this parameter should be computed from the probability of detection requirement, specified by EUROCONTROL as 97%, defined as the product of two components: the probability of an aircraft detecting the uplink interrogation message, and the probability of a GS detecting the aircraft's downlink reply. Since the combination of these two effects would greatly increase the problem complexity, they are considered independent, and defined as equal to $\sqrt{97\%} = 98.49\%$. Moreover, the probability of detecting a message is assumed to be equal to the complementary of the block error probability.

In a system with Forward Error Correction (FEC), capable of correcting up to N_c errors, the block error probability is defined as,

$$P_{e \, N_c \, N_{bl}} = 1 - \sum_{N_b=0}^{N_b=N_c} P_{e \, N_b \, N_{bl}} \tag{3.39}$$

where:
- N_c: maximum number of errors allowed for a correct demodulation,
- N_{bl}: message bit-length,
- N_b: number of errored bits in the message,
- $P_{e \, N_b \, N_{bl}}$: probability of having exactly N_b errored bits in an N_{bl} bit block.

The probability of having N_b errored bits in a message bit block of size N_{bl} can be related with the bit error probability by the following expression,

$$P_{e\,N_b\,N_{bl}} = \frac{N_{bl}!}{(N_{bl} - N_b)!\,N_b!}P_e^{N_b}(1 - P_e)^{N_{bl}-N_b}$$

(3.40)

where:
- P_e: bit error probability.

For both up- and downlink messages, the length of the bit block is $N_{bl} = 112$ bit. In the uplink, only error detection is attempted, and $N_{c,UL} = 0$; conversely, error correction is implemented in the downlink, with $N_{c,DL} = 1$ [71]. Table 3.3 describes the budget to estimate the required CNR of the aeronautical multilateration system.

Table 3.3 – Budget for the estimation of the required CNR.

Parameter	Uplink	Downlink	Comment
Modulation scheme	2-DPSK	2-PPM	See [72]
Probability of detection	98.49 %	98.49 %	
Error correction	0 bit	1 bit	See [71] and [72]
Message bit length	112 bit	112 bit	See [72]
Implementation margin	2.0 dB	2.0 dB	
Data bit rate	4 Mbps	1 Mbps	See [72]
Noise bandwidth	2 MHz	2 MHz	
Required CNR	14.5 dB	8.4 dB	Equation (3.36)
Noise factor	5.0 dB	5.0 dB	See [73] and [74]
Total noise power	−106.0 dBm	−106.0 dBm	Equation (3.7)
Receiver sensitivity	−91.5 dBm	−97.6 dBm	Equation (3.41)

The receiver sensitivity, or Minimum Triggering Level (MTL), is expressed by,

$$P_{Rx\,min\,[dBm]} = N_{[dBm]} + (P_{Rx}/N)_{required\,[dB]}$$

(3.41)

3.2.5 Radiation pattern of the ground stations' antenna

The type of antenna used for the GSs affects system coverage, accuracy, and multipath rejection [11]. Ground Stations owned by NAV use an omnidirectional, 10-element, collinear dipole phased array specifically designed for ATC, minimising multipath, and the radiated cone of silence [75]. The Cartesian plot of the antenna's far-field vertical radiation pattern is available from the manufacturer website in JPEG format, Figure 3.10 is the result of extracting the pixel positions corresponding to the pattern plot and applying a coordinate transformation from the JPEG coordinate system to the elevation pattern one: the elevation plane pattern displays some degree of loss in the ground direction, rejecting multipath from ground reflections, and favouring links with a polar angle in the range $[45º, 95º]$. The maximum gain occurs for a polar angle of $84º$, suggesting that the antenna was optimised to favour links close to the radio horizon where attenuation is more intense.
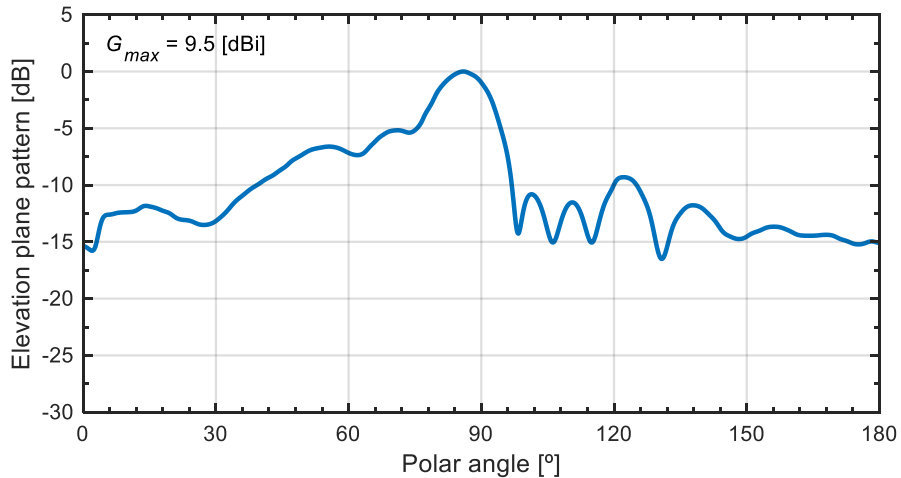
Figure 3.10 – Elevation plane pattern for the ground stations (extracted from [75]).

3.2.6 Statistical modelling of an antenna mounted on an aircraft

The PrM model should be robust concerning the aircraft's design and spatial orientation; for this reason, the model for the shadowing due to the aircraft's structure should comprise some level of generalisation. There was then the need to have the statistical modelling of the aircraft structure's influence on the radiation pattern of the ATC transponder antenna. Obtaining an unbiased estimate for this effect is out of the scope of this thesis, and was not found in the literature; instead, a model for the most common aircraft, the Airbus A320, with an antenna mounted on the bottom of the fuselage, forward to the wings, is proposed. Robustness in terms of aircraft orientation is attained by only considering the average far field elevation pattern plus a slow fading margin. A fully characterisation of the airframe shadowing, concerning the duration and depth of the fading events, or the best-fit statistical distribution, is also avoided, but should be considered in a more thorough and comprehensive study.

ICAOs Annex 10 [17] recommends that the transponder antenna system installed on an aircraft should have a radiation pattern nominally equivalent to that of a quarter-wave monopole on a ground plane. Comparatively to antennas in free space or above a standard ground plane, antennas installed on aerostructures display distorted radiation patterns due to reflection, refraction and dispersion effects caused by the fuselage, wings, moving rotors and other structures of the aircraft. Consequently, the same antenna displays different radiation patterns across different aircraft or different positions on the same aircraft [76], [77].

Commercial aviation aircraft have two independent transponder systems, each with two dedicated antennas, one on top and another on the bottom of the fuselage, performing a total of four antennas. Figure 3.11 shows the antennas locations for a typical commercial aircraft, the two antennas on top and on the bottom of the fuselage display a considerable angular displacement between each other, suggesting that a diversity combining scheme should provide some level of gain.

The antennas are usually mounted near the front of the fuselage to provide omnidirectional coverage of the aircraft's upper and lower airspace. Typically, the antennas are either planar or wire monopoles

encapsulated on a blade shaped dielectric to provide protection and minimise aerodynamic drag. For this assessment, one assumes a wire monopole mounted on the lower fuselage, forward of the wings.
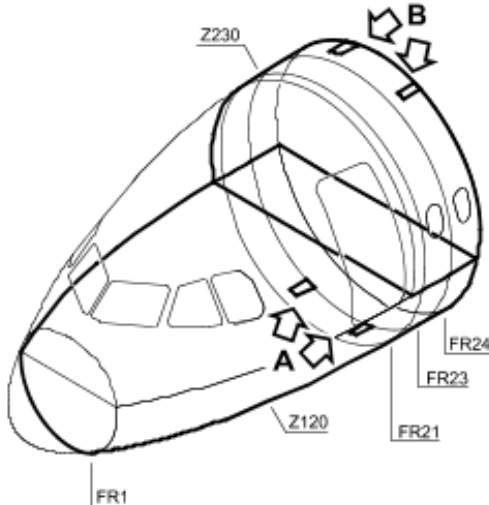
Figure 3.11 – Aircraft's fuselage transversal cut showing transponder antennas locations.

One can expect a radiation pattern resembling a quarter wavelength monopole on an infinite ground plane, crippled by interactions between direct, reflected, diffracted and creeping waves. The number of constructive and destructive wave interactions increases with frequency or structure electrical size, and manifests by ripples in the radiation pattern. Antenna design can be performed using Antenna Magus [78]. One can combine a pre-processed antenna with a simplified CAD model of an aircraft by exporting Antenna Magus's results to CST Microwave Studio [79], and simulate the effects of the airframe on the far-field radiation pattern. Additionally, electrically large problems, such as antenna placement on an aircraft for frequencies around or above $1\,\text{GHz}$, usually require the use of asymptotic methods such as Physical Optics - Shooting and Bouncing Ray (PO-SBR) to simulate the effects of the surrounding structures with a bearable trade-off between computational cost and accuracy [76].

Figure 3.12 displays the general framework to simulate antenna placement on an aerostructure, this framework is based on [76].
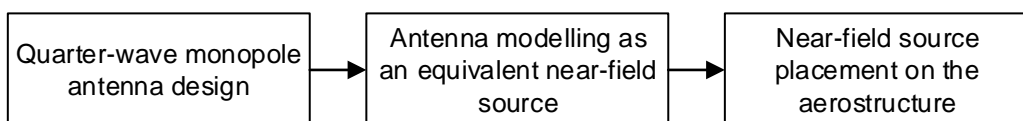
Figure 3.12 – General framework for antenna placement on an aircraft.

One starts by designing a quarter wavelength wire monopole in Antenna Magus, the antenna simulation model is then exported to CST Microwave Studio where the near-field monitor is used to model the antenna as an equivalent near-field source with the help of the Time Domain Solver. The equivalent near-field source is then exported to a new project in CST Microwave Studio; there, the source is placed on the CAD model of an aerostructure, which is assumed to be a large-scale coated Perfectly Electrically Conducting (PEC) object. Using the Asymptotic Solver for the CST simulation, one obtains the far-field results, which are then exported to MATLAB. The results agree with previous measurements existing in the literature for scaled models of small aircraft [80].

Figure 3.13 presents a perspective view of the simulation scenario with the aircraft's airframe and the computed far-field for 1 060 MHz. Results for this frequency are in the midrange between the receiving and transmitting frequencies of the transponder; respectively, 1 030 MHz and 1 090 MHz.
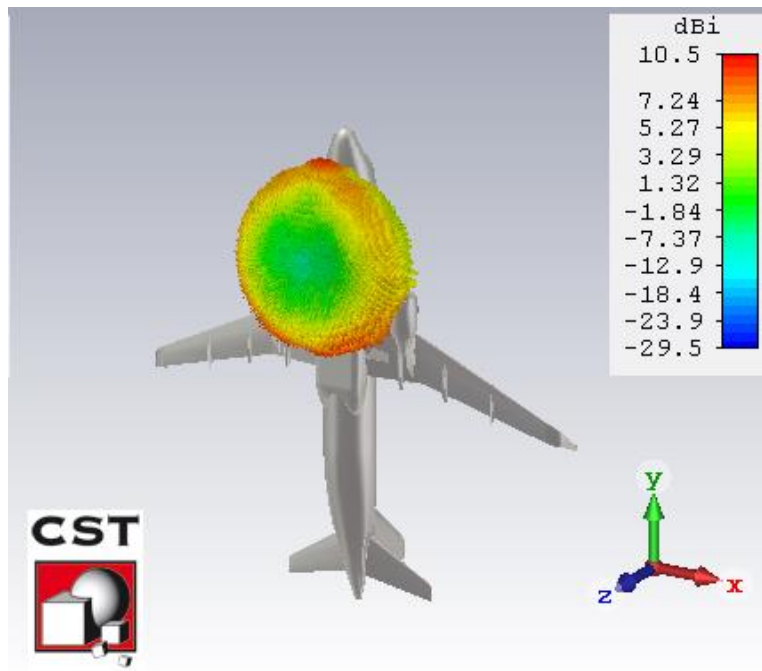
Figure 3.13 – Perspective view of the simulation results, the antenna near-field equivalent source was placed on the bottom of the fuselage, ahead of the wings, 9.3 m from the nose.

Figure 3.14 presents the average absolute gain for the vertical angle, obtained by averaging the 3D far-field pattern simulation results along the horizontal angle for each position of the vertical one. The dataset displays an average standard deviation of 2.25 dBi.
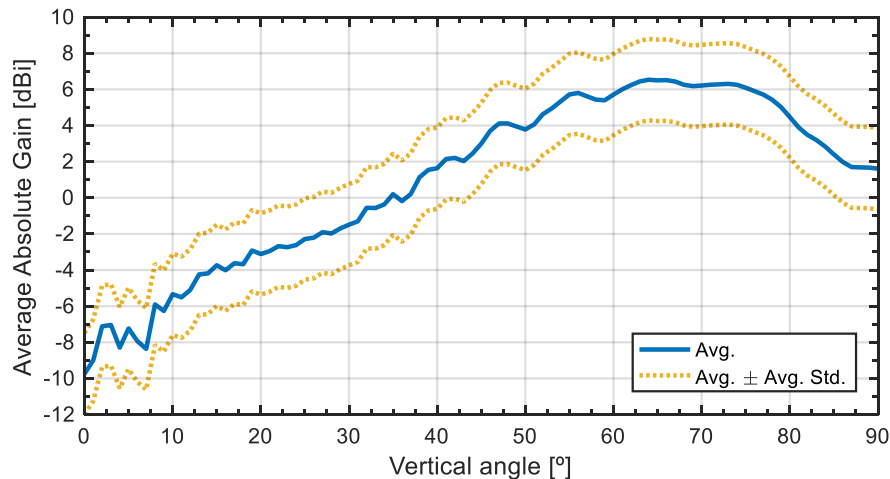
Figure 3.14 – Average absolute transponder antenna gain, with 2.25 dBi average standard deviation.

A laptop with an Intel Core i7 2630QM CPU @ 2.00GHz and 8 GB RAM was used in the simulations, the antenna placement simulation had a computational cost of 2h 59 and 1.9 GB of RAM (peak value).

A statistical analysis of the results could be used to determine and fit the statistical distribution that best

explains the gain oscillations, and define the fading margins due to the uncertainty of the aircraft orientation; however, this analysis is out of the scope of this thesis. Instead, the fading due to the uncertainty of the aircraft orientation is obtained from the literature. In this thesis, since a model for average gain of an antenna mounted on an aircraft is used, the minimum value of $2.6\,\text{dB}$, obtained in [46], is considered for the slow fading margin due to the uncertainty of the aircraft orientation.

3.3 Statistical modelling of positioning error

This section is mostly based on [81] and [82], and deals with the goodness-of-fit tests and statistics that are used to summarise the results, and in statistical and inferential modelling. Technical and management decision-making benefit from the use of computer simulations of real-world systems, through the application of analytical models that describe separate system aspects. The modelling of the different system components often consists of the search for the model that displays the best ratio between simplicity and generalisation. Goodness-of-Fit (GOF) metrics quantify the discrepancy between the theoretical model and the empirical data, and are used as tools for model validation and assessment.

3.3.1 Descriptive statistics

The sample percentile is usually estimated by linear interpolation of the empirical CDF. It provides information on the spread of the data, and the percentage of results bellow a given threshold,

$$\Delta d_{pos}^{p\%} := \left\{ \Delta d_{pos}^{p\%} : \ Prob\big[\Delta d_{pos} \leq \Delta d_{pos}^{p\%}\big] = p\% \right\} \tag{3.42}$$

The sample mean of the positioning error is a measure of location, providing insight into the central tendency of the observations,

$$\overline{\Delta d_{pos}(h_{MSL})} = \frac{1}{N_\phi N_\lambda} \sum_{n=1}^{N_\phi} \sum_{m=1}^{N_\lambda} \Delta d_{pos}(\phi_n, \lambda_m, h_{MSL}) \tag{3.43}$$

where:
- N_ϕ: number of discrete geodetic latitude samples,
- N_λ: number of discrete geodetic longitude samples,
- ϕ_n: n^{th} geodetic latitude sample,
- λ_m: m^{th} geodetic longitude sample.

The sample standard deviation of the positioning error is a measure of dispersion, providing insight into the spread of the observations,

$$\sigma_{\Delta d_{pos}}(h_{MSL}) = \sqrt{\frac{1}{N_\phi N_\lambda} \sum_{n=1}^{N_\phi} \sum_{m=1}^{N_\lambda} \left(\Delta d_{pos}(\phi_n, \lambda_m, h_{MSL}) - \overline{\Delta d_{pos}(h_{MSL})}\right)^2} \tag{3.44}$$

The sample skewness coefficient of the positioning error is a measure of shape that provides insight into the asymmetry of the underlying distribution,

$$\gamma_{\Delta d_{pos}}^{S}(h_{MSL}) = \frac{\frac{1}{N_\phi N_\lambda} \sum_{n=1}^{N_\phi} \sum_{m=1}^{N_\lambda} \left(\Delta d_{pos}(\phi_n, \lambda_m, h_{MSL}) - \overline{\Delta d_{pos}(h_{MSL})} \right)^3}{\sigma_{\Delta d_{pos}}(h_{MSL})^3} \tag{3.45}$$

The sample kurtosis coefficient of the positioning error is a measure of shape that provides insight on the flatness of the underlying distribution's tail, distributions more prone to outliers than the normal distribution having a kurtosis coefficient higher than 3,

$$\gamma_{\Delta d_{pos}}^{k} = \frac{\frac{1}{N_\phi N_\lambda} \sum_{n=1}^{N_\phi} \sum_{m=1}^{N_\lambda} \left(\Delta d_{pos}(\phi_n, \lambda_m, h_{MSL}) - \overline{\Delta d_{pos}(h_{MSL})} \right)^4}{\sigma_{\Delta d_{pos}}(h_{MSL})^4} \tag{3.46}$$

When modelling a population's distribution, one should start by analysing the underlying phenomena that produced the observations, and narrow down the set of possible distributions to be fitted. The histogram plot, and the sample skewness and kurtosis coefficients, can also be used to select the families of distributions to take into consideration when making inferences about a population. Finally, the selected model should be the one that carries the best combination of theoretical foundation and goodness-of-fit. A thoughtful and comprehensive analysis revealed that the shifted exponential distribution best fulfils these criteria for the scenarios considered in this study.

The Probability Density Function (PDF) of the Shifted Exponential Distribution, for a random variable x distributed in the interval $[x_0, +\infty[$, is,

$$p_{Exp}(x; \overline{x_n}, x_0) = \frac{1}{\overline{x_n}} e^{-\frac{(x-x_0)}{\overline{x_n}}} \tag{3.47}$$

where:
- $\overline{x_n}$: shape parameter of the shifted exponential distribution,
- x_0: translation parameter of the shifted exponential distribution.

The maximum likelihood estimates for the Shifted Exponential Distribution parameters can be obtained from [82], [83] and [84],

$$\widehat{x_n} = \overline{\Delta d_{pos}} - \Delta d_{pos}^{min}$$

$$\widehat{x_0} = \Delta d_{pos}^{min} \tag{3.48}$$

where:
- $\widehat{x_n}$: maximum likelihood estimate for $\overline{x_n}$,
- $\widehat{x_0}$: maximum likelihood estimate for x_0,
- $\overline{\Delta d_{pos}}$: sample mean of the positioning error,
- Δd_{pos}^{min}: sample minimum of the positioning error.

3.3.2 Goodness-of-fit statistics

The Root Mean Square Error (RMSE) statistic is an absolute measure of fit, providing a sense of how close the predicted values are to the observed values being modelled,

$$\sqrt{\overline{\varepsilon^2}} = \sqrt{\frac{1}{N_{obs}} \sum_{i=1}^{N_{obs}} (y_i - \hat{y}_i)^2} \tag{3.49}$$

where:
- y_i: i^{th} observed value,
- $\hat{y}_i$: i^{th} predicted value,
- N_{obs}: number of observations.

The RMSE is particularly sensitive to large errors due to the intrinsic sum of squares, penalising large prediction errors more than smaller ones. A small number of outliers, relative to the number of observations, may inflate the RMSE although the fitted model provides a good representation for the underling behaviour of the population.

This statistic is an absolute measure of fit, in the same units of the observed sample being modelled; therefore, the interpretation of its value depends on the range of values associated with the system or population under study. For example, a RMSE of $1\,\text{m}$ may be insignificantly low if one is modelling asteroid trajectories, but, on the other hand, extremely large if one is modelling plant growth.

The coefficient of determination statistic is a relative measure of fit, quantifying the fitted model improvement in prediction compared to the arithmetic average model, which uses the arithmetic average of the observations for every prediction. For example, a coefficient of determination value of 0.80 means that the fitted model shows a percent prediction gain of 80% compared to the arithmetic average model [85]. The coefficient of determination is defined as,

$$R^2 = 1 - \frac{\sum_{i=1}^{N_{obs}} (y_i - \hat{y}_i)^2}{\sum_{i=1}^{N_{obs}} (y_i - \bar{y})^2} \tag{3.50}$$

where:
- $\bar{y}$: arithmetic average of the observed values.

This statistic is dimensionless, with values lower that 0.40 indicating that the model is a very bad analytical representation of the observed data, between 0.40 and 0.60 indicating that the proposed model does not show a reasonable improvement in prediction over the arithmetic average model, while between 0.60 and 0.80 indicating a good fit, and higher than 0.80 indicating that the fitted model is a very good analytical representation of the observed data [82].

This statistic has no penalty for an increase in model complexity or overfitting, thus making it an unreliable tool for model comparison and selection. Increasing the model complexity in terms of number of coefficients, may lead to an artificial increase in the coefficient of determination inside the observed

sample, although the fitted model may not be capturing the underling behaviour of the population.

The adjusted coefficient of determination statistic adds a penalty to the ordinary coefficient of determination presented in (3.50), by accounting for the residual degrees of freedom, being

$$R_{adj}^2 = 1 - (1 - R^2)\frac{N_{obs} - 1}{N_{obs} - N_{par} - 1}$$ (3.51)

where:
- N_{par}: number of parameters

Increasing a model's number of parameters may lead to increase or decrease the adjusted coefficient of determination, depending on the prediction gain that the new parameters bring to the model.

3.3.3 Goodness-of-fit tests

The chi-square goodness-of-fit test is used to determine whether a hypothesised theoretical distribution is a satisfactory population model. The null hypothesis, H_0, for this test is that the observed sample set comes from a population with the proposed theoretical distribution with parameters estimated from that same observed sample set. The test statistic is a measure of the difference between the vectors of observed and expected frequencies, being asymptotically chi-square distributed under the null hypothesis that the population follows the hypothesised distribution,

$$\chi_0^2 = \sum_{i=1}^{N_{class}} \frac{(O_i - E_i)^2}{E_i} \quad \overset{a}{\underset{H_0}{\sim}} \quad \chi_{p\%,\, N_{class}-N_{par}-1}^2$$ (3.52)

where:
- E_i: expected counts for the ith class, drawn from the theoretical distribution,
- O_i: observed counts for the ith class, drawn from the empirical distribution,
- N_{class}: number of class intervals.

Given a sample of a population and a theoretical distribution with parameters estimated from that sample, the test procedure consists of partitioning the sample data into classes or ranges of values and count the observed and expected absolute frequencies of each class. The null hypothesis is rejected if the test statistic is higher than the chi-square inverse cumulative distribution function parameterised with the required significance level value and the degrees of freedom.

3.4 Model assessment

Validation and assessment of the models used during simulations is critical in establishing the reliability of the experimental results. This section is dedicated to the assessment of the models and overall simulator used in this thesis. During the implementation process, several procedures were considered,

to ensure the correct operation of the simulator. The models were implemented in independent code functions, and the response of the individual functions to several inputs, was registered; the results where then compared with expected analytical values to validate the simulator. Finally, with the elementary algorithms validated, the overall simulator was assessed by comparison with data from real systems, and the literature.

3.4.1 Propagation model

Figure 3.15 depicts the results of the radio LoS simulator for a Fresnel radius of 100% (dark blue), 80% (green) and 0% (yellow). NAV Portugal own prediction for the scenario is depicted by the contour line. The scenario under analysis is Fanhões GS located at $38°53′16"N\ 9°09′46"W$, 20 m above ground level. The targets consist of an 178×134 target grid at FL 100 (3048 m) in the range $(42°N\ 13°W) - (36°N\ 5°W)$ with a horizontal resolution of 5km.
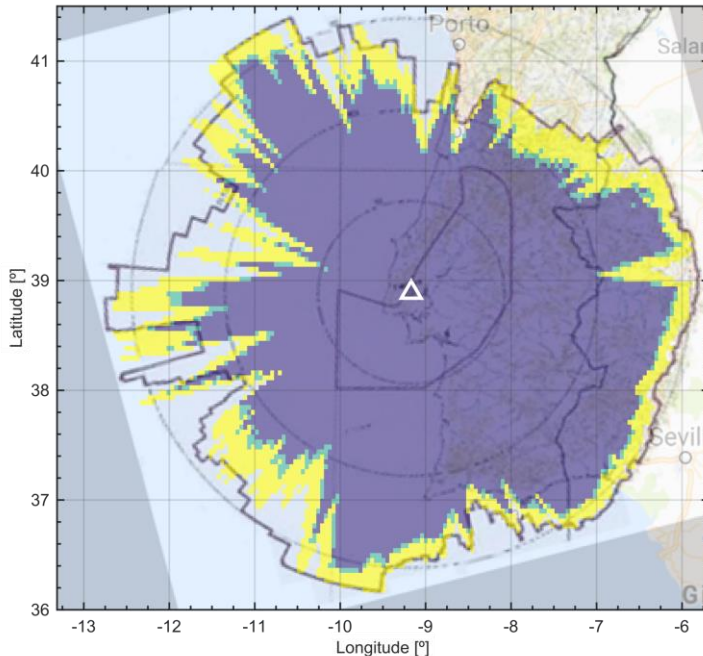
Figure 3.15 – Radio LoS model assessment.

A method for assessing the results would be to extract and compare the envelope of the coverage areas through statistical metrics, such as, the RMSE and the coefficient of determination; nonetheless, due to the intrinsic time limitations of this work, only visual comparison of the results is attempted.

Figure 3.16 shows the values of the inner variables of the simulator, concerning the LoS algorithm, for the scenario in Figure 3.15, and an aircraft at $36°30′00"N\ 8°00′00"W$. The refracted LoS is shown as curved line, in yellow, with the lower segment of the Fresnel ellipsoid, in green, beneath it. The geometric LoS is depicted as a black straight line. From Figure 3.15, it is possible to verify that this location is not covered by the Fanhões GS; in fact, this is clear from path profile, with the Fresnel ellipsoid being obstructed by Serra da Arrábida.
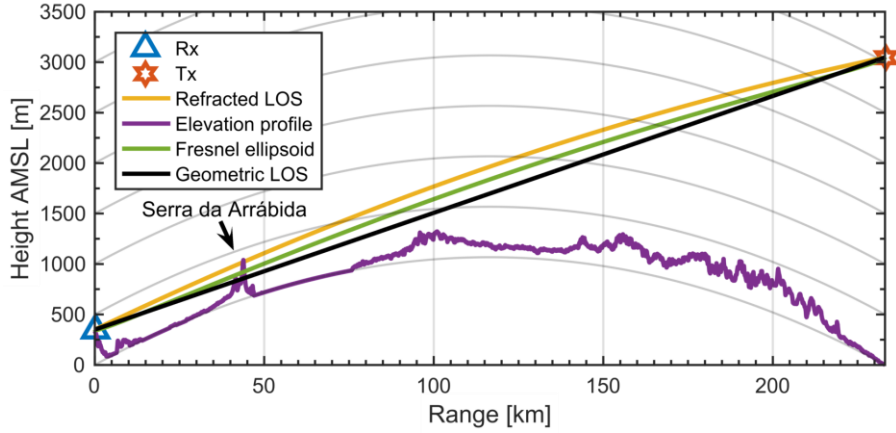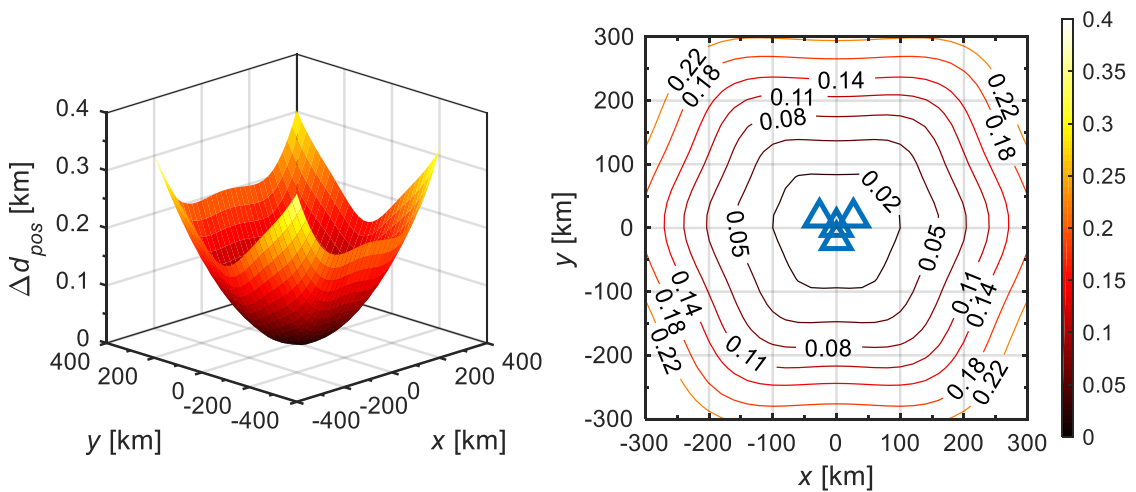
Figure 3.16 – Radio LoS model assessment.

3.4.2 Error model

The GDoP model is derived from a first-degree approximation to the hyperbolic system of equations that governs target localisation, expressed in the form of a simple matrix equation, allowing for a computationally less intensive evaluation of the system accuracy for a given target position and sensor network. The GDoP model was assessed by replication of results present in the literature. Additionally, the GDoP model was also compared with results from the hyperbole intersection approach developed in [86], and Monte Carlo simulation as explained in C.

Figure 3.17 shows the application of the GDoP model and simulator to a scenario presented in [42]. The target in assumed to be at a height of $8\,\text{km}$, and the sensor network is arranged in a four-sensor Wye configuration with coordinates: $R_0\,(0,0)\,\text{km}$, $R_1\,(-15\sqrt{3}, 15)\,\text{km}$, $R_2\,(15\sqrt{3}, 15)\,\text{km}$ and $R_3\,(0,-20)\,\text{km}$. For this scenario, the measurement error of the time differences is $\Delta d_{TDOA} = 0.3\,\text{m}$, the correlation coefficient between the measurement error of each time difference is $\eta = 0.3$, and the location error of each station is $\Delta d_{sensor} = 0.1\,\text{m}$. The simulation time was $703\,\text{ms}$ for a resolution of $20\,\text{km}$.

(a) RMS position accuracy, 3-D surface plot.

(b) RMS position accuracy, 2-D contour plot.

Figure 3.17 – Deterministic simulation (replicated from [42]).

Figure 3.18 shows the results for the stochastic simulation, by application of the Monte Carlo error model to the scenario in Figure 3.17. Simulation time was $6h\,50m$ for a confidence interval with normalised width of 20% at the 90% confidence level, and a resolution of $20\,km$.

(a) RMS position accuracy, 3-D surface plot.   (b) RMS position accuracy, 2-D contour plot.
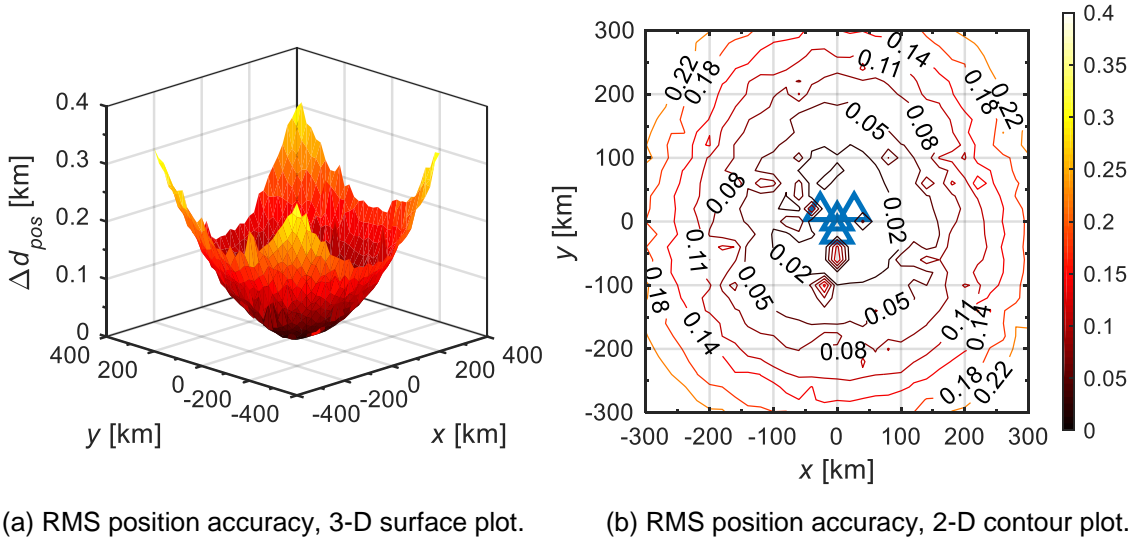
Figure 3.18 – Stochastic simulation with 600 runs.

The deterministic and stochastic simulations present similar results, with a coefficient of determination of 63.1% and a RMSE normalised to the average of 11.1%. It is worth noting that the run time of the stochastic simulation is unreasonable high, $35\,000$ times higher than that of the deterministic simulation.

3.4.3 Overall model

This subsection provides the assessment of the simulator presented in Section 3.2. Simulation results are compared with data from live ADS-B and WAM systems. The ADS-B data-set consists of an .xlsx file with 14 columns and $5\,571$ samples, Table 3.4 summarising the composition of the dataset. For simplification, only the columns used for this assessment are presented, the dataset contains a time series of the ADS-B messages reported by an aircraft, including its reported coordinates, the time stamp, and the reported barometric altitude. The WAM data set consists of an .xlsx file with 30 columns and $3\,292$ samples, Table 3.5 summarises the composition of the data set; again, for simplification, only the relevant columns are described. Figure 3.19 shows the evolution of the positioning error during the aircraft transit. The error was estimated by comparing WAM position estimates with ADS-B GNSS ones, assumed to have perfect accuracy. The WAM and ADS-B datasets did not have matching time stamps; for this reason, the WAM dataset was interpolated in time, to match the ADS-B time stamps.

Table 3.4 – Summary of the ADS-B data set.

Label	Format	Description
lat_WGS84	+DD.dddddd [º]	Latitude reported by the aircraft's GPS
lng_WGS84	+DD.dddddd [º]	Longitude reported by the aircraft's GPS
tmrp	HH:MM:SS.FFF	Time of message reception for position
modeC	Flight Level [hft]	Height above the isobaric surface of $1013.25\,hPa$

Table 3.5 – Summary of the WAM data set.

Label	Format	Description
lat_WGS84	+DD.dddddd [º]	Latitude computed by the WAM system
lng_WGS84	+DD.dddddd [º]	Longitude computed by the WAM system
tod	HH:MM:SS.FFF	Time of day
modeC	Flight Level [hft]	Height above the isobaric surface of $1013.25\ \mathrm{hPa}$
ru	Hexadecimal	Remote units used for the position computation
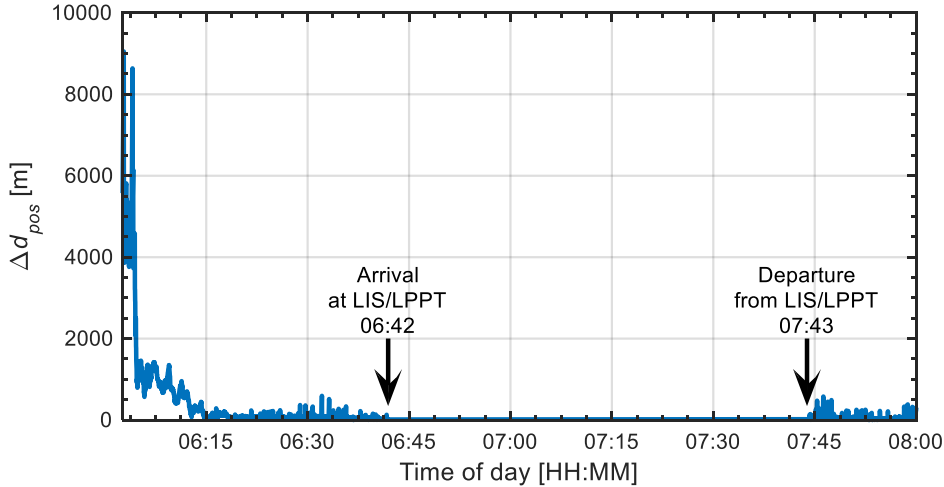
Figure 3.19 – Evolution of the system accuracy.

These findings suggest that accuracy is very poor in the edge of the system, rapidly increasing as the aircraft approaches the system centre. Figure 3.20 shows the histogram for the values in Figure 3.19, the results suggest that the positioning error during the aircraft routing may be well-described by an Exponential Distribution. Positioning error estimates obtained from the simulator, show a similar histogram, suggesting that the simulator provides trustworthy results.
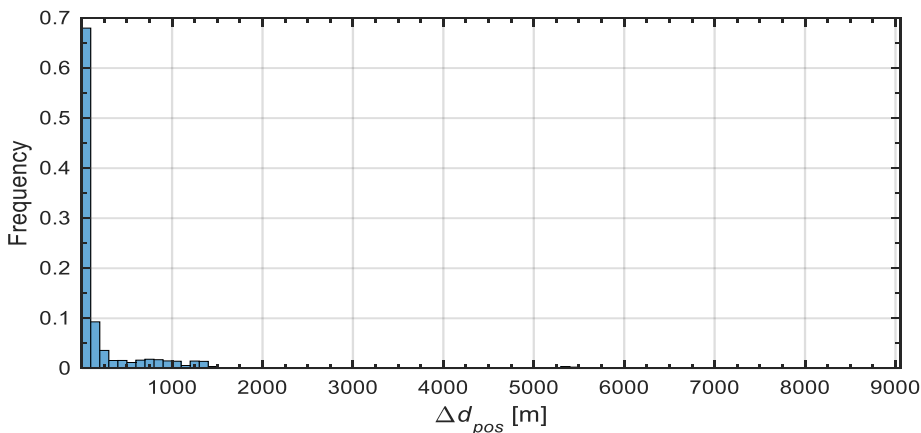
Figure 3.20 – Histogram of the system accuracy for a bin width of $100\ \mathrm{m}$.

Table 3.6 displays the descriptive statistics of the positioning error; although prohibitive errors are obtained as the aircraft enters the interest area of the system, they rapidly decay, and accurate position estimates are obtained. In fact, 50% of the recorded errors where between $0.78\ \mathrm{m}$ and $66.01\ \mathrm{m}$.

Table 3.6 – Descriptive statistics of the dataset.

Parameter	Value [m]
Maximum	9052.87
Minimum	0.78
Average	339.81
Median	66.01
Standard Deviation	914.10

Chapter 4

Results analysis

This chapter provides the description of the scenarios for the performance analysis, and the analysis of solutions and of their implementation. The chapter starts with the description of the GSs and simulation parameters for the scenarios under study. Then, an analysis of results from the model for a set of canonical scenarios found in the literature is provided. The chapter ends with the results from the model for the scenarios under study.

4.1 Scenarios development

The system studied in this thesis was proposed by NAV Portugal, and results from tenders submitted by system manufacturers for the South Portugal WAM project; henceforth, this system is referred to as Faro WAM. Figure 4.1 shows the locations of the GSs of the Faro WAM system, superimposed with a map from Google Maps.
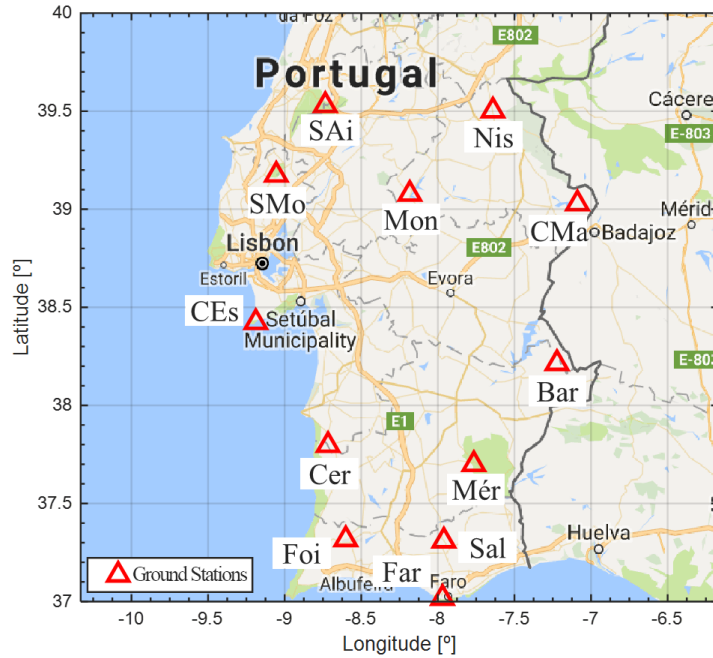
Figure 4.1 – Overview of the Faro WAM system.

As seen from Table 4.1, the Faro WAM system is composed of 12 GSs, 3 of them being shared with the Lisbon WAM system (Montargil, Cabo Espichel, and Serra de Montejunto).

Table 4.1 – Ground stations of the Faro WAM system.

GS ID	Location	Latitude [º]	Longitude [º]	Height AMSL [m]
01 Mon	Montargil	39.07725	-8.18757	243.7
02 CEs	Cabo Espichel	38.42431	-9.18590	176.7
03 SMo	Serra de Montejunto	39.17386	-9.05346	675.2
04 SAi	Serra de Aire	39.53205	-8.73209	567.2
05 Cer	Cercal	37.79451	-8.71825	343.9
06 Foi	Foia	37.31357	-8.60024	893.2
07 Far	Faro TWR	37.01907	-7.97109	26.0
08 CMa	Campo Maior	39.02724	-7.08595	339.8
09 Bar	Barrancos	38.21448	-7.22676	239.3
10 Nis	Nisa RT	39.50340	-7.64286	308.2
11 Sal	Salir DME RT	37.30761	-7.96246	586.9
12 Mér	Mértola DME RT	37.70088	-7.76380	353.7

It should be noted that the GSs are distributed in a way that maximises the distance between each other, and the distance to the centre of mass of the system, which is a characteristic of hyperbolic positioning

systems, as the accuracy of the system improves for wider baselines between sensors, proven that radio coverage is not put at risk. The multiplicative error factor, due to the geometry effect of the system, in the TDoA system of equations, decreases with the number of sensors, and the angular displacement associated with any pair of sensors and a target.

The height of the GS' antenna, Table 4.1, is for a mast height of 12 m, which does not correspond entirely to reality, but is considered a good approximation for the problem at hand. The average altitude of the GSs is 396.2 m, the highest one, Foia, being at 893.2 m, at the summit of Serra de Monchique, in South-West Portugal; in contrast, the GS at the lowest point, 26.0 m, is located at Faro's airport.

Table 4.2 contains the scenario parameters, their typical value, and their reference,

Table 4.2 – Faro WAM scenario parameters for the simulator.

Parameter	Downlink reply channel	Comment
Carrier Frequency $[\text{MHz}]$	1090	[17]
Transmitter power $[\text{dBm}]$	54	Average value for aircraft transponders, [87] and [17]
Transmitter cable and diplexer insertion loss $[\text{dB}]$	3	[51]
Transmitting antenna gain $[\text{dBi}]$	Nonparametric model	Simulations for a narrow-body, commercial passenger, twin-engine jet airliner
Propagation model	Free-Space Path Loss Model with first Fresnel ellipsoid clearance of 100%	-
Polarisation loss $[\text{dB}]$	1	[51]
Receiving antenna gain $[\text{dBi}]$	Nonparametric model	[75]
Receiver cable and diplexer insertion loss $[\text{dB}]$	1	[51]
Receiver noise factor $[\text{dB}]$	5	Value used in [73] and [74]
Noise bandwidth $[\text{MHz}]$	6	[11]
Required CNR $[\text{dB}]$	6.3	Analytically determined
Fast Fading due to multipath $[\text{dB}]$	0 and 26	[51]
Slow Fading due to airframe shadowing and orientation uncertainty $[\text{dB}]$	0 and 3	[46]

Figure 4.2 shows the used DEM, consisting of a file with $12\,598 \times 12\,599$ elevation cells; the maximum elevation is 1087 m, and the minimum -6 m, with an average elevation of 153.22 m, and standard deviation 150.97 m.
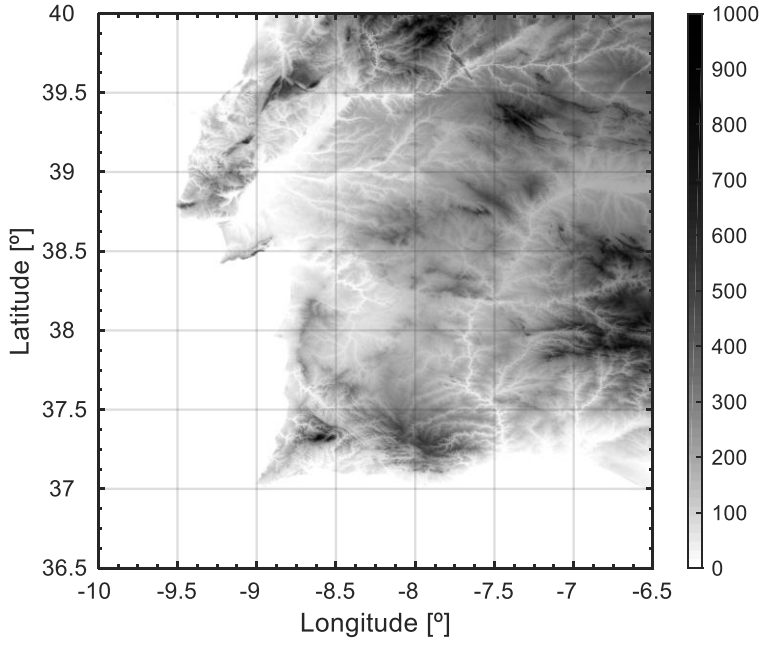
Figure 4.2 – Digital Elevation Model.

The elevation pattern for the aircraft shadowing, obtained in Section 3.2.6, is depicted in Figure 4.3.
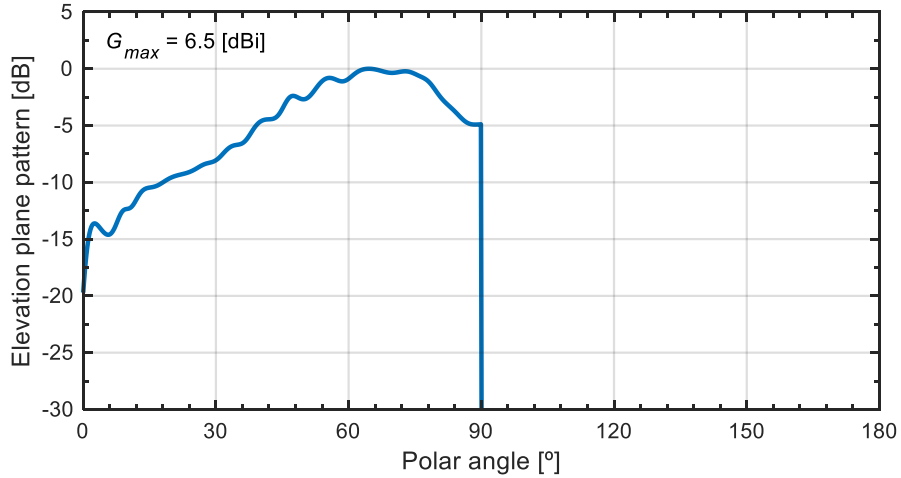
Figure 4.3 – Elevation plane pattern for the aircraft.

The analysis variability comprises three distinct parameters, the FL, the required fading margin, and the GSs availability. The system is analysed at four typical aircraft altitudes, $FL050\,(1524\,m)$, $FL100\,(3048\,m)$, $FL200\,(6096\,m)$, and $FL300\,(9144\,m)$. Considering the required fading margins, two scenarios are defined, the most favourable scenario, with a required margin of $0\,dB$; and the least favourable scenario, with a required margin of $29\,dB$. Finally, regarding GS availability, two resilience scenarios are defined, the $N_{GS} - 1$, where the system performance is analysed for a loss of one GS, corresponding to 12 possible networks; and the $N_{GS} - 2$, where the system performance is analysed for a loss of two GSs, corresponding to 66 distinct networks.

4.2 Canonical scenarios

This section provides a study of the target and sensors relative positions effect on GDoP. The framework for this analysis is shown in Figure 4.4. The canonical scenarios engine generates the sensor coordinates considering a set of predefined scenario conditions, the number of sensors, and the sensor baseline; subsequently, the GDoP simulator is fed with the generated sensors coordinates matrix and the target coordinates. The target coordinates are taken from a uniform square grid of 31×31 points on the plane $z = 12.2$ km (FL 400) with limits at $x_{max} = -x_{min} = y_{max} = -y_{min} = 150$ km. The sensor baseline is 100 km, a typical value for the aeronautical multilateration scenario [11].

```
┌──────────────────┐      ┌──────────────────┐      ┌──────────────────┐
│ Canonical        │      │                  │      │                  │
│ scenarios        │ ───▶ │ GDOP simulator   │ ───▶ │ GDOP isolines    │
│ engine           │      │                  │      │ plot             │
└──────────────────┘      └──────────────────┘      └──────────────────┘
```
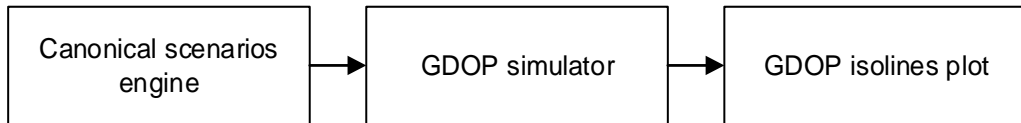
Figure 4.4 – Canonical scenarios analysis framework.

Table 4.3 presents the canonical scenarios considered for this assessment, these scenarios are based on what is typically found in the literature, concerning hyperbolic positioning systems.

Table 4.3 – Canonical scenarios extracted from the literature and adapted to the WAM conditions.

Scenario	Number of Ground Stations	Reference
Delta Configuration	3	[88]
Wye Configuration	4	[38], [42], [89], [41], [11]
Square Configuration	4	[38], [89], [88]
Parallelogram Configuration	4	[38]
Cross Configuration	5	[11]

Taking into account previous results from the literature, one expects GDoP to display an inversely proportional trend with the number and angular distance (or apparent separation) of the sensors seen by the target [86]. Furthermore, the effect of small angular distances over GDoP should decrease as the number of sensors increases [86].

Figure 4.5 presents GDoP for a configuration of three sensors; as the angle between any two sensors and a target decreases, GDoP increases. GDoP has its minimum for targets in the centre of the shape defined by the three sensors, increases rapidly outside the shape, and reaches unfeasible high values if the target is aligned with any two sensors. Inside the triangular shape, the GDoP is smaller than 2.

Figure 4.6 displays GDoP for a wye geometry. Compared with the scenario depicted in Figure 4.5, this shape reveals a significant improvement in performance, for targets outside the sensors geometry, at the cost of an additional sensor. Again, inside the sensors baseline, GDoP is always bellow 2. Outside the geometric region defined by the sensors, GDoP increases at a sub-exponential rate; moreover, when the target is collinearly aligned with any two sensors, GDoP is much smaller than one would expect, considering the results of the triangular array shown in Figure 4.5.

(a) GDoP, 3-D contour plot.

(b) GDoP, 2-D contour plot.
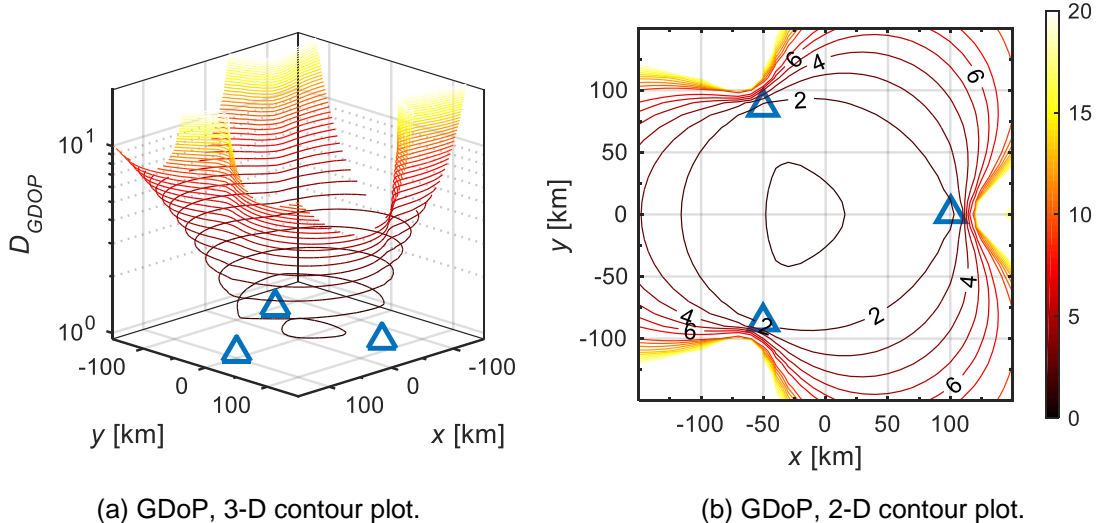
Figure 4.5 – GDoP for a triangular distribution of sensors, target height is 12.2 km.

(a) GDoP, 3-D contour plot.

(b) GDoP, 2-D contour plot.
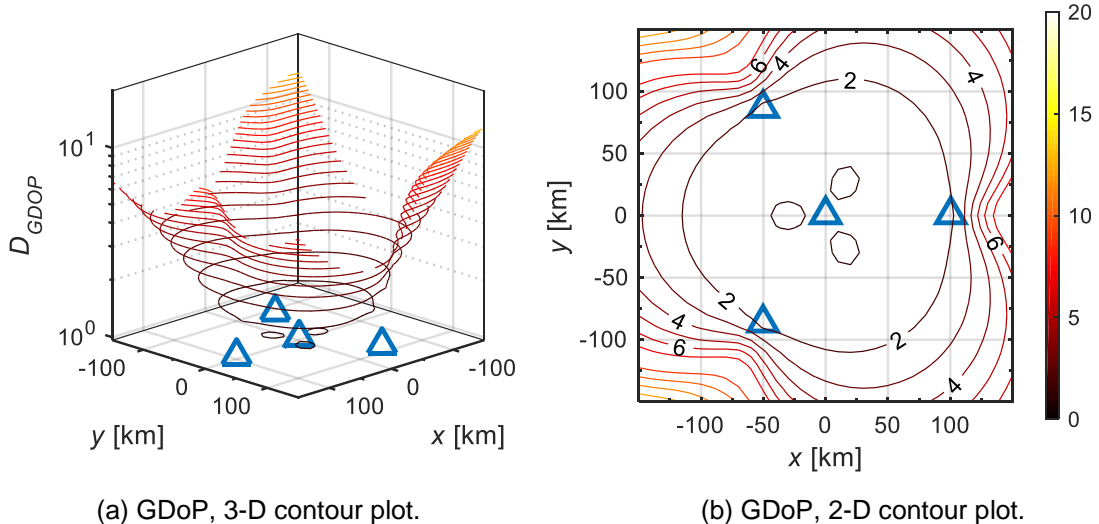
Figure 4.6 – GDoP for a Wye distribution of four sensors, target height is 12.2 km.

Figure 4.7 shows the GDoP surface for a square sensor deployment. As with the previous scenarios, inside of the region defined by the sensors, GDoP is below 2. Outside this region, GDoP increases with a sub-exponential growth. Figure 4.8 shows the GDoP for the cross-distribution scenario. Again, the area confined by the sensors displays a GDoP below 2.

The GDoP in known to be associated with the uniformity of the network, Figure 4.9 shows the GDoP for the parallelogram distribution of four sensors, a scenario equivalent to the square distribution, with a change in the placement of two sensors; system accuracy is greatly reduced, because of the narrowing of the angular displacement between a target and a pair of sensors.

These findings suggest that, for a given FL, the sensor distribution has a small effect on performance for targets inside, or close to the region defined by the network. However, GDoP behaviour changes drastically as the target moves away from the centre of the sensor network, this effect being more relevant for networks with less sensors, or with a non-uniform distribution of sensors.

(a) GDoP, 3-D contour plot.

(b) GDoP, 2-D contour plot.
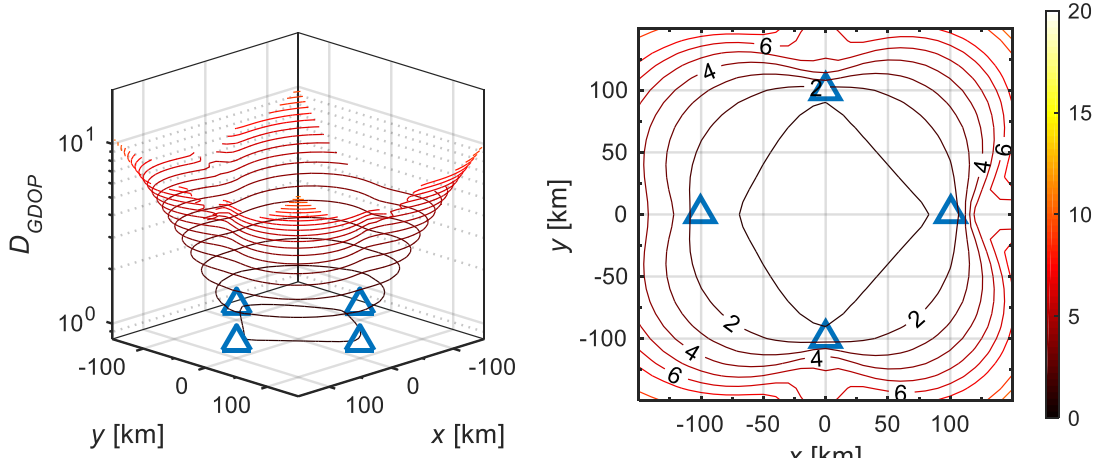
Figure 4.7 – GDoP for a square distribution of four sensors, target height is 12.2 km.

(a) GDoP, 3-D contour plot.

(b) GDoP, 2-D contour plot.
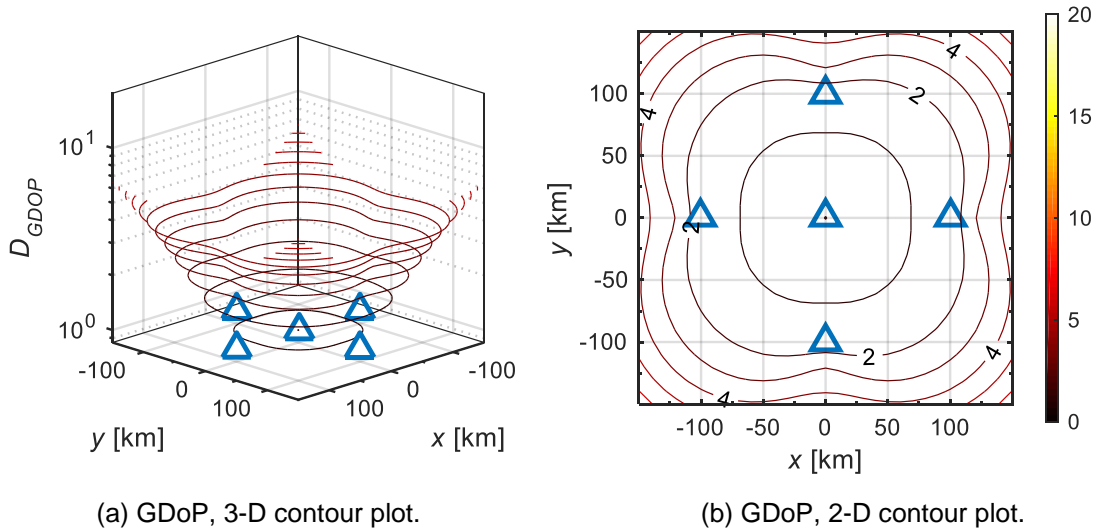
Figure 4.8 – GDoP for a cross distribution of five sensors, target height is 12.2 km.

(a) GDoP, 3-D contour plot.

(b) GDoP, 2-D contour plot.
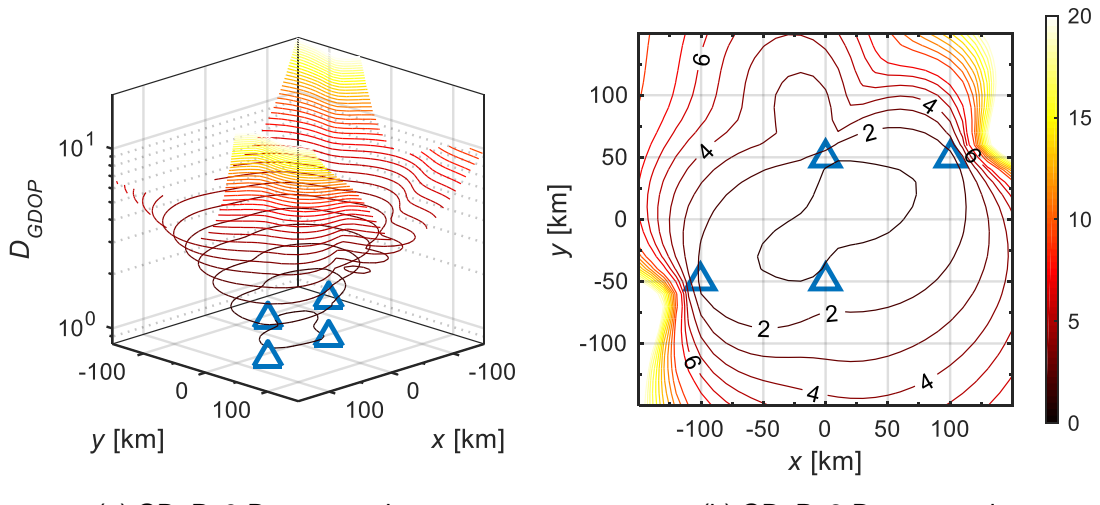
Figure 4.9 – GDoP for a parallelogram distribution of four sensors, target height is 12.2 km.

4.3 Most favourable scenario

This section provides the simulation results for the analysis of performance of the Faro WAM system, as described in Section 4.1, for the most favourable scenario. To study aircraft location accuracy, one starts by independently estimate the propagation coverage of each GS, using the PrM simulator. The results of this process are illustrated in Annex D, Figure D.1, where the propagation coverage maps, for each GS, at the considered aircraft FLs, are shown. The results suggest that for inland GSs, coverage is mostly limited by the terrain profile; in contrast, for coastal GSs, coverage is mostly limited by the radio horizon limitation in the ocean direction, and by the terrain profile in the continental one. These estimates also suggest a linear relationship between the extent of the coverage contour, or radius, and the FL, despite the effect of the terrain profile. Figure 4.10 provides a numerical comparison of the coverage maps. Comparing with the location of the GSs in Table 4.1, as one may expect, results suggest that GSs placed in higher hills display, between 3 to 2 times more coverage area, than GSs placed in lower terrain; as a matter of fact, GSs {Far, CMa, Bar and Nis} do not provide significant coverage at the lower FLs, which should be taken into account during the reliability analysis, as one could expect these GSs, not to be important to the system global coverage, when considering the limitations in accuracy, and the loss of a GS.
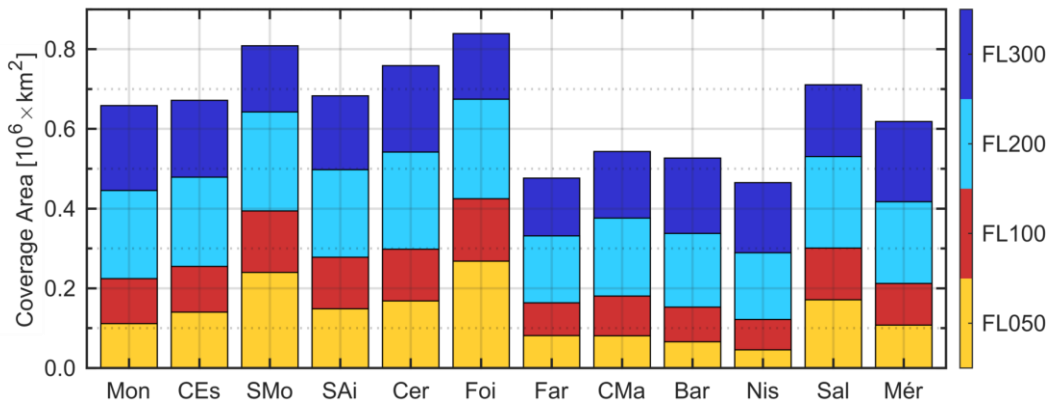
Figure 4.10 – Propagation coverage areas for each GS ($M_{F\,SF} = 0$ dB, and $M_{F\,FF} = 0$ dB).

It should be recalled that the multilateration algorithm requires at least 3 sensors to resolve aircraft position, and that system accuracy is a function of the number and location of GSs. Therefore, the results presented in Figure D.1, must be combined, to get a local estimate of the GSs offering coverage to each longitude and latitude sample, which in turn, is used by the ErM simulator to compute a local estimate of the system accuracy. Figure 4.11 provides an insight into the system global coverage, presenting the coverage maps for the number of GSs available per region, to the ErM simulator. These results suggest that the Faro WAM system can singly provide radio coverage to most of mainland Portugal, with at least 3 sensors, this finding being contrasted latter with the results of the ErM simulator. Figure 4.12 provides a numerical comparison of the results in Figure 4.11. These findings suggest that the area covered by all GSs is very limited in the lower FLs. The number of sensors available for a position estimation is critical in hyperbolic positioning systems; and one should expect the accuracy inside the regions with more sensors, towards the centre of the network, to be greater.

(a) FL050.

(b) FL100.

(c) FL200.

(d) FL300.
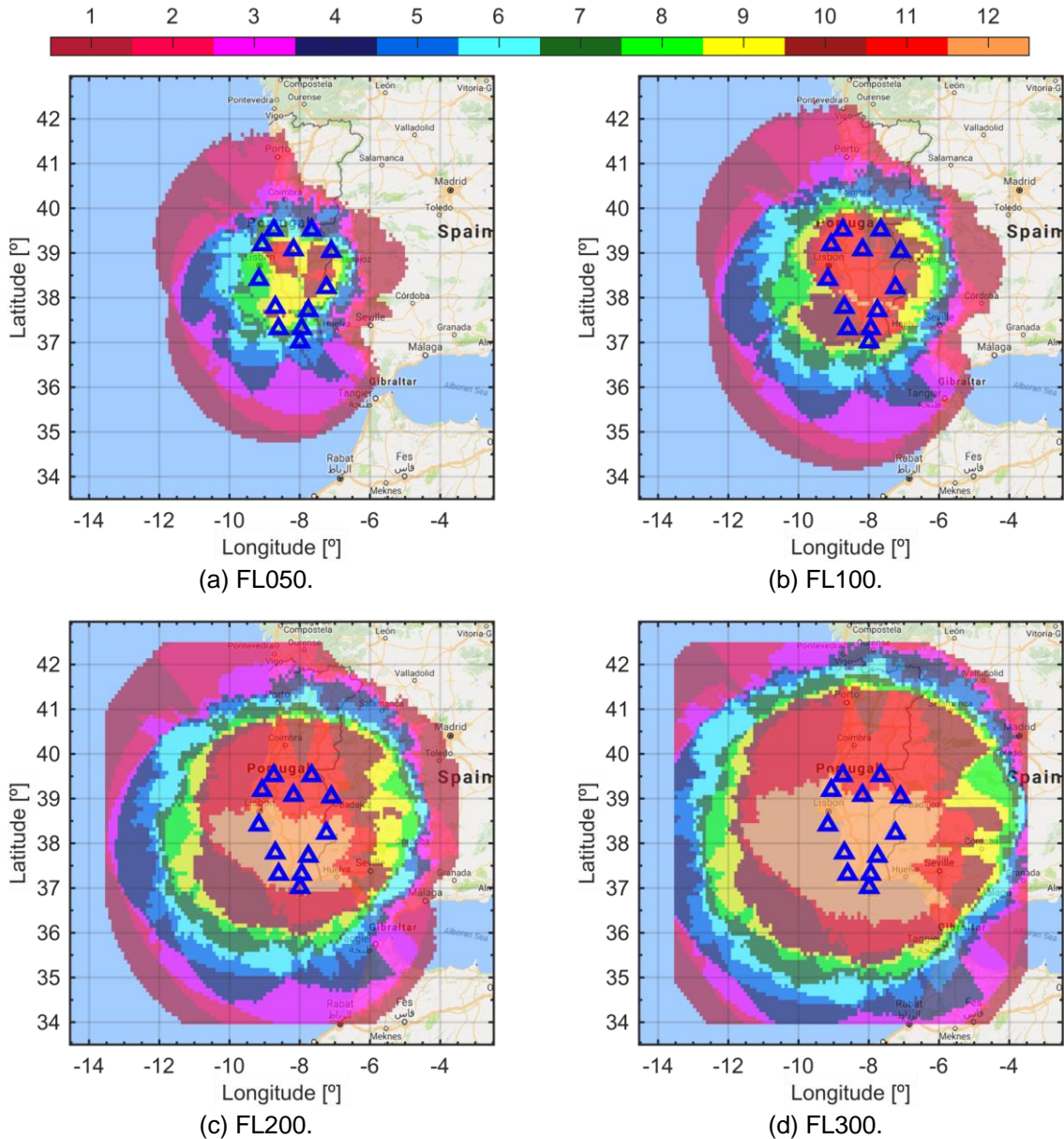
Figure 4.11 – Cumulative coverage maps for the number of GSs ($M_{F\,SF} = 0$ dB, and $M_{F\,FF} = 0$ dB).
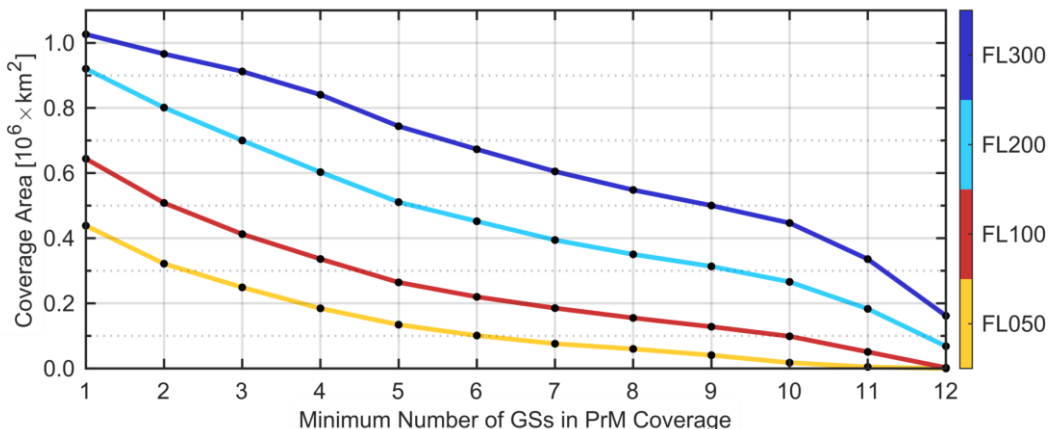
Figure 4.12 – Cumulative coverage area for the number of GSs ($M_{F\,SF} = 0$ dB, and $M_{F\,FF} = 0$ dB).

The ErM simulator provides local estimates of the system accuracy for each longitude and latitude pair, by combining the information computed from the PrM simulator for each GS. Figure 4.13 shows the aircraft RMS positioning error threshold coverage maps, for the number of GSs available per region, for the error threshold of $\Delta d_{pos\,max} = 150$ m, as defined by EUROCONTROL. The results are provided separately for each FL. In contrast with Figure 4.11, the propagation coverage maps for the number of GSs available per region are now shown with the limitation introduced by the error threshold. Visual inspection of the results immediately suggests that the global system coverage is much smaller, now that system accuracy requirements are taken into consideration.

(a) FL050.

(b) FL100.

(c) FL200.

(d) FL300.
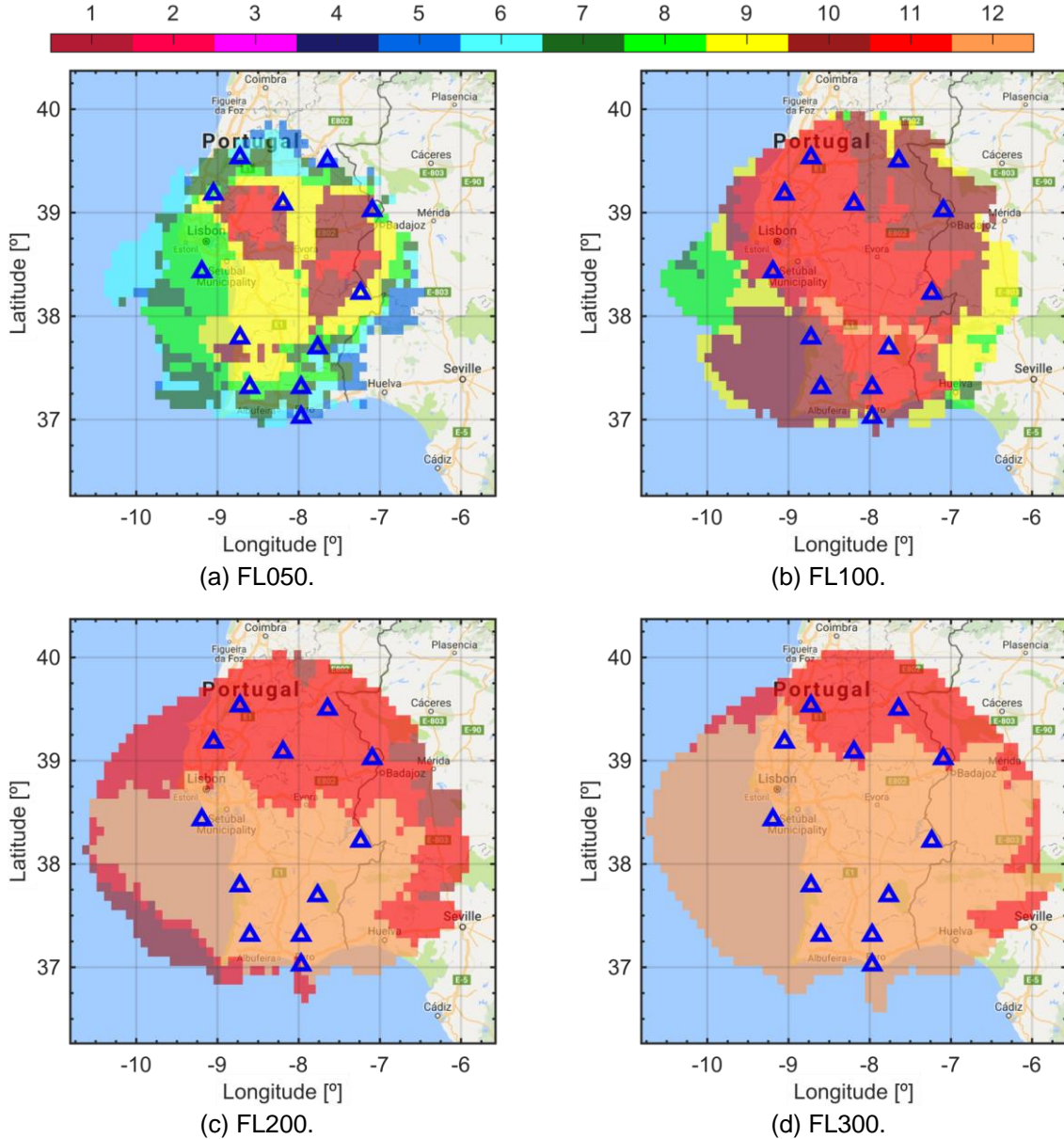
Figure 4.13 – Cumulative coverage maps for the number of GSs, with the limitation introduced by the aircraft RMS positioning error threshold ($\Delta d_{pos\,max} = 150$ m, $M_{F\,SF} = 0$ dB, and $M_{F\,FF} = 0$ dB).

The saturation of the cumulative coverage areas for different number of GSs, is apparent from Figure 4.14, where a numerical comparison of the results in Figure 4.13 is presented. These findings suggest

that for the higher FLs, accuracy is not limited by the number of GSs; instead, accuracy appears to be limited by the geometry of the system; in other words, the limiting factor is the narrowing of the apparent angle between the aircraft and any pair of sensors, as it moves away from the centre of the system. Moreover, one may expect that removing a sensor in these conditions does not affect performance.
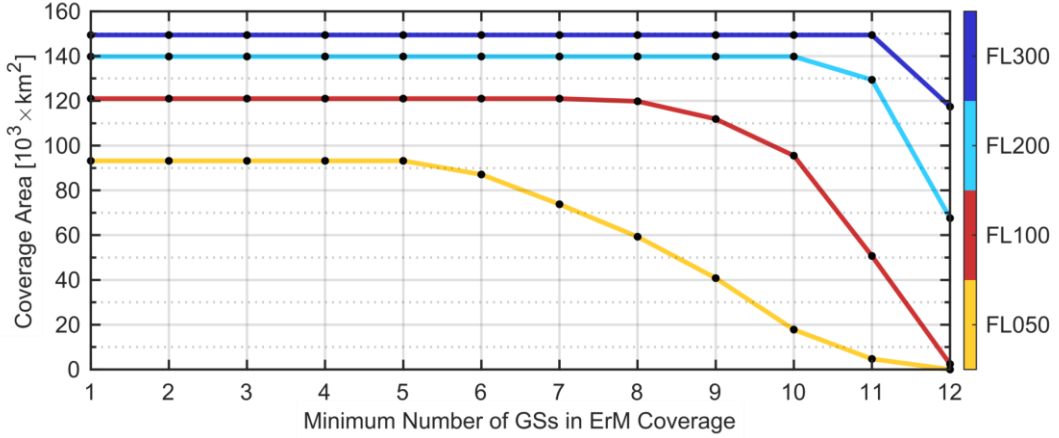
Figure 4.14 – Cumulative coverage area for the number of GSs, with the limitation introduced by the aircraft RMS positioning error threshold ($\Delta d_{pos\,max} = 150$ m, $M_{F\,SF} = 0$ dB, and $M_{F\,FF} = 0$ dB).

Figure 4.15 provides the spatial distribution of the positioning error. As one may expect from the results in Section 4.2, the positioning error has its lower values inside the region delimited by the GSs; with a guaranteed maximum RMS positioning error of 50 m, for all FLs. The positioning error was computed for every longitude and latitude sample with at least three corresponding GSs available; as seen previously in Figure 4.11, this region corresponds to the area painted in light magenta. In what follows, the statistical analysis is provided for the spatial distribution of the positioning error inside this region.

In Figure 4.16, a histogram for each FL is presented with the corresponding proposed theoretical model for the population. The histograms suggest a saturation of the positioning error towards the minimum value, which is also confirmed by inspection of the raw positioning error values. The histograms are plotted with the Shifted Exponential Distribution fitted by maximum likelihood estimation for the observations at each FL. The proposed theoretical distribution overestimates the positioning error, failing to correctly model the saturation around the minimum. Nonetheless, the Shifted Exponential Distribution is suggested as a model for the spatial behaviour of the positioning error population, exhibiting the best ratio between model goodness-of-fit, model complexity, and explanatory power.

Due to the significant increase in coverage with FL, the number of longitude and latitude samples is much higher for higher FLs; this expansion of the region considered for error analysis, matched with a decrease in the angular displacement between any pair of GSs and a sample, causes the tails of the empirical distribution to grow with higher FLs.

Table 4.4 provides the descriptive and inferential statistics for the results in Figure 4.15, the former displaying a linear relationship with FL; note that all statistics but the minimum positioning error, increase with increasing FL. The growth with FL of the region covered by at least 12 GSs may suggest an explanation for the slightly decrease with FL of the minimum value seen for the positioning error dataset.
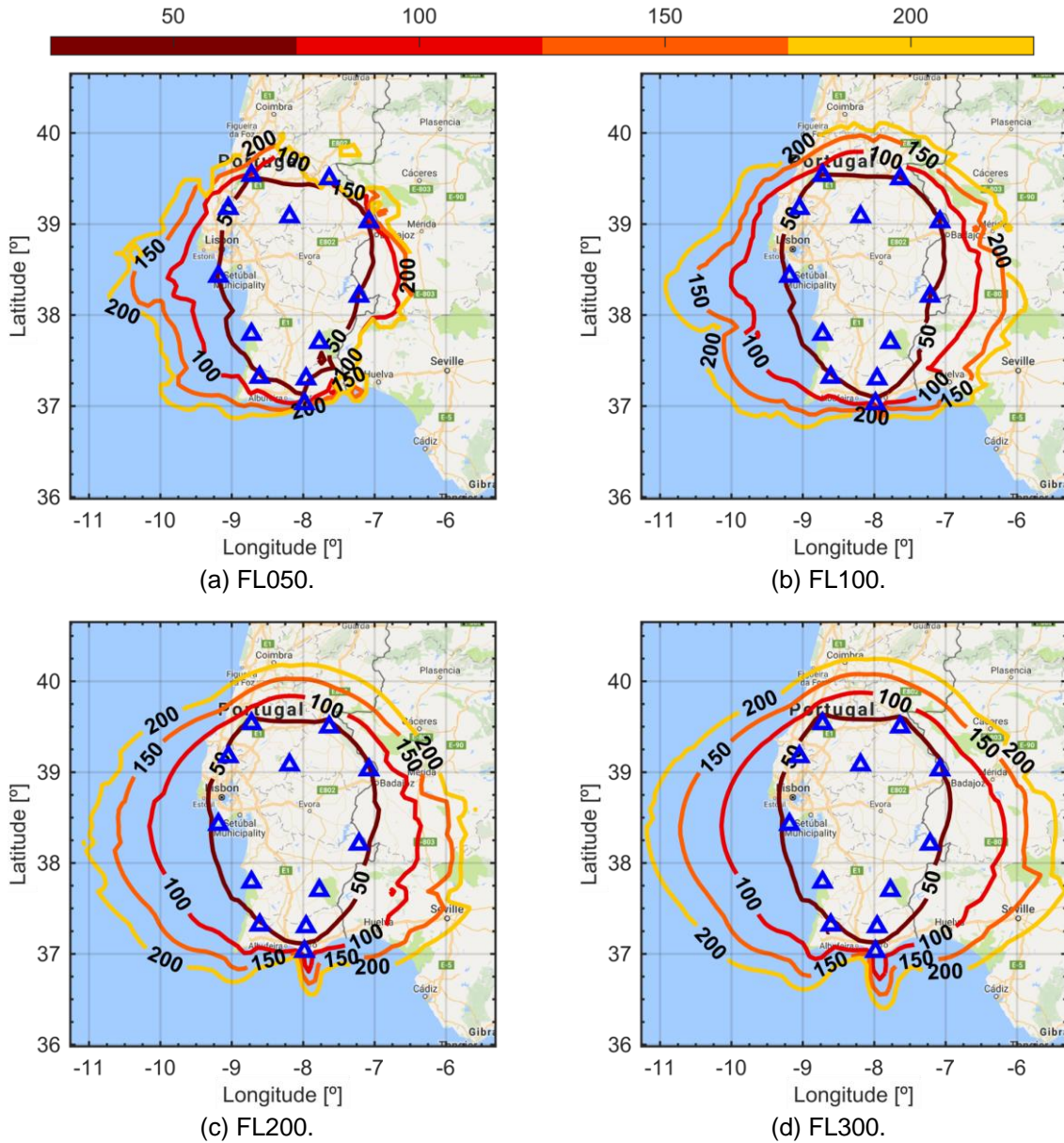
Figure 4.15 – Aircraft RMS positioning error spatial distribution ($M_{F\,SF} = 0$ dB, and $M_{F\,FF} = 0$ dB).

The results for the inference on the positioning error population are also presented in Table 4.4, the chi-squared goodness-of-fit test rejects the hypothesis that the data is consistent with the Shifted Exponential Distribution, which is explained by the inability of the theoretical distribution to model the saturated observations about the minimum, and the sensitivity of the chi-squared goodness-of-fit test to outliers. Alternative metrics, such as the RMSE, the coefficient of determination, and the adjusted coefficient of determination, display reasonable results that validate the proposed theoretical distribution. The regression analysis of the theoretical distribution's parameters suggests a linear relationship with FL. The estimates for the shape parameter of the Shifted Exponential Distribution, as a function of FL, are well-approximated by a linear regression, with a slope parameter of 208.08 m FL^{-1} and an intercept parameter of -139.15 m, showing a coefficient of determination value of 98.68%. The estimates for the translation parameter of the Shifted Exponential Distribution, as a function of FL, are reasonably well-approximated by a linear regression with a slope parameter of -0.62 m FL^{-1} and an

intercept parameter of 29.65 m, showing a coefficient of determination value of 80.76%. It is worth mentioning that the amount of FLs under study is inadequate to validate these regressions.

(a) FL050.

(b) FL100.
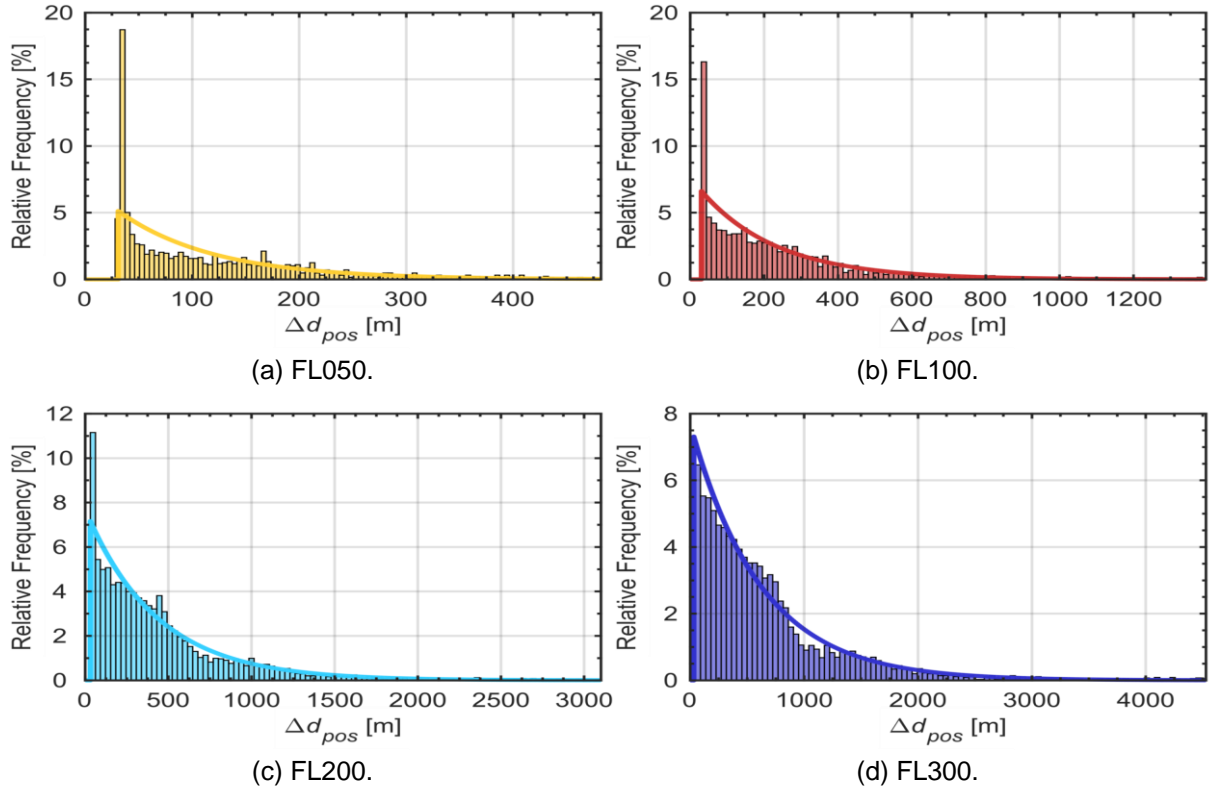
(c) FL200.

(d) FL300.

Figure 4.16 – Aircraft RMS positioning error histogram and fitted distribution

($M_{F\,SF} = 0$ dB, and $M_{F\,FF} = 0$ dB).

Table 4.4 – Aircraft RMS positioning error descriptive and inferential statistics

($M_{F\,SF} = 0$ dB, and $M_{F\,FF} = 0$ dB).

			FL050	FL100	FL200	FL300
Descriptive Statistics	Percentiles	$\Delta d_{pos\,[m]}^{max}$	1604.9	5148.5	31681.6	59072.9
		$\Delta d_{pos\,[m]}^{95\%}$	374.0	882.6	1742.2	2387.2
		$\Delta d_{pos\,[m]}^{50\%}$	86.4	169.8	325.6	463.6
		$\Delta d_{pos\,[m]}^{min}$	29.4	27.9	27.7	27.4
	Moments	$\Delta d_{pos\,[m]}^{\mu}$	131.9	278.0	548.7	780.1
		$\Delta d_{pos\,[m]}^{\sigma}$	145.3	396.0	916.2	1325.4
		$\gamma_{\Delta d_{pos}}^{s}$	3.7	4.9	11.7	14.5
		$\gamma_{\Delta d_{pos}}^{k}$	23.8	40.1	306.1	526.8
Inferential Statistics	Fit	$\widehat{\Delta d}_{pos\,[m]}^{\mu}$	97.4	233.4	486.9	706.5
		$\widehat{\Delta d}_{pos\,[m]}^{\mu_0}$	29.4	27.9	27.7	27.4
	GOF	χ_0^2	791.6	262.9	740.2	478.2
		$\chi_{95\%}^2$	38.9	46.2	55.8	59.3
		$\sqrt{\overline{\varepsilon^2}}_{[\%]}$	1.6	0.9	1.0	0.3
		$R^2_{[\%]}$	54.8	86.3	74.5	98.4
		$R^2_{adj\,[\%]}$	51.4	85.4	73.2	98.3

Table 4.5 provides the first order resilience analysis for the overall system coverage, considering the PrM and ErM simulations, for a positioning error threshold of $\Delta d_{pos\,max} = 150$ m. The table is coloured as a function of the percent coverage loss experienced by the system when a GS is removed. The global coverage loss, corresponds to the percent coverage loss considering the shaded shapes presented in Figure 4.13. The interest area coverage loss, corresponds to the percent coverage loss considering the same shaded shapes, but limited to the East, at 7ºW, and to the North, at 39ºN.

Table 4.5 – Resilience analysis percent loss for the aircraft RMS positioning error threshold coverage area for $N_{GS} - 1$ ($\Delta d_{pos\,max} = 150$ m, $M_{F\,SF} = 0$ dB, and $M_{F\,FF} = 0$ dB).

[%]	Global Coverage Loss				Interest Area Coverage Loss			
	FL050	FL100	FL200	FL300	FL050	FL100	FL200	FL300
Mon	5.26	1.32	3.43	5.42	3.20	1.04	2.27	2.84
CEs	6.44	6.36	6.22	8.50	6.40	5.80	3.40	3.57
SMo	7.83	6.28	6.51	8.77	6.28	5.28	5.00	5.87
SAi	7.51	8.10	10.44	12.72	6.16	6.42	8.03	9.26
Cer	8.48	3.31	4.58	5.96	6.87	2.90	3.31	3.12
Foi	8.69	5.54	8.15	9.50	9.60	5.80	7.18	6.60
Far	7.19	8.02	12.37	15.60	7.94	8.90	11.43	12.65
CMa	6.33	8.84	8.08	10.37	1.78	0.72	2.46	3.94
Bar	4.72	2.64	7.37	7.97	2.49	1.45	6.70	5.59
Nis	2.90	3.39	8.73	11.31	0.95	0.41	2.64	4.03
Sal	6.33	7.44	8.30	8.57	4.03	3.21	4.34	4.12
Mér	5.26	2.64	4.29	6.02	3.08	1.24	2.55	2.47

Annex E, Table E.1, provides the second order resilience analysis for the overall system coverage, considering the PrM and ErM simulations, for a positioning error threshold of $\Delta d_{pos\,max} = 150$ m. The table is coloured as a function of the percent coverage loss, experienced by the system when two GSs are removed. By removing GSs in the centre of the covered area, such as Mon or Mér, the global coverage loss is not much affected; on the other hand, removing GSs in the limit of the system affects coverage by as much as 20%.

4.4 Least favourable scenario

This section concerns the analysis of the least favourable scenario. Again, to assess the global coverage of the Faro WAM system, one starts by independently estimating the coverage of each GS, in the PrM simulator. These results are expressed in Figure D.2, where the coverage maps for each FL and for each of the GSs, are shown. In this scenario, coverage is mostly limited by path loss; coverage limitations by the terrain are now reserved for GSs with obstacles very close to the antenna. Figure 4.17 provides a numerical comparison of the coverage maps.
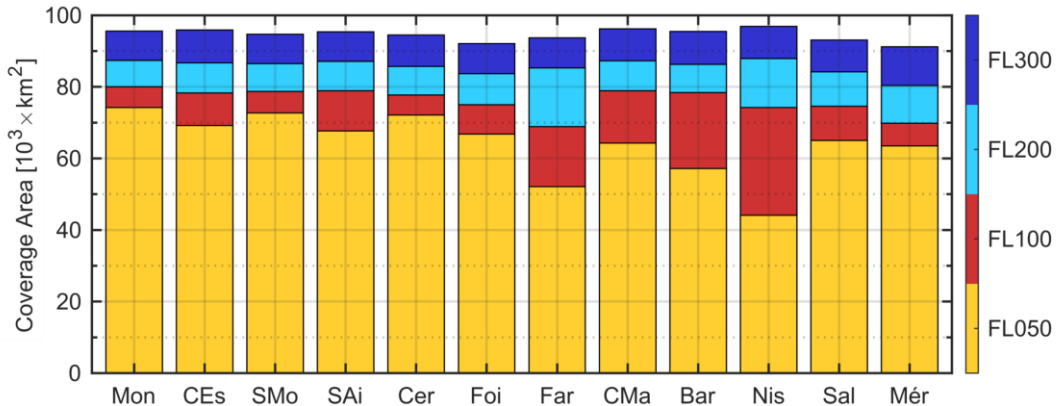
Figure 4.17 – Propagation coverage areas for each GS ($M_{F\,SF} = 3$ dB, and $M_{F\,FF} = 26$ dB).

Mostly limited by the path loss, the coverage area is now uniform for the higher FLs, despite GS altitude. Unremarkably, the coverage area decreases by one order of magnitude for the GSs that in the most favourable scenario display the highest coverage.

Figure 4.18 presents the coverage maps for the minimum number of GSs available per region. The decrease in coverage per GS is severely limited by the number of GSs available per region, with coverage over the sea being severely crippled; nonetheless, the simulations suggest that the system can still provide coverage, to the south of the country, with 4 GSs or more.

The centre of the region delimited by the GSs is still the best served area with coverage from 5 GSs or more. These results suggest, that despite the coverage loss, the positioning error threshold may still be met inside the interest area. Figure 4.19 provides a numerical comparison of the results in Figure 4.18; in this scenario, and contrasting with the most favourable one, all FLs have similar coverage area. Moreover, the cumulative radio coverage decreases rapidly when the number of GSs decreases, suggesting that accuracy outside the region defined by network is particularly susceptible to the SNR.

Figure 4.20 shows the aircraft RMS positioning error threshold coverage maps for the number of GSs available per region for the error threshold of $\Delta d_{pos\,max} = 150$ m defined by EUROCONTROL. Visual inspection of the results suggests that global system coverage is now limited to aircraft over the land.

Figure 4.21 provides a numerical comparison of the results in Figure 4.20; these findings suggest that with the reduction in expected radio coverage due to the increase in the required fading margins, accuracy is now mostly limited by the number of GSs. In fact, all the analysed FLs show a saturation when the minimum number of available GSs drops below 6, suggesting that at least 6 sensors are required to comply with the accuracy requirements. These findings suggest that accuracy, particularly in demanding radio environments, is highly dependent on the number of GSs available.

Figure 4.22 provides the spatial distribution of the positioning error, the saturation of the error contours is especially evident for FL050, it occurs for areas limited by propagation coverage, and can be thought of as sharp cliffs on the positioning error surface. Remarkably, the region delimited by the GSs still guarantees a positioning error bellow 50 m.
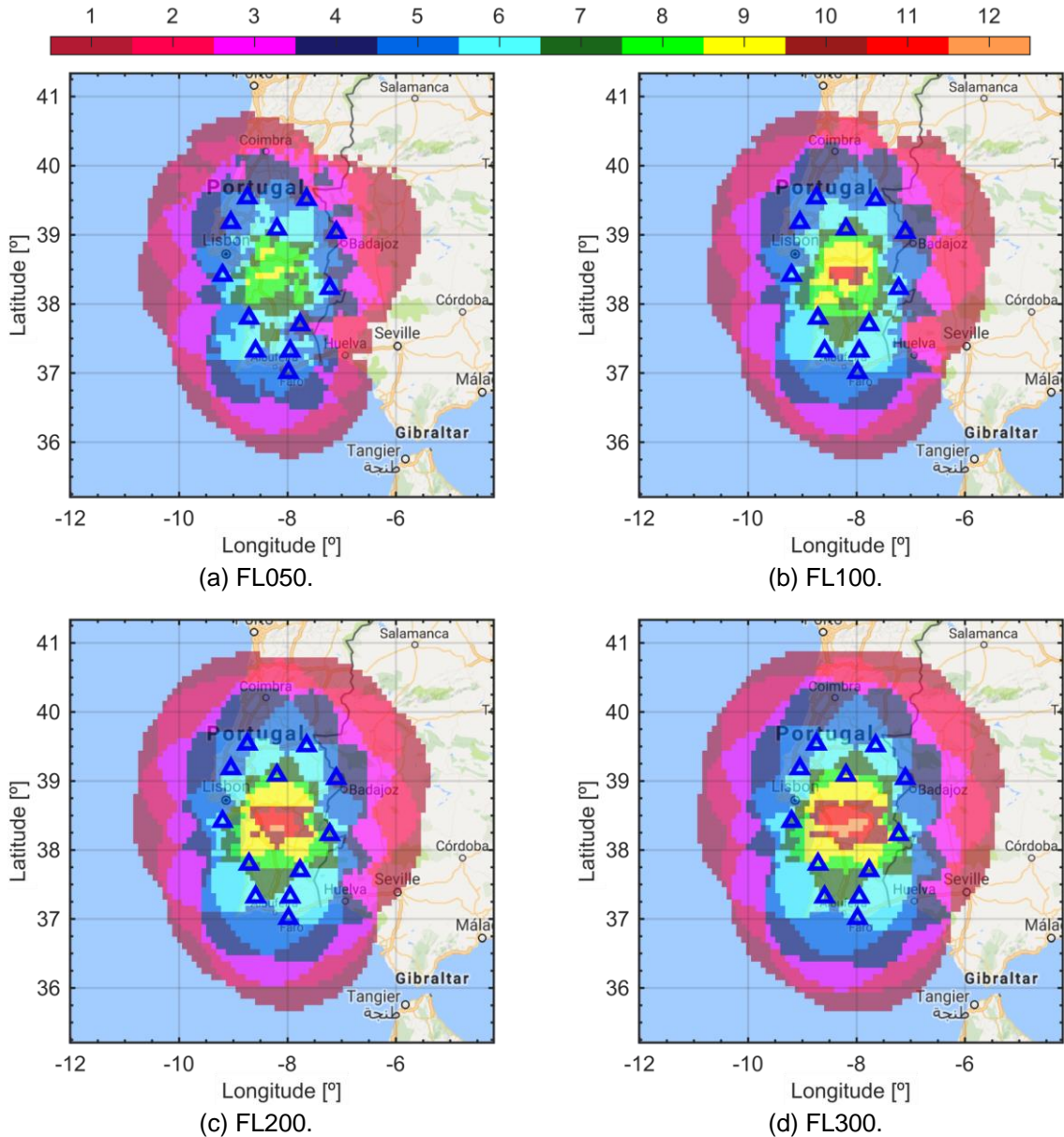
Figure 4.18 – Cumulative coverage maps for the number of GSs ($M_{F\,SF} = 3$ dB, and $M_{F\,FF} = 26$ dB).
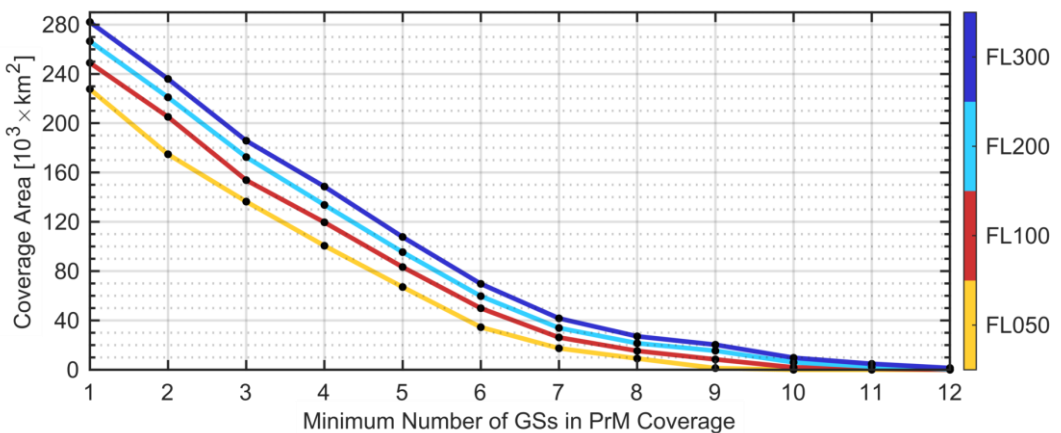
Figure 4.19 – Cumulative coverage area for the number of GSs ($M_{F\,SF} = 3$ dB, and $M_{F\,FF} = 26$ dB).
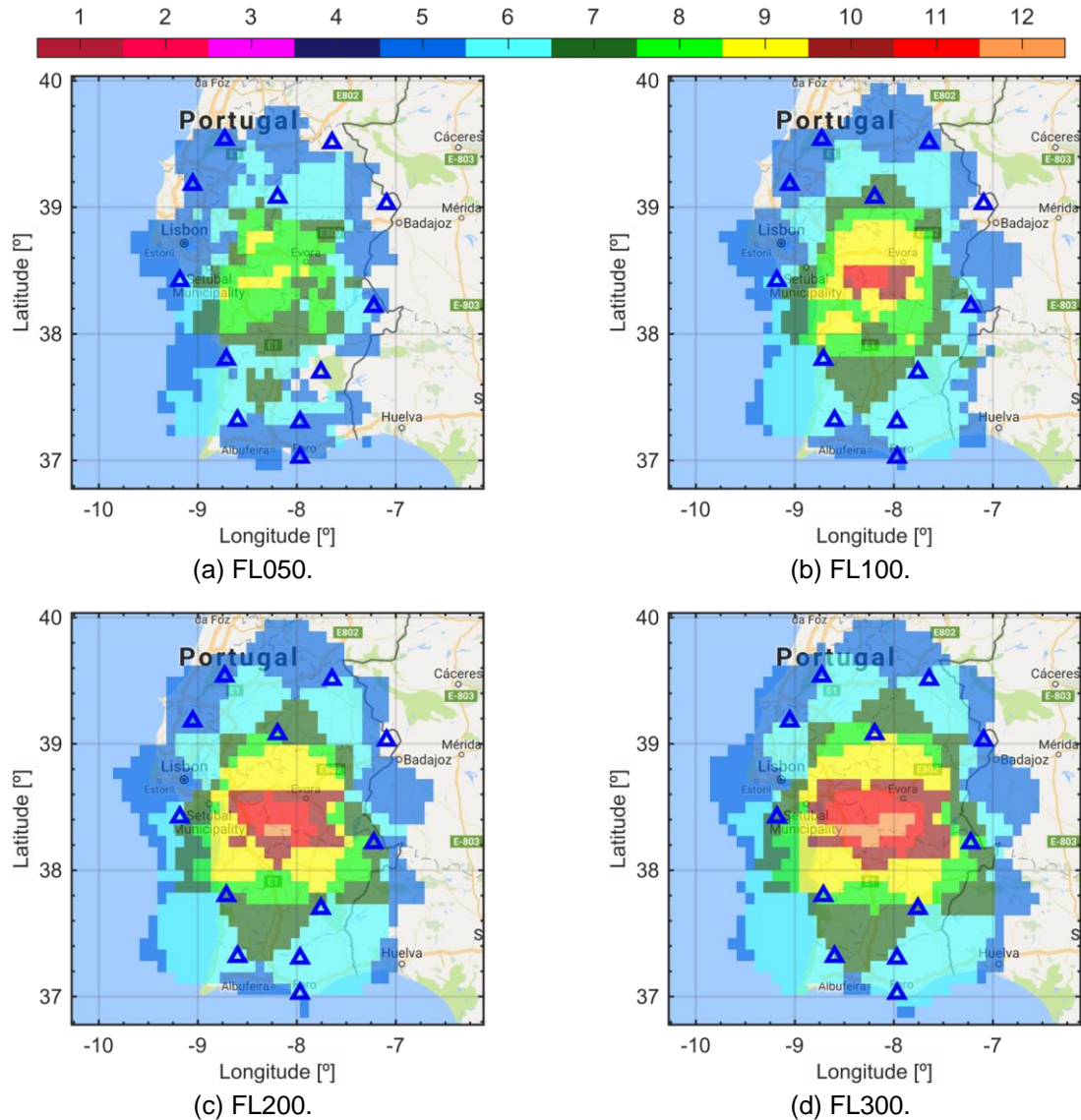
Figure 4.20 – Cumulative coverage maps for the number of GSs, with the limitation introduced by the aircraft RMS positioning error threshold ($\Delta d_{pos\,max} = 150$ m, $M_{F\,SF} = 3$ dB, and $M_{F\,FF} = 26$ dB).
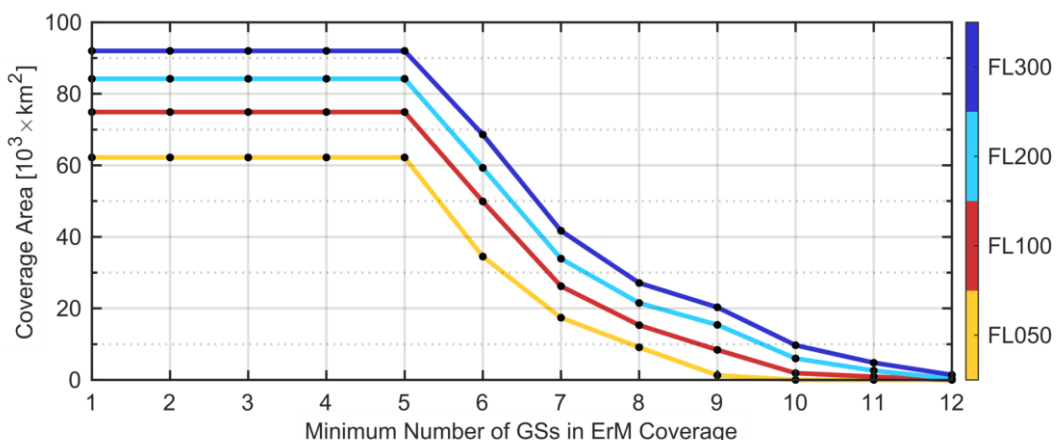
Figure 4.21 – Cumulative coverage area for the number of GSs, with the limitation introduced by the aircraft RMS positioning error threshold ($\Delta d_{pos\,max} = 150$ m, $M_{F\,SF} = 3$ dB, and $M_{F\,FF} = 26$ dB).
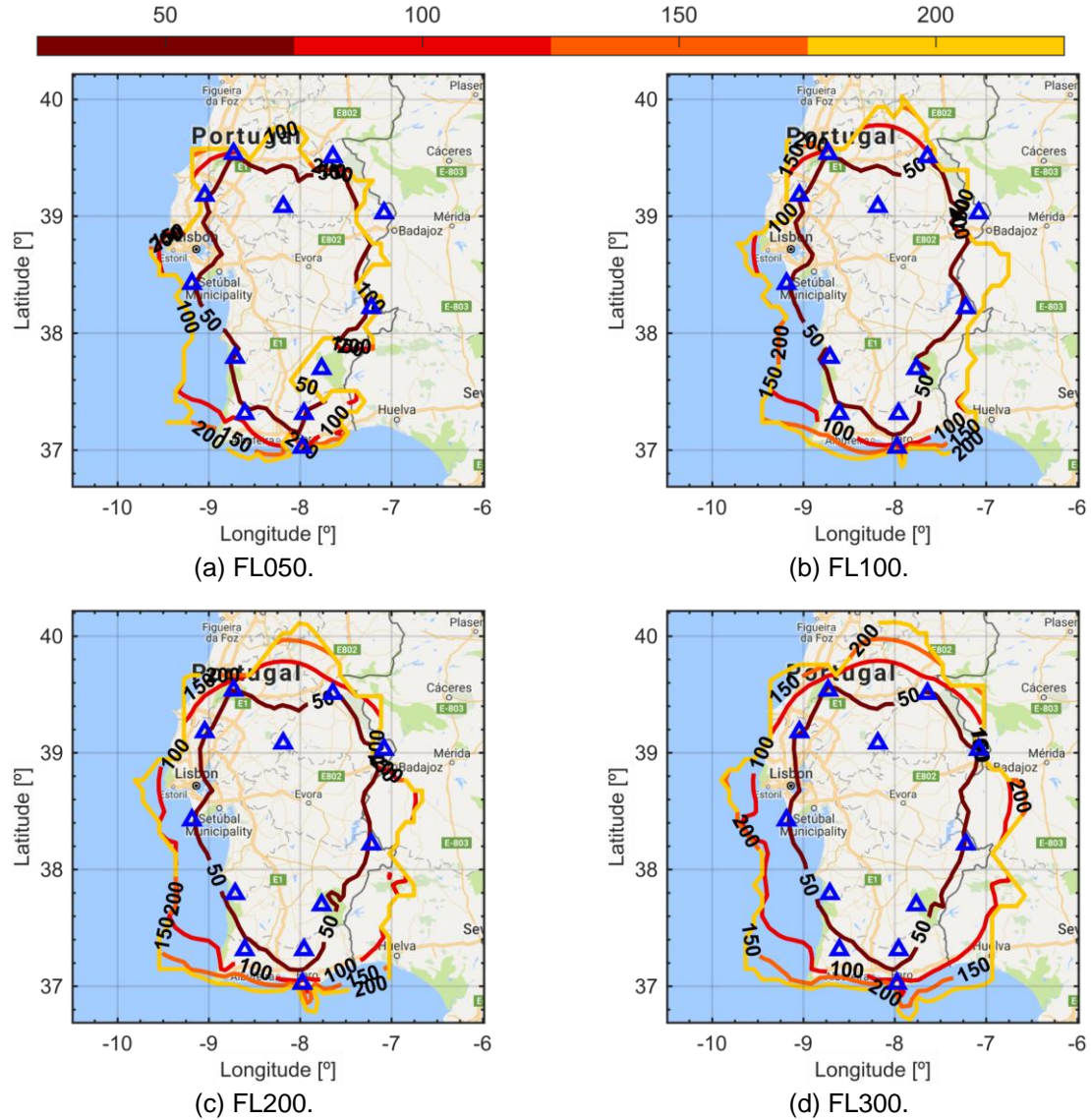
Figure 4.22 – Aircraft RMS positioning error spatial distribution ($M_{F\,SF} = 3$ dB, and $M_{F\,FF} = 26$ dB).

Figure 4.23 provides the statistics of the estimates obtained for the positioning error. In this scenario, accuracy is mostly limited by the number of available GSs; nonetheless, the results suggest that the positioning error statistics have the same intrinsic mechanism as with the most favourable scenario, where the results suggested that accuracy coverage is mostly limited by geometric effects. Inside the region delimited by the GSs, coverage is still guaranteed by 7 or more sensors; moreover, the angle between an aircraft and any pair of GSs is also maximised inside this region; due to these two facts, the error statistics inside this area are similar to the ones obtained for the most favourable scenario.

Table 4.6 provides the descriptive statistics of the results in Figure 4.22. The statistics display a linear trend with the FL, with the minimum observed value showing a slightly decrease with increasing height. The estimates for the shape parameter of the Shifted Exponential Distribution, as a function of FL, are well-approximated by a linear regression with slope parameter of 10.96 m FL^{-1} and intercept parameter of 28.35 m, showing a coefficient of determination value of 97.99%. The estimates for the translation parameter of the Shifted Exponential Distribution, as a function of FL, are reasonably well-approximated

by a linear regression with slope parameter of -1.14 m FL^{-1} and intercept parameter of 33.95 m, showing a coefficient of determination value of 98.16%.

(a) FL050.

(b) FL100.
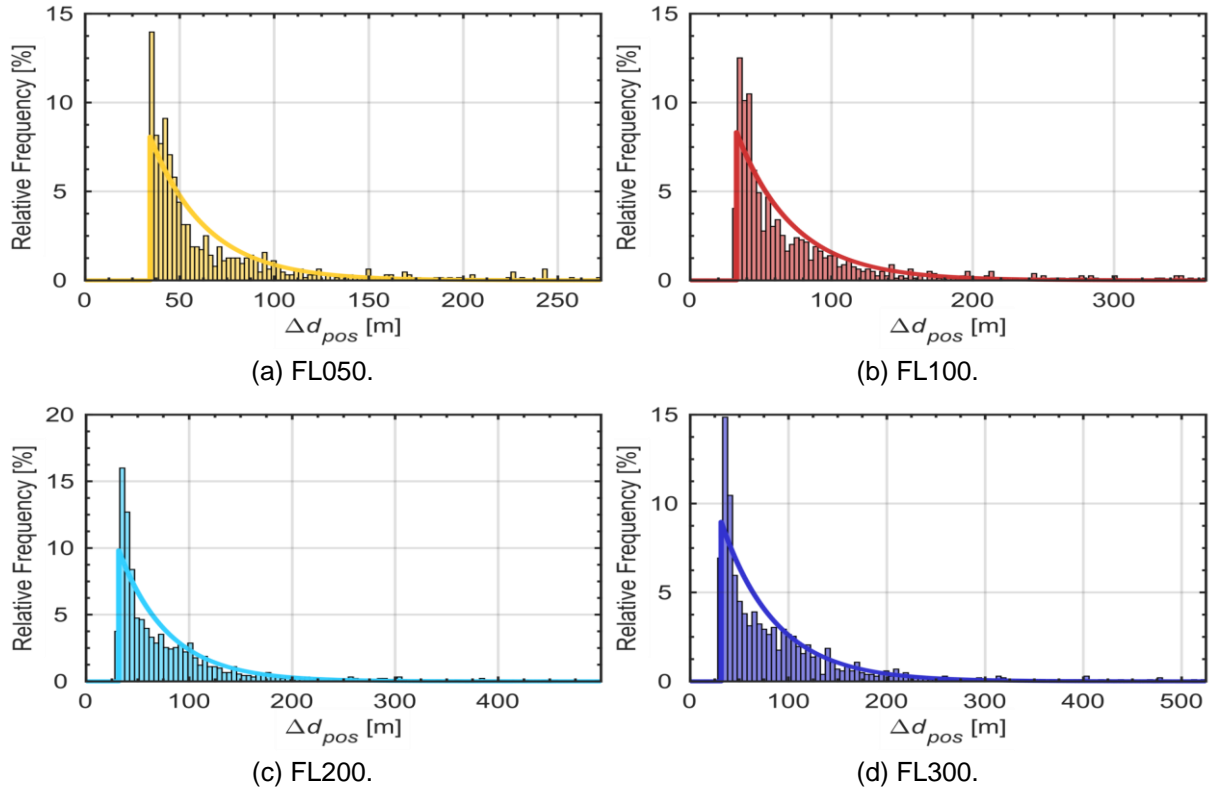
(c) FL200.

(d) FL300.

Figure 4.23 – Aircraft RMS positioning error histogram and fitted distribution
($M_{F\,SF} = 3$ dB, and $M_{F\,FF} = 26$ dB).

Table 4.6 – Aircraft RMS positioning error descriptive and inferential statistics
($M_{F\,SF} = 3$ dB, and $M_{F\,FF} = 26$ dB).

			FL050	FL100	FL200	FL300
Descriptive Statistics	Percentiles	$\Delta d_{pos\,[m]}^{max}$	1217.8	2175.9	2707.0	2082.6
		$\Delta d_{pos\,[m]}^{95\%}$	185.4	249.4	278.5	287.9
		$\Delta d_{pos\,[m]}^{50\%}$	47.7	52.2	55.7	63.3
		$\Delta d_{pos\,[m]}^{min}$	33.0	31.4	30.5	29.5
	Moments	$\Delta d_{pos\,[m]}^{\mu}$	75.0	90.6	103.7	108.0
		$\Delta d_{pos\,[m]}^{\sigma}$	94.2	146.9	194.3	169.5
		$\gamma_{\Delta d_{pos}}^{s}$	6.8	7.6	7.8	6.1
		$\gamma_{\Delta d_{pos}}^{k}$	64.7	80.8	79.6	50.1
Inferential Statistics	Fit	$\widehat{\Delta d}_{pos\,[m]}^{\mu}$	37.5	52.2	62.8	70.5
		$\widehat{\Delta d}_{pos\,[m]}^{\mu_0}$	33.0	31.4	30.5	29.5
	GOF	χ_0^2	202.2	118.5	200.8	211.4
		$\chi_{95\%}^2$	21.0	22.4	22.4	25.0
		$\sqrt{\overline{\varepsilon^2}}_{[\%]}$	1.6	1.3	1.8	1.7
		$R^2{}_{[\%]}$	79.4	88.3	80.7	80.0
		$R_{adj\,[\%]}^2$	75.9	86.5	77.7	77.3

Table 4.7 provides the first order resilience analysis for the position error threshold coverage. The global coverage loss, corresponds to the percent coverage loss considering the shaded shapes presented in Figure 4.13. The interest area coverage loss, corresponds to the percent coverage loss considering the same shaded shapes, but limited to the East, at 7ºW, and to the North, at 39ºN. As seen from the table, removing GSs produces a coverage loss much higher than in the most favourable scenario, due to the crippled radio coverage. Nevertheless, inside the interest area it is still possible to find noncritical GSs. Results suggest that the loss of a GS in more critical for lower FLs; this may be due to geometric effects, since the system coverage does not improve much for higher FLs. Regarding geometry effects, the optimal scenario corresponds to a target forming equilateral triangles with any pair of sensors, the multiplicative effect of the geometry in the accuracy of the system should get worse when the target moves away from this optimal position. The results in Table 4.7 suggest that the optimal point is above the simulated altitudes, moving away from this optimal point causing a degradation in the aircraft location accuracy; hence, lower FLs display worse accuracy, and higher coverage loss when a GS is removed.

Table 4.7 – Resilience analysis percent loss for the aircraft RMS positioning error threshold coverage area for $N_{GS} - 1$ ($\Delta d_{pos\,max} = 150$ m, $M_{F\,SF} = 3$ dB, and $M_{F\,FF} = 26$ dB).

[%]	Global Coverage Loss				Interest Area Coverage Loss			
	FL050	**FL100**	**FL200**	**FL300**	**FL050**	**FL100**	**FL200**	**FL300**
Mon	28.14	26.30	23.52	21.63	25.62	20.12	16.64	13.80
CEs	23.47	17.36	16.39	15.65	23.46	17.80	16.91	16.19
SMo	21.54	18.83	16.75	14.67	18.80	13.75	11.36	9.79
Sai	22.99	19.89	18.05	16.20	20.30	14.91	12.81	11.17
Cer	24.92	12.42	9.86	9.24	25.79	13.31	10.57	9.41
Foi	15.11	7.88	6.41	6.30	15.64	8.39	6.74	5.40
Far	9.65	10.01	11.16	12.61	9.98	10.71	10.83	10.41
CMa	13.99	15.09	14.96	15.00	11.81	8.83	6.87	4.77
Bar	10.77	12.82	13.90	14.57	11.15	12.01	11.62	9.28
Nis	18.65	19.23	17.46	16.09	15.81	12.45	10.04	8.03
Sal	17.20	7.74	7.24	7.17	17.80	8.25	6.34	3.89
Mér	20.10	11.08	11.05	11.20	20.80	10.13	8.45	5.40

The second order resilience analysis, for the position error threshold coverage, reveals that the coverage percent loss is above 20% for all GSs, hence, for this reason the corresponding table of results is not presented here.

Chapter 5

Conclusions

This chapter finalises the thesis, providing the main results from the work. It starts by formulating the addressed problem, after which conclusions from the various chapters are presented. A summary of the developed model is then provided, as well as directions for future work. Finally, the chapter ends with recommendations to optimise future implementations of aeronautical multilateration systems.

This thesis addresses the analysis of performance of aeronautical multilateration systems regarding aircraft location accuracy. A model, considering the major propagation and error components acting in the system, is proposed and implemented in a simulator, allowing to provide estimates for system coverage and accuracy inside a volume, with results being shown on bi-dimensional Mercator projections of the Earth. In what follows, one summarises the five chapters in this thesis.

Chapter 1 provides the motivation and objectives for the work, as well as its structure and organisation. The chapter starts with the current paradigm in aeronautical surveillance, focusing on the economic benefits of the air transportation service, the current democratisation of the industry, and the need to improve airspace capacity through the integration and performance improvement of the CNS interface.

In Chapter 2, the theoretical foundations for the problem under study are analysed. After a brief introduction on surveillance systems for air traffic control, a study of aeronautical multilateration systems is provided, describing the system architecture and function, as well as the main sources of error during aircraft location. Also, the specification parameters for the system are provided, followed by the technical limitations associated with aeronautical multilateration systems. The chapter ends with a state of the art on the modelling and assessment of multilateration systems.

In Chapter 3, a deterministic model for the analysis of aircraft accuracy location in aeronautical multilateration systems is proposed. The chapter starts with a cursory description of the theoretical model, offering an overview of its objectives and assumptions. Subsequently, a more detailed description of the sub-models is provided, followed by the development of the statistical model for the positioning error. Afterwards, the implementation of the developed model is fully described, with detailed flowcharts being shown for the algorithms realised in the simulator. Finally, the chapter ends with a thorough assessment of results by comparison with data from the literature, and from previously implemented systems. Aeronautical multilateration systems enable the locating of an aircraft based on the TDoA of its signal to three or more strategically placed receiver GSs, which are located around an area of interest, providing continuous air traffic surveillance. The aim of this dissertation is to develop a model for the analysis of the performance of aeronautical multilateration systems concerning aircraft location accuracy. The proposed model considers the GSs' location, their antennas radiation patterns, transmitted power, receiver sensitivity, and the corresponding parameters for the aircraft. LoS conditions are assessed, considering a Digital Elevation Model, Fresnel's Ellipsoid Model, and the Effective Earth's Radius Model. The Free-Space Path Loss Model is used, with fading margins being set to model the power oscillations due to multipath and the aircraft orientation uncertainty. Aircraft accuracy location is estimated from the system's GDoP, considering the error components due to tropospheric delay, multipath, receiver noise, quantisation, and clock bias. The model was implemented in a simulator and successfully validated, with results from the model displaying good agreement with data from the literature and previously implemented systems.

In Chapter 4, one provides the description of the scenarios for the performance analysis, and the analysis of solutions and of their implementation. The chapter starts with the description of the simulation parameters for the scenarios under study. Then, an analysis of results from the model for a set of canonical scenarios found in the literature is provided. The chapter ends with the results from the model

for the scenarios under study. The developed model is employed in the analysis of an implemented system from NAV Portugal, with results suggesting that the system has a good degree of redundancy, displaying negligible reductions in coverage of as low as 2%, when two out of twelve GSs are removed. Statistical analysis suggests that the positioning error can be modelled by a Shifted Exponential Distribution, with parameters proportional to the aircraft's altitude.

This thesis provides a model for the analysis of performance of aeronautical multilateration systems concerning aircraft location accuracy, and a simulator to implement it. The devised model combines two elements otherwise independent: a propagation model, and an error model. The propagation model accounts for the typical losses of the aeronautical communication channel, providing a step forward in the modelling of the shadowing caused by the aircraft structure. This information is used to feed the error model, considering the viable links between the aircraft and each GS, the GSs' detectors' accuracy, and the typical geometric effects of the localisation scenario. The propagation and error models are, individually and jointly, validated against available data from NAV and the literature.

A demonstration of the model capabilities is also provided by an analysis of a solution owned by NAV in the south of mainland Portugal. The demonstration analysis indicates that the implemented system can provide surveillance coverage, inside the defined interest volume, with a positioning RMSE lower than the regulatory threshold of 150 m. As a supplement, the model is used for reliability analysis of the system owned by NAV, with results indicating that certain GSs are not critical to system performance, a fact that is of the most importance for resource management during GS failure or malfunction.

The findings in this thesis suggest that system performance decays abruptly outside the region defined by the network; therefore, future implementations are recommended to have a baseline distance between GSs as high as possible, without reducing cumulative radio coverage; additionally, GSs at higher altitudes, by providing higher radio coverage, are more important to the system overall coverage in terms of accuracy and propagation conditions. The uniformity of the network is also advised, considering the possible GSs sites, baselines should be as uniform as possible. These parameters can only be fully assessed by numerical simulation of the system; therefore, the use of the model provided in this thesis is recommended.

It is worth noting that the propagation model can be improved with the implementation of diffraction propagation models to better understand the system behaviour in NLoS conditions. Also, co-channel interference should be assessed, since more than one aircraft can be transmitting in a given instant; a statistical characterisation for this effect is advised. The model can also be improved by merging it with existing models for the delay analysis [47], interference due to wind turbine generators, [49] and [48], and interference due to RF sources outside aeronautical telecommunications [50]. The simulator can be programmed to be a general-purpose tool for the assessment of the aeronautical CNS infrastructure, since much of the geometry, propagation and error algorithms are already implemented.

The model for the error component due to noise and signal bandwidth in the ToA estimation is shared with many other systems, such as the PSR and the SSR, and NAVAID technologies, such as the DME. The model for GDoP can also be adapted to assess accuracy in emergent surveillance systems, such as the MSPSR.

Annex A

Vendor technical specifications

Technical specifications of the aeronautical multilateration systems from specialised vendors.

Table A.1 – Vendor 1, system technical specifications (extracted from [90]).

Input data	Mode A/C
	Mode S (DF 0, 11, 4, 5, 16, 17, 20, 21)
Output data	ASTERIX Cat 19/20/21
Capacity	500 targets (Mode S)
Maximum latency	250ms (surface movement)
	500ms (wide area)
Accuracy	Up to 5m horizontal
	Up to 10m vertical
Coverage	System extendable to coverage required
Update rate	Configurable

Table A.2 – Vendor 2, system technical specifications (extracted from [91]).

Input data	Receives 1090MHz, Mode A/C
	Mode S (DF 0, 4, 5, 11, 16, 17, 18, 20, 21)
Target report data	ASTERIX 20, 21
CMS interfaces	SNMP V3
Capacity	400 Mode S targets, 100 mode A/C
Maximum latency	500ms
Accuracy (tested in existing deployments)	Horizontal error better than 50m std deviation
	Vertical error < 10m
Coverage	Extendable to required.
Update rate	Data driven or periodic mode
	(reporting period configurable)

Table A.3 – Vendor 2, receiver technical specifications (extracted from [91]).

Bandwidth	≥ 20 MHz
Sensitivity	-90 dBm
Dynamic Range	75 dB
ToA error	< 1ns
Power consumption	< 100W
Operating temp.	from -40ºC to +55ºC
Humidity	from 5% to 100%
Ingress protection	IP66
MTBF	> 40.000 h
MTTR	< 30 minutes

Table A.4 – Vendor 2, transmitter technical specifications (extracted from [91]).

Interrogation modes	1030MHz, modes 1, 2, 3/A, C and Mode S
Peak power	≥ 53 dBm
Spurious radiations	≤ -76 dBW
Antenna	Sector or Omni-directional
	Gain variable according to coverage needs.
Power consumption	≤ 100 W (TBC)
Operating temp.	-40º a +55º
Humidity	0 - 95%
Ingress protection	IP67
MTBF	>40.000 h
MTTR	< 30 minutes

Table A.5 – Vendor 3, system technical specifications (extracted from [92]).

Transponder Types	Mode S, (ELS/EHS), Mode S ES, Mode A/C
RMS Position Error (accuracy)	surface: < 5 m, airborne: < 30 m
Target Capacity	750 targets
Track Initiation	5 seconds max
Target Update Rate	1–12 seconds (Adaptable)
Probability of Detection	>97%
System Latency	250 ms
SSR Interrogation	ICAO Annex 10 compliant
Data Output Format	ASTERIX CAT 010, 011, 20, 48, CD2 (MLAT), ASTERIX CAT 21 (ADS-B), ASTERIX 19, 23, 34 (Status)

Annex B

Summary of basic
system characteristics

Technical specifications of the aeronautical multilateration systems from specialised vendors.

For convenience, the basic system characteristics are summarised bellow,
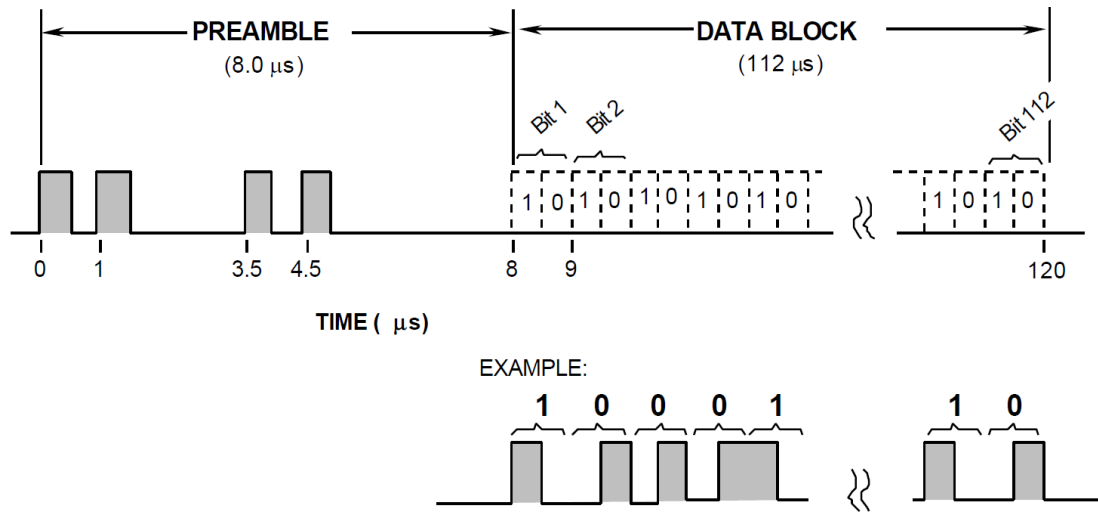
Figure B.1 – Signal structure (adapted from [87]).

Table B.1 – System characteristics (adapted from [87]).

Frequency band	1090 MHz	
Channels	one channel	
Bit rate	1 Mb/s	
Modulation	PPM	
Synchronisation	4 pulse preamble	
Message length	112 bit	
Parity Check	24 bit	
Aircraft Address	24 bit	
Longitude	CPR, LSB ~ 5 meters	
	17 bit even, 17 bit odd	
PVT segmentation	velocity in separate message	
Transmitter power (at antenna)	51-57 dBm, normal	
	48.5-57 dBm, low-end	
Receiver Minimum Triggering Level MTL (90%) (at antenna)	<= -84 dBm, high-end	
	<= -72 dBm, low-end	
Polarisation	vertical	
Transmission rate, PVT	2 per sec. position	
	2 per sec. velocity	
Multiple access technique	random short messages	

Annex C

Positioning error assessment with Monte Carlo method

An empirical model for the positioning error is proposed, this model is used to validate the deterministic model used in this thesis.

Taking the nonlinear TDoA measurement model, as defined in [65], it is possible to define a system of nonlinear equations to be solved stochastically, using an nonlinear equation solver. Stochastic simulations provide a way to estimate the true value of a given quantity by sampling an infinite population. When performing stochastic simulations, one should keep in mind that the convergence of the procedure to the true value of the quantity being measured, vastly depends on the number of trials. The number of times that the stochastic model should be run can be related with a precision metric.

Given an aircraft coordinate is space, it is possible to solve the multilateration equations several times, measuring the overall standard deviation of the results. Considering that the expected value is known, the degrees of freedom are equal to the number of samples withdrawn through stochastic simulation; moreover, the sample variance estimator is written without Bessel's correction,

$$s_{\mu_0}^2 = \frac{1}{N_{MC}} \sum_{i=1}^{N_{MC}} (X_i - \mu_0)^2 \tag{C.1}$$

where:

- N_{MC}: number of Monte Carlo simulations,
- X_i: i^{th} sample,
- μ_0: expected value of X.

The width of the confidence interval for the variance of a normal population, normalised to the sample variance is defined as,

$$w_{\sigma^2}^{p\%} = \frac{N_{MC}}{\chi_{1-\alpha/2,N_{MC}}^2} - \frac{N_{MC}}{\chi_{\alpha/2,N_{MC}}^2} \tag{C.2}$$

where:

- $p\%$: confidence level,
- N_{MC}: number of runs for the Monte Carlo simulations,
- α: confidence interval variable.

Figure C.1 shows the number of required simulations to achieve a given confidence interval of the accuracy estimate, for the variance of a normal population at the 90%, 95% and 99% confidence level.
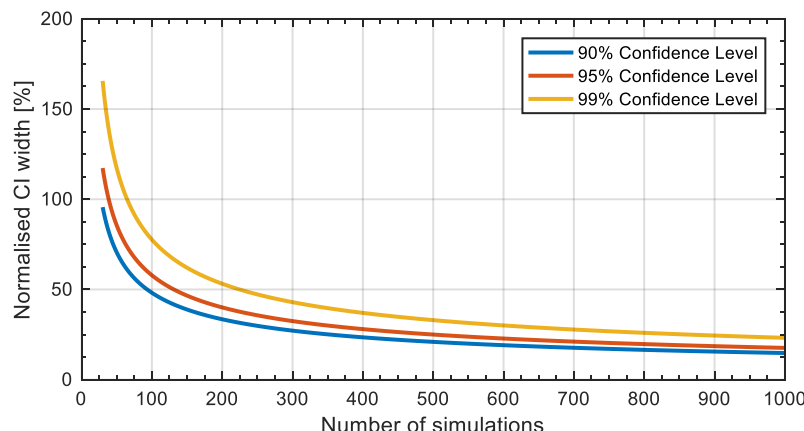
Figure C.1 – Required number of simulations for the normalised width of the confidence interval.

Annex D

Results for radio coverage analysis

This annex provides the results for the radio coverage analysis of the Faro WAM system. The individual coverage of each of the twelve GSs of the Faro WAM are displayed, at the four considered FLs, and for the two availability scenarios considered.
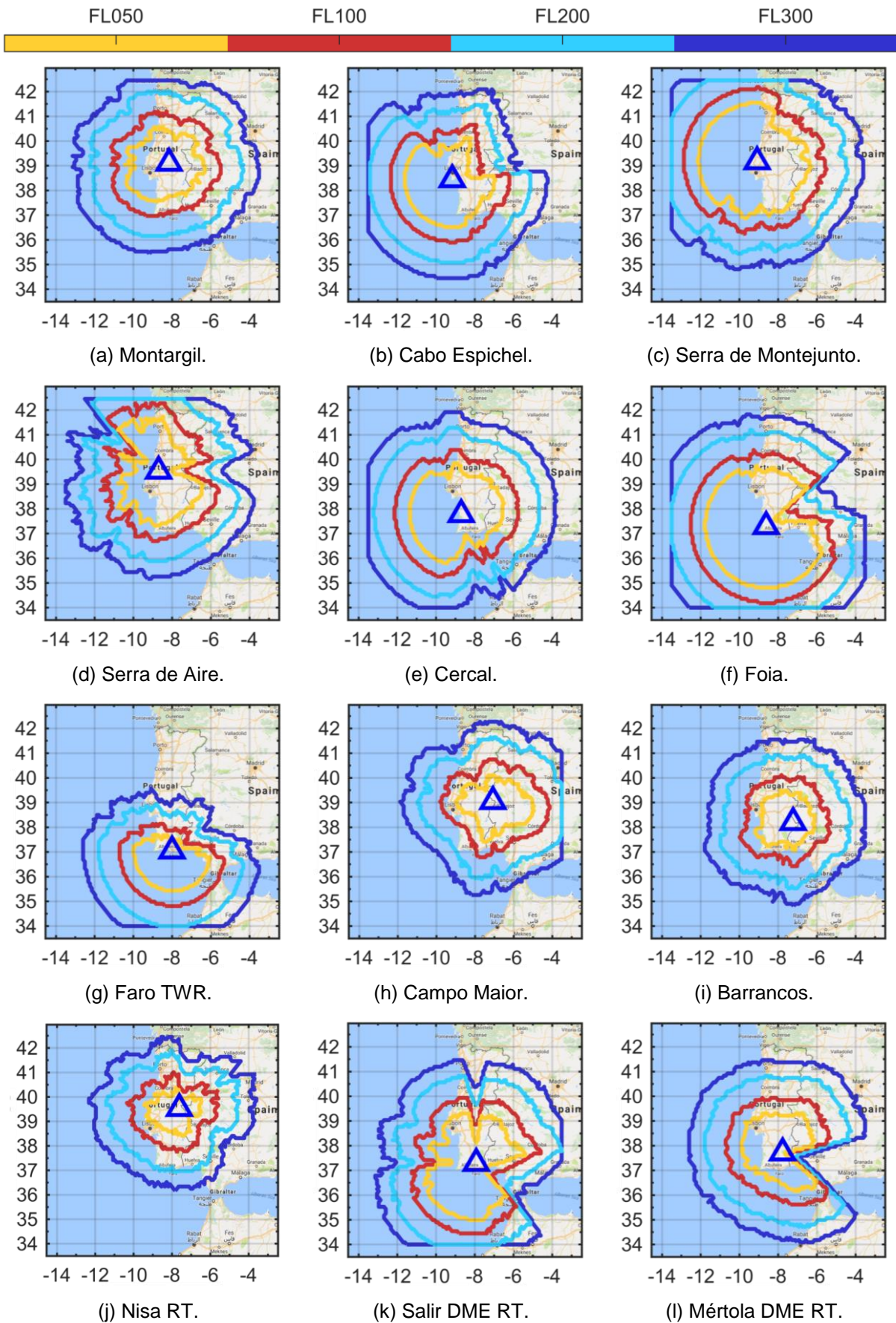
Figure D.1 – Propagation coverage maps for each GS ($M_{F\ SF} = 0$ dB, and $M_{F\ FF} = 0$ dB).
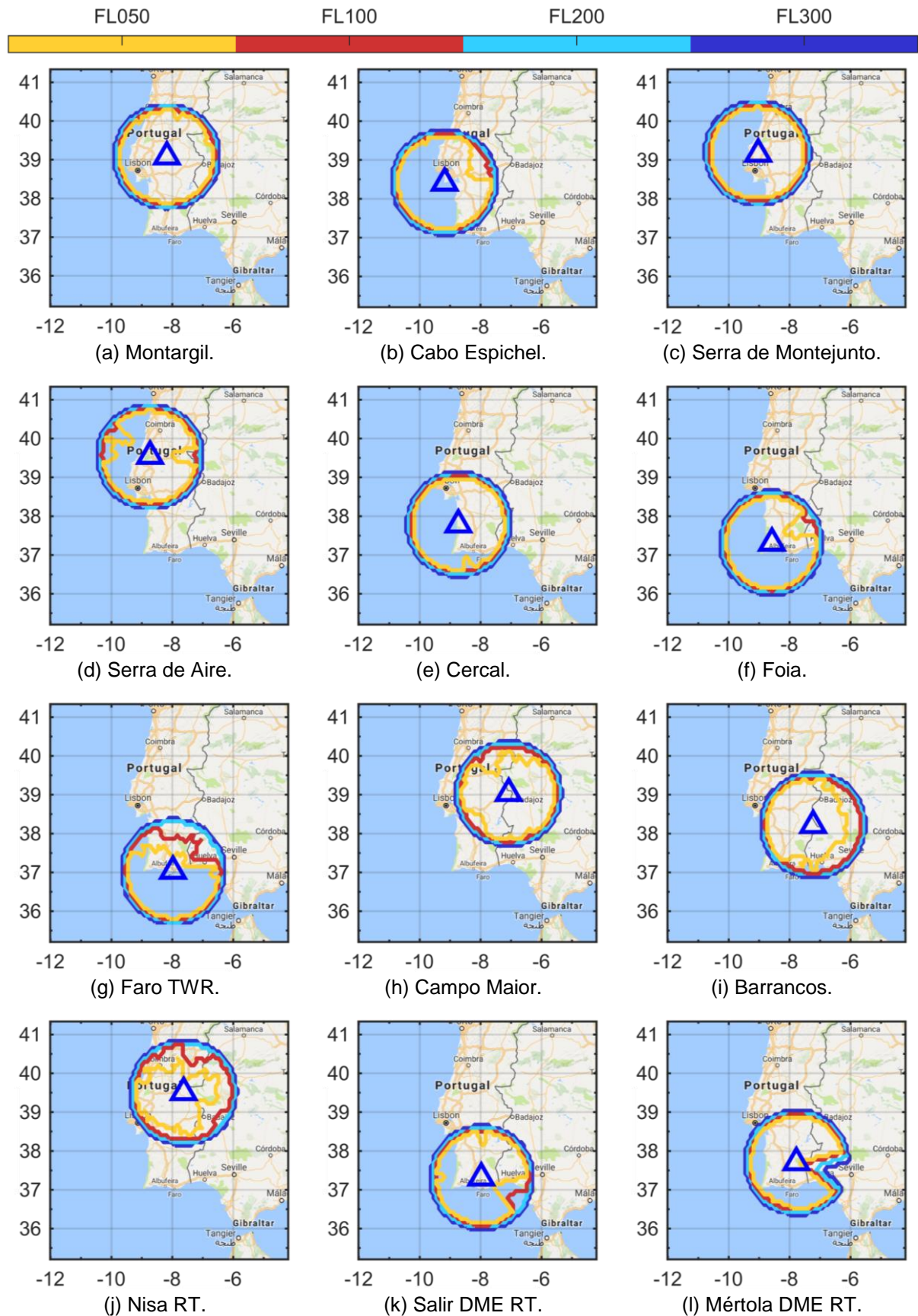
Figure D.2 – Propagation coverage maps for each GS ($M_{F\,SF} = 3$ dB, and $M_{F\,FF} = 26$ dB).

Annex E

Results for resilience analysis

This annex provides the results for the resilience analysis of the Faro WAM system due to loss of two GSs. The simulations where obtained for different flight levels in order to assess their impact.

The following Tables provide the percent loss in coverage area when two GSs are removed from the Faro WAM system described in Section 4.1. The simulations where conducted for four aircraft flight levels: $FL050$ (1524 m), $FL100$ (3048 m), $FL200$ (6096 m), and $FL300$ (9144 m). The simulation procedure comprised the coverage assessment of the system for a nominal scenario with all the GSs available, establishing the coverage area of the system considering its radio and accuracy performance. Then, the simulation process was repeated for all the 66 possible GS failure scenarios, considering the combinations of 2 out of the 12 GSs present in the system. Finally, the coverage area for each failure scenario was compared with the nominal coverage area, and the percent coverage loss computed. The percent coverage loss is provided for the global and interest coverage areas of the system.

Table E.1 – Resilience analysis percent loss for the aircraft RMS positioning error threshold coverage area for $N_{GS} - 2$ ($\Delta d_{pos\,max} = 150$ m, $M_{F\,SF} = 0$ dB, and $M_{F\,FF} = 0$ dB).

| [%]	Global Coverage Loss				Interest Area Coverage Loss			
	FL050	FL100	FL200	FL300	FL050	FL100	FL200	FL300
Mon, CEs	13.73	8.84	6.87	9.44	12.09	7.66	3.59	4.22
Mon, SMo	15.88	7.19	7.22	9.57	13.15	6.11	5.38	6.51
Mon, SAi	12.88	9.09	11.80	14.26	10.55	6.94	9.07	10.45
Mon, Cer	17.92	5.21	5.65	6.69	14.45	3.62	3.87	3.57
Mon, Foi	19.31	7.44	8.94	10.04	18.25	7.35	7.46	6.87
Mon, Far	12.45	9.17	12.88	16.40	11.14	9.83	11.80	13.29
Mon, CMa	12.12	10.83	9.08	11.38	5.69	2.07	3.12	4.40
Mon, Bar	9.66	4.38	9.08	9.30	5.33	2.59	8.12	6.78
Mon, Nis	7.40	5.12	10.16	12.45	4.62	2.07	3.97	4.58
Mon, Sal	11.37	8.43	9.01	9.30	7.23	3.83	4.72	4.58
Mon, Mér	12.77	4.13	5.36	7.03	8.77	2.59	3.02	3.30
CEs, SMo	16.52	13.39	12.09	14.32	14.81	10.35	7.46	8.71
CEs, SAi	14.06	14.13	14.38	17.34	12.32	11.18	10.20	11.82
CEs, Cer	17.92	8.84	8.73	10.78	16.23	7.45	5.38	4.86
CEs, Foi	15.34	10.91	12.59	13.86	16.23	10.46	9.92	9.44
CEs, Far	11.80	13.72	15.31	19.88	12.32	13.98	13.13	14.57
CEs, CMa	14.06	15.54	13.09	14.99	8.89	6.94	4.72	5.77
CEs, Bar	12.12	10.17	13.09	15.06	9.95	7.45	9.82	9.72
CEs, Nis	9.23	9.59	12.23	14.26	7.46	6.42	4.53	5.50
CEs, Sal	13.73	12.07	11.52	12.58	11.49	7.45	6.23	6.14
CEs, Mér	13.73	8.60	8.01	10.24	11.73	7.04	4.25	4.58
SMo, SAi	21.03	17.69	18.96	21.29	19.08	14.08	15.68	17.42
SMo, Cer	19.31	9.01	8.73	10.44	16.00	6.83	6.52	7.15
SMo, Foi	20.06	11.82	12.09	13.86	19.31	10.77	10.10	10.72
SMo, Far	14.16	13.22	16.02	20.08	13.27	13.25	14.16	16.50

Table E.1 (contd.) – Resilience analysis percent loss for the aircraft RMS positioning error threshold coverage area for $N_{GS} - 2$ ($\Delta d_{pos\,max} = 150$ m, $M_{F\,SF} = 0$ dB, and $M_{F\,FF} = 0$ dB).

SMo, CMa	14.59	14.05	11.23	13.65	8.77	5.69	5.48	7.06
SMo, Bar	12.55	8.76	11.52	13.19	8.77	6.31	10.01	11.00
SMo, Nis	10.73	9.42	12.88	16.13	7.94	5.69	6.80	8.80
SMo, Sal	14.81	13.14	11.95	13.19	10.90	7.14	7.08	8.52
SMo, Mér	15.13	9.09	8.01	10.31	11.61	7.14	5.48	6.78
SAi, Cer	17.70	10.91	11.95	14.06	14.45	8.18	8.97	10.27
SAi, Foi	17.60	12.89	15.02	17.07	16.82	10.97	12.46	13.38
SAi, Far	14.70	15.95	20.03	23.63	14.10	15.22	17.75	19.52
SAi, CMa	15.56	17.02	16.02	18.54	9.24	7.76	9.35	11.37
SAi, Bar	12.55	10.83	14.81	16.73	8.77	8.28	12.84	14.02
SAi, Nis	11.70	14.46	19.46	22.62	9.24	9.21	12.28	14.21
SAi, Sal	13.95	14.30	15.59	16.40	10.19	8.49	10.20	11.09
SAi, Mér	14.06	10.99	12.09	14.39	10.43	8.18	8.78	10.08
Cer, Foi	19.74	9.34	11.59	12.05	19.31	9.01	10.20	8.89
Cer, Far	14.59	10.33	14.38	17.20	13.63	10.77	13.31	14.12
Cer, CMa	13.95	12.40	9.94	11.51	8.41	3.73	4.25	5.22
Cer, Bar	10.84	7.69	11.37	9.44	8.89	6.52	10.86	6.51
Cer, Nis	11.37	7.69	11.16	12.99	7.82	3.73	4.63	5.13
Cer, Sal	13.95	10.08	10.87	10.51	12.20	5.18	6.52	5.50
Cer, Mér	15.99	5.54	6.58	7.50	14.57	3.93	4.25	3.76
Foi, Far	15.99	15.79	20.24	24.30	17.65	17.70	19.74	21.91
Foi, CMa	16.20	14.13	14.02	15.06	12.20	6.83	8.31	8.71
Foi, Bar	12.55	9.17	11.66	12.58	11.14	8.18	10.39	9.62
Foi, Nis	12.98	9.26	14.09	15.33	11.61	6.52	8.12	8.34
Foi, Sal	18.03	14.79	14.95	14.12	16.94	11.39	10.39	10.17
Foi, Mér	15.13	8.60	9.87	11.11	13.98	7.76	7.93	7.33
Far, CMa	13.52	16.28	17.81	21.62	9.72	9.83	12.46	15.03
Far, Bar	11.80	10.66	15.88	18.88	10.31	10.66	14.92	15.67
Far, Nis	10.09	11.49	18.88	22.69	8.89	9.52	13.03	14.48
Far, Sal	13.73	15.37	19.74	22.76	12.20	12.22	15.49	17.05
Far, Mér	11.16	10.00	13.73	17.40	9.60	9.52	11.99	13.29
CMa, Bar	8.91	13.39	14.02	15.73	4.38	3.73	8.50	9.53
CMa, Nis	10.09	13.39	18.53	20.35	3.44	1.66	4.25	5.96
CMa, Sal	10.41	14.46	14.38	14.19	5.09	4.76	5.48	6.23
CMa, Mér	10.19	11.40	10.23	11.91	5.21	2.17	3.68	4.77
Bar, Nis	7.30	6.69	13.88	14.73	3.08	2.07	8.03	7.24
Bar, Sal	8.48	9.92	12.66	12.18	5.69	4.24	8.31	7.33

Table E.1 (contd.) – Resilience analysis percent loss for the aircraft RMS positioning error threshold coverage area for $N_{GS} - 2$ ($\Delta d_{pos\,max} = 150$ m, $M_{F\,SF} = 0$ dB, and $M_{F\,FF} = 0$ dB).

Bar, Mér	8.37	5.21	9.73	10.11	5.57	2.17	7.55	6.32
Nis, Sal	9.23	11.16	14.23	14.73	4.98	3.83	5.57	6.05
Nis, Mér	8.15	6.20	11.02	12.65	4.03	2.07	4.25	4.67
Sal, Mér	11.48	10.58	11.16	10.58	8.89	3.83	5.19	5.22

References

[1] ATAG, *Aviation: Benefits Beyond Borders*, 2016 Global Summary, ATAG, Geneva, Switzerland, Jul. 2016 (http://aviationbenefits.org/media/149668/abbb2016_full_a4_web.pdf).

[2] FAA, *The Economic Impact of Civil Aviation on the U.S. Economy*, FAA, Washington DC, USA, Nov. 2016 (https://www.faa.gov/air_traffic/publications/media/2016-economic-impact-report_FINAL.pdf).

[3] Oxford Economics, *The Importance of Air Transport to Portugal*, Oxford Economics, London, UK, Dec. 2016 (http://www.iata.org/policy/Documents/benefits-of-aviation-portugal-2017.pdf).

[4] Oxford Economics, *Economic Benefits from Air Transport in Portugal*, Portugal country report v1.3, Oxford Economics, Oxford, UK, 2011 (https://www.iata.org/policy/Documents/Benefits-of-Aviation-Portugal-2011.pdf).

[5] EUROCONTROL, *Guidelines for the Application of the ECAC Radar Separation Minima*, EATCHIP Project, Deliverable ASM.ET1.ST18.1000-REP-01.00, Brussels, Belgium, Dec. 1998 (http://www.eurocontrol.int/sites/default/files/publication/content/documents/nm/ecac_radar_sep_min.pdf).

[6] EUROCONTROL, *EUROCONTROL Specification for ATM Surveillance System Performance (Volume 1)*, EUROCONTROL Specification, Deliverable EUROCONTROL-SPEC-0147, EUROCONTROL, Brussels, Belgium, Sep. 2015 (http://www.eurocontrol.int/publications/atm-surveillance-system-performance-esassp-specification).

[7] Era Systems Corporation, *Multilateration - Executive Reference Guide*, Era Systems Corporation, Pardubice, Czech Republic, (http://www.multilateration.com/downloads/MLAT-ADS-B-Reference-Guide.pdf).

[8] N. Xu, R. Cassell, C. Evers, S. Hauswald, and W. Langhans, "Performance assessment of Multilateration Systems - a solution to nextgen surveillance," in *Proc. of ICNS'10 - 10th IEEE Integrated Communications, Navigation and Surveillance Conference*, Herndon, VA, USA, May 2010 (http://ieeexplore.ieee.org/stamp/stamp.jsp?tp=&arnumber=5503290).

[9] NAV Portugal, Mission, https://www.nav.pt/nav/quem-somos, Jan. 2016.

[10] ICAO, *Guidance Material on Comparison of Surveillance Technologies (GMST)*, ICAO, ICAO, Montreal, Canada, Sep. 2007 (http://www.icao.int/APAC/Documents/edocs/cns/gmst_technology.pdf).

[11] W.H.L. Neven, T.J. Quilter, R. Weedon, and R.A. Hogendoorn, *Report on Wide Area Multilateration*, Report on EATMP TRS 131/04, Deliverable NLR-CR-2004-472, EUROCONTROL, Brussels, Belgium, Aug. 2005 (https://www.eurocontrol.int/sites/default/files/publication/files/surveilllance-report-wide-area-multilateration-200508.pdf).

[12] F.X. Salambanga, *MULTILATERATION & MAGS*, ICAO, Montreal, Canada, Apr. 2014 (www.icao.int/WACAF/Documents/Meetings/2014/Interconnexion of ASS/WP05 Mlat.pdf).

[13] M.I. Skolnik, *Radar Handbook*, 3rd Edition, McGraw-Hill, New York, NY, USA, 2008.

[14] Range Commanders Council, *Error Sources Applicable to Precison Trajectory Radar Calibration*, Document 255-80, AD-A091654, Jan. 1980 (http://www.dtic.mil/dtic/tr/fulltext/u2/a091654.pdf).

[15] ICAO, *Manual on the Secondary Surveillance Radar (SSR) Systems (Doc 9684)*, ICAO Document 9684-AN/951, ICAO, Montreal, Quebec, Canada, 2004.

[16]   NTIA, *960-1164 MHz*, NTIA, Washington, DC, USA, Mar. 2014 (https://www.ntia.doc.gov/files/ntia/publications/compendium/0960.00-1164.00_01MAR14.pdf).

[17]   ICAO, *Annex 10 — Aeronautical Telecommunications: Volume IV — Surveillance and Collision Avoidance Systems*, 5th Edition, International Standards and Recommended Practices, ICAO, Montréal, Quebec, Canada, Jul. 2014.

[18]   K. Pourvoyeur, A. Mathias, and R. Heidger, "Investigation of Measurement Characteristics of MLAT / WAM and ADS-B," in *Proc. of TIWDC/ESAV'11 - 22nd IEEE Tyrrhenian International Workshop on Digital Communications - Enhanced Surveillance of Aircraft and Vehicles*, Capri, Italy, Sep. 2011 (http://ieeexplore.ieee.org/stamp/stamp.jsp?tp=&arnumber=6060989).

[19]   Y. Trofimova, "Multilateration Error Investigation and Classification. Error Estimation," *Transport and Telecommunication*, Vol. 8, No. 2, 2007, pp. 28–37 (http://www.tsi.lv/sites/default/files/editor/science/Research_journals/Tr_Tel/V2/4.pdf).

[20]   S.A.R. Zekavat and R.M. Buehrer, *Handbook of Position Location: Theory, Practice and Advances*, Wiley-IEEE Press, 2011.

[21]   A. Jasch, T. Feuerle, G. Scoor, and P. Hecker, "Geometrical siting considerations for wide area multilateration systems," in *Proc. of PLANS'10 - 3rd Biennial IEEE/ION Position Location and Navigation Symposium*, Indian Wells, CA, USA, May 2010 (http://ieeexplore.ieee.org/lpdocs/epic03/wrapper.htm?arnumber=5507349).

[22]   J.M. Abbud, G. de Miguel, and J. Besada, "Correction of systematic errors in Wide Area Multilateration," in *Proc. of TIWDC/ESAV'11 - 22nd IEEE Tyrrhenian International Workshop on Digital Communications - Enhanced Surveillance of Aircraft and Vehicles*, Capri, Italy, Sep. 2011.

[23]   G.D.M. Vela, J.B. Portas, and J.G. Herrero, "Correction of propagation errors in Wide Area Multilateration systems," in *Proc. of EuRAD'09 - 6th IEEE European Radar Conference*, Rome, Italy, Oct. 2009 (http://ieeexplore.ieee.org/stamp/stamp.jsp?tp=&arnumber=5307004).

[24]   I.A.M. Gaviria, *New Strategies to Improve Multilateration Systems in the Air Traffic Control*, Ph.D. Thesis, Universitat Politècnica de València, Valencia, Spain, 2013 (http://hdl.handle.net/10251/29688).

[25]   S. Gezici and H.V. Poor, "Position Estimation via Ultra-Wideband Signals," *Proceedings of the IEEE - Special Issue on UWB Technology and Emerging Applications*, Vol. 97, No. 2, Feb. 2009, pp. 386–403 (http://ieeexplore.ieee.org/lpdocs/epic03/wrapper.htm?arnumber=4796279).

[26]   H.I. Ahmed, P. Wei, I. Memon, Y. Du, and W. Xie, "Estimation of Time Difference of Arrival (TDOA) for the Source Radiates BPSK Signal," *International Journal of Computer Science Issues (IJCSI)*, Vol. 10, No. 3, May 2013, pp. 164–171 (http://ijcsi.org/papers/IJCSI-10-3-2-164-171.pdf).

[27]   R.A. Hogendoorn, C. Rekkas, and W.H.L. Neven, "ARTAS: An IMM-based Multisensor Tracker," in *Proc. of FUSION'99 - 2nd IEEE International Conference on Information Fusion*, Sunnyvale, CA, USA, Jul. 1999 (http://fusion.isif.org/proceedings/fusion99CD/C-131.pdf?).

[28]   J.L. Gertz and A.D. Kaminsky, *COTS Fusion Tracker Evaluation*, Project Report ATC-302, Lincoln Laboratory, Massachusetts Institute of Technology, Lexington, MA, USA, Feb. 2002 (https://www.ll.mit.edu/mission/aviation/publications/publication-files/atc-reports/Gertz_2002_ATC-302_WW-15318.pdf).

[29]   COMSOFT Solutions GmbH, *ARTAS - ATM Surveillance Tracker & Server*, Product Brochure, 20-005-b-XVI, COMSOFT Solutions GmbH, Karlsruhe, Germany, (http://www.comsoft.aero/fileadmin/user_upload/pdf/brochures/artas.pdf).

[30]   R. Heidger and A. Mathias, "Multiradar tracking in PHOENIX and its extension to fusion with ADS-B and multilateration," in *Proc. of EuRAD'08 - 5th IEEE European Radar Conference*, Amsterdam, Netherlands, Oct. 2008 (http://ieeexplore.ieee.org/xpls/abs_all.jsp?arnumber=4760833).

[31]   EUROCAE, *078/ ED-117 - MOPS for Mode S Multilateration Systems for Use in A-SMGCS*, EUROCAE Working Group 41, Technical Specification EUROCAE ED-117, EUROCAE, Malakoff, France, Nov. 2003

(https://www.eurocae.net/eshop/catalog/product_info.php?products_id=207).

[32]   EUROCAE, *105/ ED-142 - Technical Specification for Wide Area Multilateration (WAM) Systems*, EUROCAE Working Group 70, Technical Specification EUROCAE ED-142, EUROCAE, Malakoff,   France,   Sep.   2010 (https://www.eurocae.net/eshop/catalog/product_info.php?products_id=323).

[33]   J. Chaoshu, L. Changzhong, and W. Xuegang, "GPS synchronised wide area multilateration system," in *Proc. of ICCCAS'09 - 2009 IEEE International Conference on Communications, Circuits   and   Systems*,   Milpitas,   CA,   USA,   Jul.   2009 (http://ieeexplore.ieee.org/stamp/stamp.jsp?tp=&arnumber=5250465).

[34]   D.W. Thomas, "Method for use in a multilateration system and a multilateration system," U.S. Patent 7 557 754, Jul. 7, 2009 (http://www.google.com/patents/US7557754).

[35]   Z. Xu, D. He, Y. Tang, and J. Li, "A MLAT Algorithm Based on Target Pressure Altitude," in *Proc. of ICMA'15 - 2015 IEEE International Conference on Mechatronics and Automation*, Beijing, China, Aug. 2015 (http://ieeexplore.ieee.org/stamp/stamp.jsp?tp=&arnumber=7237759).

[36]   R.F.R. Mojica, I.A.M. Gaviria, E.J.G. Pérez, J.V.B. Tejedor, and E.D.L.R. Davó, "A genetic algorithm and local search for the automated calculation of dilution of precision of mode-S multilateration systems at airports," in *Proc. of TIWDC/ESAV'11 - 22nd IEEE Tyrrhenian International Workshop on Digital Communications - Enhanced Surveillance of Aircraft and Vehicles*,   Capri,   Italy,   Sep.   2011 (http://ieeexplore.ieee.org/stamp/stamp.jsp?tp=&arnumber=6060999).

[37]   L. Alia, A. Italiano, and F. Pozzi, "Advanced tools to analyse the expected performance of multilateration and wide area multilateration," in *Proc. of TIWDC/ESAV'14 - 25th IEEE Tyrrhenian International Workshop on Digital Communications - Enhanced Surveillance of Aircraft and Vehicles*,   Rome,   Italy,   Sep.   2014 (http://ieeexplore.ieee.org/stamp/stamp.jsp?tp=&arnumber=6945453).

[38]   Y.P. Lei, F.X. Gong, and Y.Q. Ma, "Optimal distribution for four-station TDOA location system," in *Proc. of BMEI'10 - 3rd IEEE International Conference on Biomedical Engineering and Informatics*,   Yantai,   China,   Oct.   2010 (http://ieeexplore.ieee.org/stamp/stamp.jsp?arnumber=5639637).

[39]   Bin Yang and Jan Scheuing, "Cramer-Rao Bound and Optimum Sensor Array For Source Localisation From Time Differences of Arrival," in *Proc. of ICASSP'05 - 2005 IEEE International Conference on Acoustics, Speech and Signal Processing*, Philadelphia, PA, USA, Mar. 2005 (http://ieeexplore.ieee.org/stamp/stamp.jsp?arnumber=1416170).

[40]   K.W.K. Lui and H.C. So, "A study of two-dimensional sensor placement using time-difference-of-arrival measurements," *Digital Signal Processing*, Vol. 19, No. 4, Jul. 2009, pp. 650–659 (http://dx.doi.org/10.1016/j.dsp.2009.01.002).

[41]   Y. Meng, J. Xu, Y. Huang, and J. He, "Key Factors of Multi-station TDOA Passive Location Study," in *Proc. of IHMSC'15 - 7th IEEE International Conference on Intelligent Human-Machine Systems   and   Cybernetics*,   Hangzhou,   China,   Aug.   2015 (http://ieeexplore.ieee.org/lpdocs/epic03/wrapper.htm?arnumber=7334955).

[42]   Q. Jiang, *Network Radar Countermeasure Systems*, 1st Edition, Springer Berlin Heidelberg, Berlin, Germany, 2016.

[43]   ITU-R, *Propagation curves for aeronautical mobile and radionavigation services using the VHF, UHF and SHF bands*, Recommendation ITU-R P.528-3, ITU-R, Geneva, Switzerland, Feb. 2012 (http://www.itu.int/rec/R-REC-P.528/en).

[44]   G.D. Gierhart and M.E. Johnson, *The IF-77 Electromagnetic Wave Propagation Model*, NTIA Sponsor Report DOT/FAA/ES-83/3, U.S. Department of Commerce, National Telecommunications & Information Administration, Institute for Telecommunication Sciences, Boulder, CO, USA, Sep. 1983 (http://www.its.bldrdoc.gov/publications/2524.aspx).

[45]   EUROCONTROL,   Distance   Measuring   Equipment   Tracer   (DEMETER), http://www.eurocontrol.int/demeter, Oct. 2016.

[46] R. Sun and D.W. Matolak, "Initial results for airframe shadowing in L- and C-band air-ground channels," in *Proc. of ICNS'15 - 15th IEEE Integrated Communications, Navigation and Surveillance Conference*, Herdon, VA, USA, Apr. 2015 (http://ieeexplore.ieee.org/lpdocs/epic03/wrapper.htm?arnumber=7121271).

[47] J. Pinto, *Assessment and Design of Multilateration Telecommunication Systems installed in NAV Portugal, EPE*, M.Sc. Thesis, Instituto Superior Tecnico, Technical University of Lisbon, Lisbon, Portugal, 2011.

[48] R. Santos, *Assessment of wind turbines generators influence in aeronautical radars*, M.Sc. Thesis, Instituto Superior Tecnico, Technical University of Lisbon, Lisbon, Portugal, 2013.

[49] J. Fernandes, *Assessment of Wind Turbines Generators Influence in Aeronautical Navigation Systems*, M.Sc. Thesis, Instituto Superior Tecnico, Technical University of Lisbon, Lisbon, Portugal, 2013.

[50] R. Santos, *Impact of FM Broadcast Signals on Aeronautical Radionavigation*, M.Sc. Thesis, Instituto Superior Tecnico, Technical University of Lisbon, Lisbon, Portugal, 2015.

[51] ICAO, *Comparison of Typical Air/Ground Aeronautical Communication System Propagation Losses in the L band and the C band*, Report on RPG/ACP/NSP WP-42, ICAO, Montréal, Quebec, Canada, Feb. 2005 (http://www.icao.int/safety/acp/Inactive working groups library/ACP-WG-C-10/WGC10-IP04-Comparative link budgets L and C band.doc).

[52] EUROCONTROL, *FCI Technology Investigations: L band Compatibility Criteria and Interference Scenarios Study*, EUROCONTROL, Brussels, Belgium, Aug. 2009 (https://www.eurocontrol.int/sites/default/files/article/content/documents/communications/25082 009-lcis-s1tos5-compatibility-scenarios-v10.pdf).

[53] ITU-R, *Calculation of Free-Space Attenuation*, Recommendation ITU-R P.525-2, ITU-R, Geneva, Switzerland, Aug. 1994 (https://www.itu.int/rec/R-REC-P.525/en).

[54] C. Salema, *Microwave radio*, 3rd Edition, IST Press, Lisbon, Portugal, 2011.

[55] M. Geyer, *Earth-Referenced Aircraft Navigation and Surveillance Analysis*, Project Memorandum, DOT-VNTSC-FAA-16-12, Prepared for FAA-WTRO, Cambridge, MA, USA, Jun. 2016 (http://ntl.bts.gov/lib/59000/59300/59358/DOT-VNTSC-FAA-16-12.pdf).

[56] B.R. Mahafza, *Radar Systems Analysis and Design Using MATLAB*, 3rd Edition, Chapman and Hall/CRC, London, UK, 2013.

[57] A.W. Doerry, *Earth Curvature and Atmospheric Refraction Effects on Radar Signal Propagation*, Report SAND2012-10690, Unlimited Release, Sandia National Laboratories, Albuquerque, NM, USA, Jan. 2013 (http://prod.sandia.gov/techlib/access-control.cgi/2012/1210690.pdf).

[58] NASA JPL, ASTER Global Digital Elevation Model, https://doi.org/10.5067/ASTER/ASTGTM.002, Sep. 2016.

[59] NASA LP DAAC, Global Data Explorer, http://gdex.cr.usgs.gov/gdex/, Sep. 2016.

[60] Y. Qi, *Wireless Geolocation in a Non-line-of-sight environment*, Ph.D. Thesis, Princeton University, Princeton, NJ, USA, 2003 (http://cs.gmu.edu/~iyoun/geo/pdf/qi_thesis.pdf).

[61] Y. Qi, H. Kobayashi, and H. Suda, "Analysis of wireless geolocation in a non-line-of-sight environment," *IEEE Transactions on Wireless Communications*, Vol. 5, No. 3, Mar. 2006, pp. 672–681 (http://ieeexplore.ieee.org/lpdocs/epic03/wrapper.htm?arnumber=1611097).

[62] S. Hara, D. Anzai, T. Yabu, K. Lee, T. Derham, and R. Zemek, "A Perturbation Analysis on the Performance of TOA and TDOA Localisation in Mixed LOS/NLOS Environments," *IEEE Transactions on Communications*, Vol. 61, No. 2, Feb. 2013, pp. 679–689 (http://ieeexplore.ieee.org/lpdocs/epic03/wrapper.htm?arnumber=6427618).

[63] M.J. Leeson, *Error Analysis for a Wide Area Multilateration System*, Report QinetiQ/C&IS/ADC/520896/7/19, QinetiQ, Farnborough, Hampshire, UK, Aug. 2006.

[64] R.N. McDonough and A.D. Whalen, *Detection of Signals in Noise*, 2nd Edition, Academic Press/Elsevier, Cambridge, MA, USA, 1995.

[65]   J. Neering, *Optimization and estimation techniques for passive acoustic localisation*, Ph.D. Thesis, École Nationale Supérieure des Mines de Paris, Paris, France, 2009 (https://pastel.archives-ouvertes.fr/tel-00426732).

[66]   X. Lv, K. Liu, and P. Hu, "Geometry Influence on GDOP in TOA and AOA Positioning Systems," in *Proc. of NSWCTC'10 - 2nd IEEE International Conference on Networks Security, Wireless Communications and Trusted Computing*, Wuhan, Hubei, China, Apr. 2010 (http://ieeexplore.ieee.org/lpdocs/epic03/wrapper.htm?arnumber=5480336).

[67]   MathWorks, Techniques to Improve Performance, http://www.mathworks.com/help/matlab/matlab_prog/techniques-for-improving-performance.html, MATLAB R2016a Documentation, Apr. 2016.

[68]   MathWorks, Strategies for Efficient Use of Memory, http://www.mathworks.com/help/matlab/matlab_prog/strategies-for-efficient-use-of-memory.html, MATLAB R2016a Documentation, Apr. 2016.

[69]   F. Xiong, *Digital Modulation Techniques*, 2nd Edition, Artech House, Norwood, MA, USA, 2006.

[70]   A. Abdulaziz, A.S. Yaro, A.A. Adam, M.T. Kabir, and H.B. Salau, "Optimum Receiver for Decoding Automatic Dependent Surveillance Broadcast (ADS-B) Signals," *American Journal of Signal Processing*, Vol. 5, No. 2, 2015, pp. 23–31.

[71]   J.L. Gertz, *Fundamentals of Mode S Parity Coding*, Project Report ATC-117, DOT/FAA/PM-83/6, Lincoln Laboratory, Massachusetts Institute of Technology, Lexington, MA, USA, Apr. 1984 (https://www.ll.mit.edu/mission/aviation/publications/publication-files/atc-reports/Gertz_1984_ATC-117_WW-15318.pdf).

[72]   V.A. Orlando and P.R. Drouilhet, *Mode S Beacon System: Functional Description*, Project Report ATC-42 Revision D, DOT/FAA/PM-86/19, Lincoln Laboratory, Massachusetts Institute of Technology, Lexington, MA, USA, Aug. 1986 (http://extweb.ll.mit.edu/mission/aviation/publications/publication-files/atc-reports/Orlando_1986_ATC-42d_WW-15318.pdf).

[73]   Y. Nijsure, G. Kaddoum, G. Gagnon, F. Gagnon, C. Yuen, and R. Mahapatra, "Adaptive Air-to-Ground Secure Communication System based on ADS-B and Wide Area Multilateration," *IEEE Transactions on Vehicular Technology*, Vol. 65, No. 5, Jun. 2015, pp. 3150–3165 (http://ieeexplore.ieee.org/lpdocs/epic03/wrapper.htm?arnumber=7113878).

[74]   W. Peng, Y. Li, H. Li, and B. Wen, "A Novel High-sensitivity ADS-B Receiver Based on RF Direct Logarithmic Detecting," in *Proc. of ICCASM'12 - 2nd International Conference on Computer Application and System Modeling*, Paris, France, 2012 (http://www.atlantis-press.com/php/paper-details.php?id=2650).

[75]   dB Systems, dBs 5100A DME Antenna - Omni-Directional, http://www.dbsant.com/5100A.php, Part Number 500300-100, Apr. 2016.

[76]   T.M. Macnamara, *Introduction to Antenna Placement and Installation*, John Wiley & Sons, Chichester, UK, 2010.

[77]   W.D. Burnside and R.J. Marhefka, "Antennas on Aircraft, Ships, or Any Large, Complex Environment," in Y.T. Lo and S.W. Lee (eds.), *Antenna Handbook*, Springer US, Boston, MA, USA, 1988.

[78]   A.A. Moreira, *Antennas*, Lecture Notes, Instituto Superior Tecnico, Technical University of Lisbon, Lisbon, Portugal, Oct. 2015.

[79]   CST - Computer Simulation Technology, *Efficient Simulation of Electrically Large Structures: Antenna Placement and RCS*, CST Workshop Series 2010, Framingham, MA, USA, Feb. 2010 (https://www.cst.com/content/events/workshop_documents/2010/Electrically_Large_Structure_Simulation.pdf).

[80]   G.J. Schlieckert, *An Analysis of Aircraft L-Band Beacon Antenna Patterns*, Project Report ATC-37, FAA-RD-74-144, Lincoln Laboratory, Massachusetts Institute of Technology, Lexington, MA, USA, Jan. 1975 (https://www.ll.mit.edu/mission/aviation/publications/publication-files/atc-reports/Schlieckert_19

75_ATC-37_WW-15318.pdf).

[81]   S.M. Ross, *Introduction to probability and statistics for engineers and scientists*, 4th Edition, Academic Press/Elsevier, Boston, MA, USA, 2009.

[82]   M.C. Morais, *Probability and Statistics*, Lecture Notes, Instituto Superior Tecnico, Technical University of Lisbon, Lisbon, Portugal, Sep. 2010.

[83]   J. Bioucas-Dias, *Communication Theory*, Lecture Notes, Instituto Superior Tecnico, Technical University of Lisbon, Lisbon, Portugal, Oct. 2014.

[84]   J.S. Marques, *Digital Signal Processing*, Lecture Notes, Instituto Superior Tecnico, Technical University of Lisbon, Lisbon, Portugal, Mar. 2015.

[85]   MathWorks, Evaluating Goodness of Fit, https://www.mathworks.com/help/curvefit/evaluating-goodness-of-fit.html, MATLAB R2016a Documentation, Apr. 2016.

[86]   A. Castro, *Optimisation of Ground Stations Location in Aeronautical Multilateration Systems*, M.Sc. Thesis, Instituto Superior Tecnico, Technical University of Lisbon, Lisbon, Portugal, 2016.

[87]   RTCA, *Technical Link Assessment Report, Appendix 7: 1090 MHz Extended Squitter System Description*, RTCA Free Flight Select Committee, Safe Flight 21 Steering Committee, ADS-B Technical Link Assessment Team, RTCA, Washington DC, USA, Mar. 2001 (http://www.icao.int/safety/acp/ACPWGF/ACP-WG-M-3/WPM303.pdf).

[88]   H. Lee, "Accuracy Limitations of Hyperbolic Multilateration Systems," *IEEE Transactions on Aerospace and Electronic Systems*, Vol. AES-11, No. 1, 1975, pp. 16–29 (http://ieeexplore.ieee.org/lpdocs/epic03/wrapper.htm?arnumber=4101352).

[89]   K. Keunecke and G. Scholl, "Deriving 2D TOA/TDOA IEEE 802.11 g/n/ac location accuracy from an experimentally verified fading channel model," in *Proc. of IPIN'13 - 4th IEEE International Conference on Indoor Positioning and Indoor Navigation*, Montbéliard, France, Oct. 2013 (http://ieeexplore.ieee.org/lpdocs/epic03/wrapper.htm?arnumber=6817849).

[90]   Roke Manor Research, *Vigilance(TM) – Wide Area Multilateration Datasheet*, Roke Manor Research, Romsey, Hampshire, UK, 2006 (http://www.roke.co.uk/resources/datasheets/018-Vigilance.pdf).

[91]   Indra Sistemas, *Wide Area Multilateration*, Indra Sistemas, Madrid, Spain, Jan. 2013 (http://www.indracompany.com/sites/default/files/indra-indra_wide_area_multilateration_system_0.pdf).

[92]   Saab Sensis Corporation, MULTILATERATION SYSTEM - HIGH PERFORMANCE POSITIONING ON THE GROUND AND IN THE AIR, http://saab.com/security/air-traffic-management/air-traffic-management/Wide-Area-Multilateration/, Nov. 2015.